Interfacial and Near Interfacial Crack Growth Phenomena in Metal Bonded Alumina

by

Jamie Joseph Kruzic

B.S. (University of Illinois, Urbana-Champaign) 1996
M.S. (University of California, Berkeley) 1998

A dissertation submitted in partial satisfaction of the

requirements for the degree of

Doctor of Philosophy
in

Engineering – Materials Science and Mineral Engineering

in the

GRADUATE DIVISION

of the

UNIVERSITY OF CALIFORNIA, BERKELEY

Committee in charge:

Professor Robert O. Ritchie, Chair
Professor John W. Morris, Jr.
Professor Lisa A. Pruitt

Fall 2001

The dissertation of Jamie Joseph Kruzic is approved:

Chair	Date
	Date
	Date

University of California, Berkeley

Fall 2001

ABSTRACT

Interfacial and Near Interfacial Crack Growth Phenomena in Metal Bonded Alumina

by

Jamie Joseph Kruzic

Doctor of Philosophy
Engineering - Materials Science and Mineral Engineering

University of California, Berkeley

Professor Robert O. Ritchie, Chair

This study examines the mechanisms of interfacial and near interfacial crack propagation associated with the failure of sandwich specimens consisting of 99.5% pure polycrystalline alumina: 1) liquid state bonded with 99.999% pure aluminum layers and 2) partial transient liquid phase (PTLP) bonded using copper/niobium/copper interlayers. For the former system, the aluminum layer thickness was varied from 5 to 100 μm; it was found that the 3-point unnotched bending strength of the aluminum bonded joints increased, and the fracture toughness decreased, with decreasing layer thickness. Strength beams failed by ductile failure in the aluminum while fracture toughness samples failed by brittle fracture in the alumina. Under cyclic loading, crack growth occurred primarily by separating the aluminum from the alumina with evidence of ductile fatigue striations; cracks deviated into the alumina only for thin layered samples at high driving forces. Cyclic fatigue thresholds increased with decreasing layer thickness; however, the change to a brittle fatigue mechanism for thin layered samples at high driving forces was detrimental to the overall fatigue resistance. Under static loading in

moist air, interfacial separation was never observed at measurable rates ($\geq 10^{-9}$ m/sec); however, for 5 and 35 μm thick layered samples, cracks deviated off the interface and grew, sometimes stably, into the alumina resulting in time dependent failure.

For alumina PTLP bonded with copper/niobium/copper interlayers, the mean interfacial fracture toughness was found to decrease from 39 J/m^2 to 21 J/m^2 as temperature was increased from 25 to 1000°C. At room temperature, cyclic fatigue crack propagation occurred at both the niobium/alumina interface and in the alumina, with higher fatigue thresholds resulting from a predominantly near interfacial (alumina) crack path. During both fracture and fatigue failure, residual copper at the interface deformed and remained adhered to both sides of the fracture surface, while separation of the niobium/alumina interface appeared essentially brittle in both cases. The observed behaviors of all samples are examined in terms of modulus mismatch effects, the level of plastic constraint, the relative crack propagation resistance of each observed crack path, the loading conditions, extrinsic toughening from ductile phase and/or alumina grain bridging, and environmental influences.

TABLE OF CONTENTS

ACKNOWLEDGMENTS*

I'd like to first off thank my advisor, Rob Ritchie, for all his help, knowledge, and support during the pursuit of my Ph.D. here at Berkeley. Of course I would like to thank my parents, Joe and Marlene, my sister, Kim, and the rest of my family who raised me and have helped me continuously throughout the years. A very special thanks goes to Monica Barney, who has done by far the most to make my life during graduate school wonderful and help make this possible for me. The rest of my friends and support crew that have helped along the way have included Kinzy Jones, Brooks Larsen, Ed Cissel, Alex Greaney, Brandin Becker, Todd Williams, Luke Restorick, Autumn Fjeld, Nicola Armstrong, Chris Sybert, and many others too numerous to name. As for the lab, I would like to thank the Ritchie Group members, past and present, including Chris Gilbert, Avinash Kant, Josh Campbell, Don Bloyer, Brad Boyce, T.J. Becker, Aindrea McKelvey, Alexander Ziegler, Valeska Schroeder, Chris Muhlstein, Da Chen, Moon-He Hong, Heeman Choe, Gun Lee, Rong Yaun, Ravi Nalla, and of course the grand master of them all, Jim McNaney. Also, thanks to all the wonderful lab staff who have always been so helpful, such as Chip Flor, John Jacobson, James Wu, Peter Ruegg, Edwardo Saiz, Eric Stach, Ron Wilson, Doreen Ah Tye and many others. Additional thanks go to Robert Marks and Josh Sugar, and their advisor Professor Andy Glaeser, for fabrication of the partial transient liquid phase bonded joints used in this study. I would like to specially thank Rowland Cannon for his support and input involving my Ph.D. Thess work; additionally, I would like to thank Tony Thompson and Tony Tomsia for their help and input as well. Finally, thanks to everyone and anyone I can't remember to add to this list.

* This work was supported by the Director, Office of Science, Office of Basic Energy Sciences, Materials Sciences Division of the U.S. Department of Energy under Contract No. DE-AC03-76SF00098.

CHAPTER 1
INTRODUCTION

Metal/ceramic interfaces can be found in many engineering applications including microelectronic packaging, multi-layered films, coatings, joints, and composite materials. In order to design reliable engineering systems that contain metal/ceramic interfaces, a comprehensive understanding of interfacial and near interfacial failure mechanisms is necessary. Specifically, given an interfacial or near interfacial flaw, an understanding of how that flaw may to grow to failure, and how engineering systems can be designed to avoid such failures, is needed.

For monolithic materials, the majority of real service failures are time dependent, involving such mechanisms as mechanical fatigue, creep, and environmentally assisted slow crack growth. While much is understood about these failure mechanisms in monolithic materials, service failures persist and this is an ongoing area of investigation. Problems involving time dependent failure of multi-material systems are inherently more complicated and are much less understood than that of monolithic materials. Considerations must be made for differences in mechanical and thermal properties such as the elastic modulus, yield strength, and thermal expansion coefficient that can lead to different stress states, deformation properties, and residual stresses than would be expected for monolithic materials. Furthermore, for multi-material systems, additional crack paths are available for failure since cracks may grow in either of the bulk materials or at the interface, with each crack path typically having different failure mechanisms and crack propagation rates.

While much research has been conducted to understand the strength and fast fracture behavior of metal/ceramic interfaces [1-31], previous work is limited to a handful of studies looking at subcritical crack growth at interfaces, namely, fatigue crack growth under cyclic loading [32-36] and moisture assisted slow crack growth under static loading [19,37-39]. An understanding of subcritical crack growth is important, however, since these properties will most likely play an important role in dictating the lifetime and reliability of metal/ceramic interface containing systems; indeed, both fatigue crack growth under cyclic loading and moisture assisted slow crack growth under static loading allow for crack propagation to occur slowly, leading to time dependant failure. If a fabrication process results in a known interfacial flaw distribution, knowledge of the active growth mechanisms and the corresponding growth rates under both cyclic and static loading may allow for lifetime predictions to be made for various loading conditions. Furthermore, in addition to furthering the understanding strength and fast fracture properties, the goal of this research is to advance the understanding of subcritical cyclic fatigue crack growth and moisture assisted slow crack growth at and near ceramic/metal interfaces.

CHAPTER 2
BACKGROUND

2.1. Interface Fracture Mechanics

Linear elastic fracture mechanics allows a way to describe the conditions necessary to cause crack extension in terms of a characterizing parameter such as the strain energy release rate, G, or the stress intensity, K. These parameters are related such that

$$G = \frac{K_I^2}{E'} + \frac{K_{II}^2}{E'} + \frac{K_{III}^2}{2\mu}\ , \tag{2-1}$$

where $K_{I\text{-}III}$ are the mode I-III stress intensities, respectively, μ is the shear modulus, and

$$E' = E \qquad \text{plane stress,}$$
$$E' = \frac{E}{1-\nu^2} \quad \text{plane strain.} \tag{2-2}$$

E and ν are Young's modulus and Poisson's ratio, respectively. For single mode loading of monolithic materials, a single parameter can be used to describe the conditions necessary for crack advance, e.g., K_{IC} is sufficient to describe fracture under plane strain mode I loading conditions; however, for mixed mode loading, multiple independent parameters must be used, for example, K_I and K_{II} for mixed mode I and II.

When applying fracture mechanics to problems involving cracks at and near bimaterial interfaces, several complications arise, as noted by Williams [40] and others who first considered problems involving the stresses around an interface crack [41-44]. These complications can be understood by looking at the stress intensity for a crack on an interface subjected to mode I and/or mode II loading, which can be expressed by the

complex stress intensity factor first introduced by Rice and Sih [43,44] and further developed by Rice [22]:

$$K_1 + iK_2 = g(\alpha, \beta)(K_I^{\infty} + iK_{II}^{\infty})L^{-i\varepsilon} e^{i\omega(\alpha,\beta,L)}. \quad (2\text{-}3)$$

K_I^{∞} and K_{II}^{∞} are the far field applied mode I and II stress intensities for a monolithic sample while the elastic mismatch across a bimaterial interface in an elastic body is described by α and β, the non-dimensional Dunders' parameters, given by:

$$\alpha = \frac{E_1' - E_2'}{E_1' + E_2'}, \quad (2\text{-}4)$$

$$\beta = \frac{1}{2}\left[\frac{\mu_1(1-2\nu_2) - \mu_2(1-2\nu_1)}{\mu_1(1-2\nu_2) + \mu_2(1-2\nu_1)}\right], \quad (2\text{-}5)$$

where the subscripts 1 and 2 denote the materials above and below the interface, respectively [45]. L is a length parameter typically taken as the shortest in-plane length parameter for the given geometry, while ε is a function of elastic mismatch given by:

$$\varepsilon = \frac{1}{2\pi}\ln\left(\frac{1-\beta}{1+\beta}\right). \quad (2\text{-}6)$$

The functions $g(\alpha,\beta)$ and $\omega(\alpha,\beta,L)$ are geometry specific, with $\omega(\alpha,\beta,L)$ thought of as a phase shift that rotates the stress field a distance L from the crack tip, relative to that expected from far field loading. Fig. 2.1 schematically depicts the situation.

The shear (σ_{xy}) and normal (σ_{yy}) stresses ahead of an interface crack tip can be calculated from the complex stress intensity factor such that:

$$\sigma_{yy} + i\sigma_{xy} = (K_1 + iK_2)(2\pi r)^{-\frac{1}{2}} r^{i\varepsilon}. \quad (2\text{-}7)$$

From Eq. 2-7 it can be seen that the ratio of tensile to shear loading, given by the phase angle:

$$\psi = \tan^{-1}\left(\frac{\sigma_{xy}}{\sigma_{yy}}\right), \tag{2-8}$$

is dependent on *r*, the distance ahead of the crack tip. Since the phase angle changes with position ahead of the crack tip, to simplify interpretations of data, phase angles are typically calculated and reported using some reference length, *l*, ahead of the crack tip for a given problem. It is a simple matter to transform from one choice of *l* to another using the relation:

$$\psi_2 = \psi_1 + \varepsilon \ln\left(\frac{l_2}{l_1}\right) \tag{2-9}$$

and thus given the choice of reference length, data can be transformed to determine the state at any relevant length ahead of the crack tip [22].

While an early concern about the admissibility of interface stress intensity solutions was that they predicted interpenetration of the crack faces near the crack tip [42], the solutions have been shown to be admissible and valid away from the near tip contact regions assuming that such contact regions are small compared to other relevant size scales [22]. A more serious concern regarding the validity of interface stress intensity solutions has come about recently regarding the size of the region of *K*-dominance, i.e., the size of the region over which the asymptotic stress intensity solutions accurately give the stresses ahead of a crack [46]. Practical interface samples often introduce new size scales to problems, such as a layer thickness for sandwich specimens, which results in *K*-dominant regions much smaller as compared to monolithic samples [46]. Often this results in the region of *K*-dominance being embedded within the plastic zone of the lower strength material, bringing into serious question the validity of any fracture criteria based on the stress intensity in these cases [46].

In addition to concerns of validity, there are some practical concerns regarding the presentation and interpretation of interface fracture results in terms or the complex stress intensity factor. It can be seen from Eq. 2-3 that even under nominally applied mode I loading ($K_{II}^{\infty} = 0$) there will still be a complex contribution ($K_2 \neq 0$) to the stress intensity and thus a single parameter is not sufficient to describe the crack tip state. Thus, even for the simplest interface fracture problems, a multi-parameter criteria for crack advance must be used unless simplifying assumptions about the crack tip state are made. Additionally, the phase angle, ψ, depends on both the length parameter, L, and the chosen reference length, l. While different choices of l can be accommodated using Eq. 2-9, it is unclear which choices of l make the most physical sense. Additionally, to explain the difficulties presented by dependence of ψ on L, Rice [22] used the simple example where L is equal to the crack length, a, as in a semi-infinite bimaterial. For this case it is implied that to achieve the same crack tip state of a tensile loaded sample ($K_{II}^{\infty} = 0$) with crack length a_1, a sample with crack length a_2 must be loaded under combined tensile and shear loading ($K_{II}^{\infty} \neq 0$) [22], a serious concern especially when characterizing growing cracks. Finally, it should be noted that different complex stress intensity solutions are required for cracks that deviate off the interface [47], complicating analysis for cracks that may not lie entirely at the interface.

Such concerns make the strain energy release rate, G, an attractive characterizing parameter for fracture of many practical sample geometries. Provided small scale yielding conditions are satisfied, G provides a measure of the energy available for fracture and is invariant with respect to crack position (i.e, fracture at or near the interface). One must use caution, however, since the critical strain energy release rate to

cause failure, G_c, can be strongly affected by the magnitude of ψ. If one can reasonably assume similar crack tip states (e.g., mode I) for all cases of interest; however, G can be used as a single parameter crack advance criteria for interface problems, greatly simplifying the presentation and interpretation of interface fracture data. In general, the strain energy release rate can be related to the complex stress intensity factor by [12]:

$$G = \frac{1}{2}(1-\beta^2)\left(\frac{1}{E_1'}+\frac{1}{E_2'}\right)(K_1^2 + K_2^2); \qquad (2\text{-}10)$$

however, for specific geometries such as mode I loaded sandwich specimens, where a thin layer is sandwiched between two like members, more simple calculation methods can be employed.

It is noted that for sandwich specimens, where the layer thickness, h, is small compared to all other relevant sample dimensions, the magnitude of the strain energy release rate is essentially unaffected by the presence of the layer [25]. G can thus be simply calculated from standard stress intensity solutions for monolithic samples using the expression given in Eq. 2-1. Additionally, for thin layer sandwich samples with predominantly mode I far-field loading (e.g., as with compact tension, C(T), specimens), it has been shown that that the actual phase angle is typically small, implying that such geometries are essentially mode I specimens [25]. Since G_c is only weakly sensitive to ψ when it is small [12], this implies that the strain energy release rate can be used to satisfactorily describe the linear elastic driving force for crack advance for such mode I configurations. Note that as a single characterizing parameter for interface fracture using mode I sandwich specimens, G offers the advantages of being a single parameter that is easy to compute and invariant with respect to crack position (i.e., at versus near the interface).

2.2. Crack Path Considerations

Another complication when dealing with problems involving interfacial fracture is that there are several possible crack paths, and crack trajectories may change depending on the loading conditions, environment, and other factors. For homogeneous, brittle materials it has been proposed that cracks follow a path with a local mode I stress field (i.e., $K_{II} = 0$) [48], a path of maximum hoop stress [49], or a path of maximum strain energy release rate [50]. For straight or slightly curved continuous cracks these criteria have been shown to be identical in their crack path predictions; however, in the case of discontinuous, finite crack kinking, the kink angles predicted by the various criteria deviate slightly [51,52].

For an interface crack in an semi-infinite bimaterial, it has been found that crack kinking into the more compliant material is favored since more strain energy can be released, and thus the highest driving force direction is dominated by the sign of α [53]. Crack path predictions cannot rely solely on the aforementioned criteria, however, since the relative toughness of the two materials and the interface also determines whether the crack will stay at the interface or kink away from it. If the more compliant material is significantly tougher than both the interface and the stiffer material, the crack may be trapped at the interface or kink into the stiffer material. For kinking into the more compliant material, it has been found that the $K_{II} = 0$ and the maximum strain energy release criteria predict virtually identical kinking directions for linear elastic materials. When the crack kinks into the stiffer material; however, large deviations are observed,

with the maximum strain energy release rate occurring at small angles while $K_{II} = 0$ predicts kink angles close to 45°.

For sandwich specimens, issues of crack kinking are more complex with the parameter β playing a prominent role in determining crack path. Fig. 2.2 shows the crack paths predicted based on the highest driving force direction using a $K_{II} = 0$ criteria for various metal/ceramic material combinations based on their elastic mismatch parameters α and β [54]. Defining the outer members as material 1 and the layer as material 2, for $\beta < 0$ the crack is expected to kink towards material 1 and away from the layer, independent of the value of α (i.e., independent of the relative stiffness). For positive β, in all cases the crack is expected to kink towards/into the layer; however, the preferred path within the layer is dependent on the value of α, with both centerline and off-center crack paths possible. Once again, it is important to point out that these predictions only consider which direction has the highest driving force for fracture and do not take into account the relative toughnesses of material 1, material 2, and the interface, which will also have an important role in determining the actual crack path.

2.3. Metal/Ceramic Interface Studies

In general, investigations into the strength and fracture of metal/ceramic interfaces have yielded a wide variance in results depending on the material system and test conditions [8]. In the case of "weak" interfaces (due to poor bonding, impurities, brittle interfacial phases), failure typically occurs at the interface at low applied loads. Well bonded "strong" interfaces have shown a much wider variety of behavior, with failure occurring in the metal, ceramic, or at the interface, with changes in mechanism observed

for some systems depending on test conditions. In strength tests, both single crystal alumina (sapphire) and polycrystalline alumina strongly bonded to aluminum have exhibited a ductile failure mode with voids nucleating at the interface, then growing and coalescing to failure in the ductile metal [2,28]. Fracture toughness tests using interfacial pre-cracks on polycrystalline alumina/aluminum interfaces have shown both a ductile hole growth failure mechanism, as well as brittle failure with the crack propagating in the alumina [17,33]. Sapphire and polycrystalline alumina strongly bonded to gold, platinum, niobium, or nickel, however, have typically exhibited interfacial separation with no microvoid coalescence when tested in an ambient air environment [4,9,10,19,20].

When tested in an inert dry nitrogen environment, however, the failure mechanism of sapphire/gold interfaces was observed to switch from relatively brittle debonding to ductile microvoid growth and coalescence [19,20]. The brittle debonding observed in ambient, humid air has been attributed to moisture assisted cracking and is associated with toughness values ~ 50 J/m^2 under mixed mode conditions ($\varphi \approx 52°$). In the absence of moisture, however, voids nucleated at the interface ahead of the crack and left intact ligaments behind the crack tip, giving rising crack growth resistance curves (R-curves) and higher mixed mode toughness values, up to ~ 150 J/m^2 at the peak of the R-curve [20].

For sapphire/nickel interfaces, a similar effect of moisture has been observed. Interface cracks that debonded in room air at mixed mode fracture energies as low as 10 J/m^2 were found to blunt significantly in a dry nitrogen environment; such cracks would not grow at driving forces up to 100 J/m^2 [9]. Furthermore, a study investigating the mode I fracture of sapphire/nickel interfaces in a dry environment revealed that

considerable crack blunting (CTOD ~ 140 nm) could be measured prior to the final failure at ~ 70 J/m^2 [24]. In contrast to sapphire/gold interfaces, in a dry environment under conditions causing considerable crack tip blunting these sapphire/nickel interfaces failed by interface separation instead of by microvoid coalescence.

Due to the low thermal expansion mismatch, the alumina/niobium system has been studied extensively using polycrystalline samples as well as bicrystals. Fracture energies of 9 – 90 J/m^2 have been reported for polycrystalline samples under mode I loading [4,14,18,55,56], while bicrystals have exhibited a range of 74 - >2100 J/m^2 depending on the relative orientations of the niobium and sapphire single crystals [4,13,57]. Investigations into the effects of mixed mode loading have shown an increase in fracture energy with increasing phase angle, ψ [18]. For bicrystal samples, the crystal orientations were found have a large effect on fracture energy, with results spanning ~ 1.5 orders of magnitude [4,14]. The orientation of the niobium crystal relative to the crack front determines the active slip systems, and thus the amount of plastic dissipation, leading to changes in fracture energy. Additionally, the relative orientation of the sapphire to the niobium was also found affect the fracture energy, with these differences attributed to small changes the work of adhesion, W_{ad}. As for sapphire/nickel interfaces, cracks propagated by interfacial separation even for the toughest bicrystal samples, where considerable blunting and measurable slip steps were observed on the fracture surface [14,58].

Changes in the interfacial chemistry by doping with impurities was also found to strongly affect the fracture energies of sapphire/niobium bicrystals. With sub-monolayer additions of silver or sulfur, sapphire/niobium interfacial fracture energies were found to

decrease significantly [13,14,57]; conversely, similar doping with titanium was shown to increase the sapphire/niobium fracture energy [14,57]. The direction of these trends corresponds with the computed changes in the work of adhesion [57] and/or the work of attraction, W_{at}, [14] caused by the addition of the dopant. While the work of adhesion implies all segregation at the interface and on the new surfaces is in equilibrium with the environment, the work of attraction is defined as applying to the limiting case where segregants at the interface are simply partitioned between the surfaces formed during separation, and it represents a reversible, metastable work that can be computed thermodynamically [14]. An extremely strong dependence of sapphire/niobium interfacial fracture energy on W_{at} has been demonstrated, with fracture energies spanning two orders of magnitude while W_{at} increases from 0.8 to 2 J/m^2 [14]. Effects of impurities on fracture energy has also been reported for sapphire/nickel [24,30] and sapphire/gold [29] interfaces.

2.4. Constraint and Interface Failure

2.4.1. Role of constraint in the strength and fracture of ductile materials

The strengthening effects resulting from constraining a plastically deforming ductile material with an elastic material have long been utilized in areas such as soldering and brazing. Indeed, a study by Ashby *et al.* [59] has shown that pure lead wires can reach yield strengths six times that of bulk material when constrained by well bonded glass tubes, finally failing by the formation and growth of a single cavity instead drawing to a point. In applying fracture mechanics to ductile materials, plastic constraint has always

been a concern since the plastic zone near the crack tip is typically constrained by the surrounding elastic material, generating a local triaxial stress state.

When the plastic zone ahead of a crack tip is well constrained through the thickness of the sample, the z-direction in Fig. 2.3, a condition of plane strain is said to exist. In the middle section of the sample, the elastic material surrounding the plastic zone constrains the plastic strain through the thickness, and stresses develop in the z-direction, resulting in a triaxial stress state. Near the sides of the sample, however, plasticity is unconstrained since stress cannot develop normal to the free surface. This leads to a variation in the plastic zone size and shape through the thickness of the sample, illustrated schematically in Fig. 2.3, as well as variations in the stress state. For thin samples, the lack of constraint at the free surfaces does not allow for stresses to fully develop in the z-direction, and a condition of plane stress is said to exist. In fracture of ductile materials, samples in a condition of plane strain result in lower measured toughness values since the triaxial stress state promotes void formation and growth that leads to ductile fracture. Measurements of plane strain fracture toughness are typically most desirable since they provide a lower bound, geometry independent fracture toughness value. In addition to the sample sides, constraint can also be lost if plasticity extends to any free surface, including the top, bottom, or back of the sample, which also can result in an increase in the measured toughness value. When measuring plane strain fracture toughness, care must be taken to design the sample so that the plastic zone is small relative to all relevant sample dimensions, ensuring full constraint of the plastic zone.

In layered structures utilizing metals and ceramics, additional constraint may be imposed at the material interfaces. Fig. 2.4 illustrates schematically a crack in a ductile metal layer sandwiched between two ceramic members. As the plastic zone extends across the metal layer, it impinges on the ceramic, which does not plastically deform, and becomes constrained. In order to look at effects of this type of constraint on fracture, Varias *et al.* [27] modeled numerically the case depicted in Fig. 2.4 and showed that constraint of the plastic zone through the layer thickness has a profound effect on the stress state ahead of the crack tip, increasing the magnitude of the stresses as well as the degree of triaxiality. This effect was quantified by using the mean hydrostatic stress normalized by the yield strength, σ_m / σ_o, where σ_m is defined as one third of the sum of the normal stresses, $1/3(\sigma_{xx} + \sigma_{yy} + \sigma_{zz})$. When the extent of the plastic zone in the x-direction, r_{px}, was less than 3 times the metal layer thickness, h, the magnitude and distribution of σ_m / σ_o changed very little with increasing load, with the maximum value of σ_m / σ_o in the 2.8 – 3 range. When r_{px} exceeded $3h$, however, both the distribution and the maximum value of σ_m / σ_o changed significantly, with the peak value of σ_m / σ_o shifted farther ahead of the crack tip and reaching values > 6.

Experiments looking at the fracture of metal/sapphire sandwich specimens have verified that changing the amount of constraint via changing the layer thickness can have a significant effect on the measured toughness values [10,20,31]. For mode I fracture testing in the alumina/gold system, fracture energies for pre-notched samples decreased from 12 to 3 J/m^2 as layer thickness was reduced from 100 to 25 μm while for the alumina/platinum system fracture energies decreased from 28 to 6 J/m^2 as the layer thickness was reduced from 125 to 10 μm [10]. For mixed mode testing, initiation

fracture energies decreased by 30% after reducing the layer thickness from 100 to 10 μm in the alumina/gold system ($\varphi \approx 52°$) [20]. Similarly, a 36% decrease in the mixed mode initiation fracture energy was observed in the alumina/copper system for a reduction in layer thickness from 130 – 25 μm [31].

2.4.2. Constraint effects in the alumina/aluminum system

Studies of the strength of interface samples comprised of thin layers of aluminum bonded between alumina have shown a definite effect of constraint through the thickness of the layer. In bending, strength was found to have an inverse relationship to layer thickness over the range of 100 - 500 μm thick layers, following trends predicted from plasticity theory [2,3]. Investigations into the fracture and fatigue behavior of aluminum/alumina interface sandwich specimens with 100 - 500 μm thick metal layers, however, did not as clearly demonstrate constraint effects [33]. When fracture toughness values were computed using linear elastic solutions (i.e., using small scale yielding, SSY, assumptions), very little effect of layer thickness was observed; however, observations of highly blunted crack tips on fractured samples indicated that there was a need to account for large scale plasticity. Toughness estimates accounting for the large scale plasticity ahead of the crack tip gave an order of magnitude increase in toughness with increasing layer thickness from 100 to 500 μm; however, the accuracy of the estimates was limited, and thus they only demonstrated the expected qualitative trend. For the fatigue crack growth threshold, where driving forces are low enough for SSY assumptions to be valid, it was found that layer thickness had no observable effect for the 100 - 500 μm layer thickness range [33]. Additionally, no effects were observed on fatigue crack growth

rates at higher driving forces; however, there are concerns regarding the validity of the SSY assumptions made in calculating those higher driving forces due to excessive plasticity [33].

Although no effect on cyclic fatigue crack growth thresholds and rates have been observed previously, as the thickness of the metal layer is reduced further, thus constraining the plastic zone, one may expect an effect on fatigue crack growth rates. Since cyclic fatigue crack growth for ductile materials is dependent on plastic deformation mechanisms near the crack tip, as dislocation motion is restricted by the metal/ceramic interface, one might expect fatigue crack growth mechanisms to be restricted as well. For the 100 - 500 μm thick layers studied in [33], however, the computed plastic zone at the fatigue threshold was fully embedded in the metal layer, and thus there was no constraint on the plasticity through the layer thickness due to the ceramic. Indeed, the computed plastic zone thickness, r_{py}, is small enough near the fatigue threshold ($r_{py} \approx 35$ μm at 4 J/m^2 [23,36]) so that it is not expected to extend completely across the metal layer for 100 - 500 μm layers. This unconstrained configuration is illustrated in Fig. 2.5 which shows schematically the plastic zone for a bimaterial interface crack and defines r_{py}. Thus one goal of this research is to investigate fatigue crack growth along interfaces in alumina/aluminum sandwich specimens with metal layer thicknesses in the range of 5 - 100 μm where the plastic zone will be constrained through the thickness of the metal layer at the fatigue crack growth threshold for the thinner layers. Additionally, the use of thinner layers will allow for a more clear demonstration of constraint effects on the fracture toughness since plasticity is limited for thinner layers making SSY assumptions more reasonable.

While no evidence of moisture assisted slow crack growth under static loading has been found for the aluminum/alumina system, such behavior has been observed for sapphire/gold [19], sapphire/nickel [9], and glass/copper [37,38] interfaces in sandwich specimens. Additionally, it is known that both polycrystalline alumina and sapphire are susceptible to moisture assisted crack growth under static loading in a humid environment [60,61]. In the above cases, interactions of water molecules with the crack tip are thought to promote crack advance, resulting in time dependent failure under static loading similar to that found for stress corrosion cracking in metals. It is reasonable to expect, therefore, that given a sharp crack at an alumina/aluminum interface, there is a possibility that moisture assisted crack growth may occur either in the alumina or along the interface when subjected to a static load. Although this crack growth mechanism was not observed in the previously mentioned study [33], this may have been due to local reductions in the crack tip stresses due to crack tip blunting into the ductile aluminum layer. Indeed, measurements gave interfacial toughness values well in excess of bulk alumina and extensive crack tip blunting was observed. As the metal layer thickness is reduced well below 100 microns, however, the plasticity in the metal layer will be further limited by constraint due to the ceramic, therefore limiting the amount of blunting, leading to increased crack tip stresses. Accordingly, another goal of this research is to investigate moisture assisted crack growth in alumina/aluminum sandwich specimens with metal layer thicknesses in the range of 5 - 100 μm, where increased constraint may raise the crack tip stresses to levels high enough to activate this previously unobserved failure mechanism either at the interface or in the ceramic.

2.5. Novel Bonding Routes and Complex Interfacial Structures

While high purity interfacial systems such as alumina/aluminum provide an attractive medium with which to study interfacial failure mechanisms with a minimum of variables, some novel processing routes of interest result in more complex interfacial structures with several phases. There is specifically a desire to produce ceramic/metal/ceramic sandwich joints that retain reasonable strength at elevated temperatures without requiring the high temperatures and pressures typically necessary for conventional solid state diffusion bonding. One avenue to pursue that goal has been partial transient liquid-phase bonding (PTLPB) [62-72], where an additional liquid phase is used at the interfaces to facilitate the solid state joining of the ceramic/metal/ceramic joints. PTLPB offers the advantages of potentially lower processing temperatures and/or pressures than conventional diffusion bonding while resulting in joints that can retain appreciable strength at elevated temperatures.

One model system used to further the understanding of PTLP bonding methods employs a multilayer interlayer comprised of a relatively thick (125 μm) niobium core layer and thin (~ 3 μm) copper cladding layers to bond alumina [66,67,71]. During bonding, the liquid copper-rich phase de-wets the interface, yielding at least two distinct metallic phases in contact with the alumina, one niobium-rich and the other copper-rich. Although discrete copper-rich particles persist along the interface and melt at ~1083°C, the high area fraction of niobium/alumina contact allows joints to retain reasonably high strength levels up to 1300°C, well above the melting point of copper, with the majority of failures occurring away from the joint in the alumina [66,67]. While strength is an important property governing the suitability of joints for structural applications, fracture

and cyclic fatigue properties (i.e., flaw tolerance) must also be assessed to predict the reliability and lifetime of joints. No previous studies have investigated the fracture toughness and fatigue crack growth properties at or near PTLP bonded joints, and accordingly, the final goal of this research is to provide a first investigation into the fast fracture and cyclic fatigue crack growth properties of PTLP bonded alumina/niobium joints.

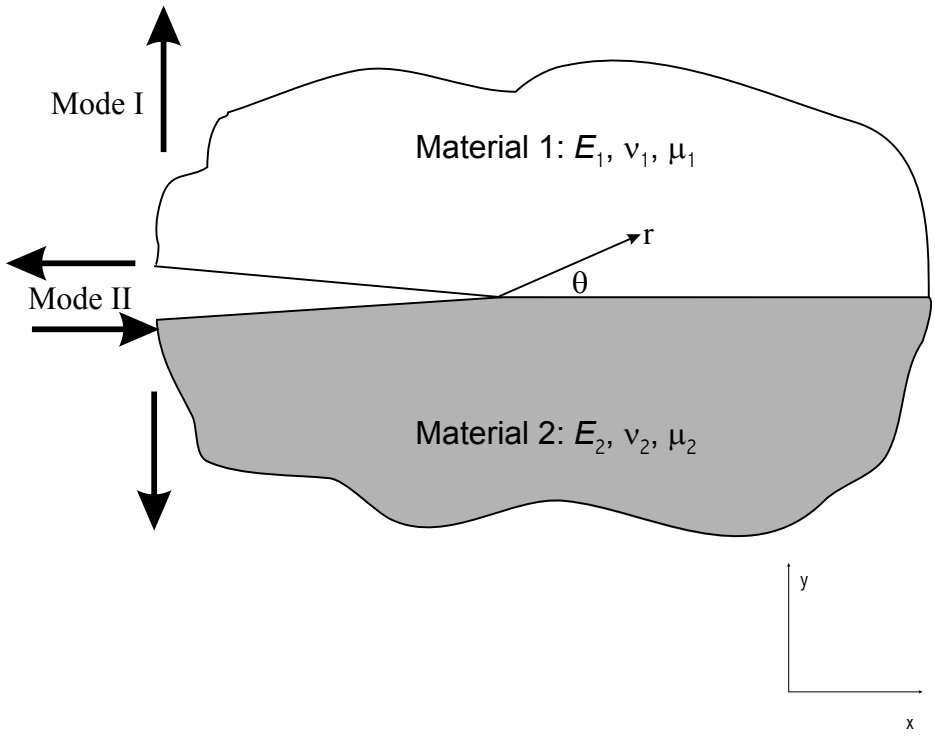

Figure 2.1. Schematic of a bimaterial interface crack under mode I and II loading.

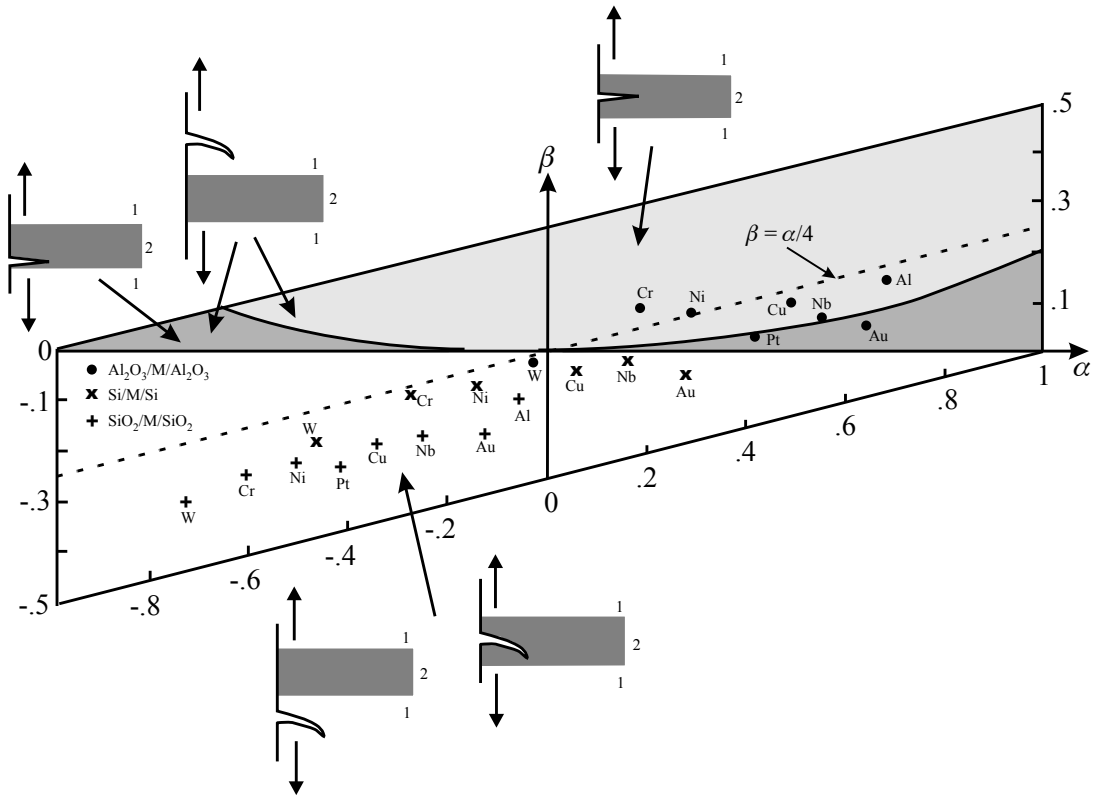

Figure 2.2. Plot of the elastic mismatch parameters α and β in plane strain, showing three predicted regimes of $K_{II} = 0$ crack path trajectories for ceramic/metal/ceramic sandwich geometries subjected to far-field mode I loading taken from Ritchie *et al.* [53]. For negative β values, the highest driving force direction is for the crack to deviate out of and/or away from the layer material 2. For positive β, crack growth deviating towards or orrurring within the layer is favored, with the prefered loaction in the layer (i.e., center or off center) determined by the value of α as shown.

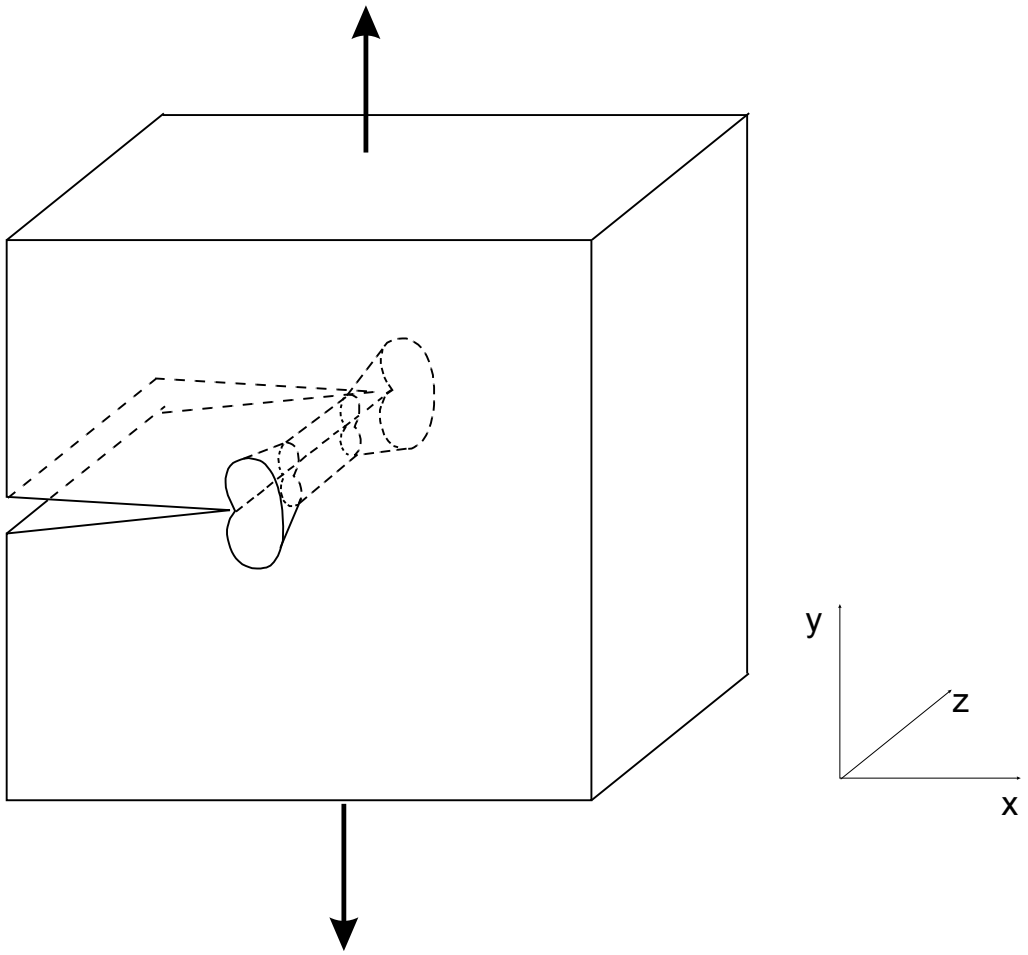

Figure 2.3. Schematic illustrating the plastic zone shape and size variation through the thickness of a fracture specimen due to changing constraint.

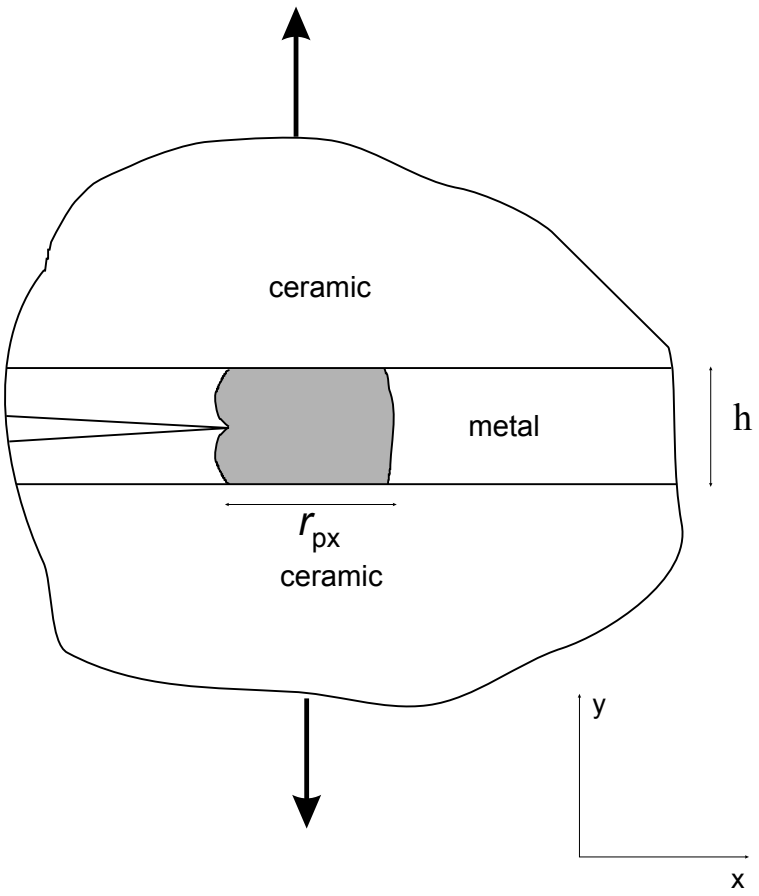

Figure 2.4. Schematic illustrating the constraint of the plastic zone ahead of a crack tip through the thickness of a metal layer bonded between two ceramic substrates.

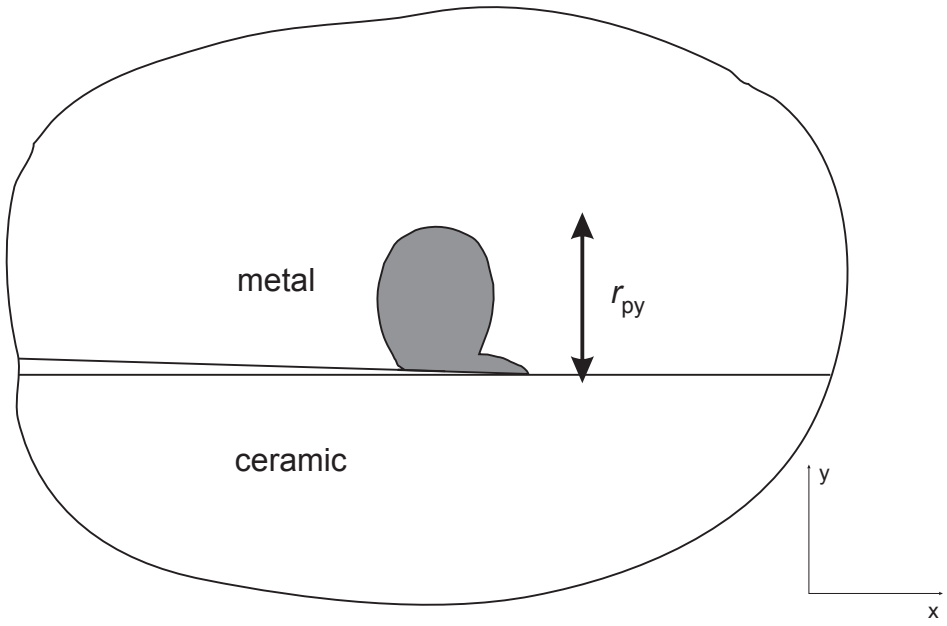

Figure 2.5. Schematic illustrating the extension of the plastic zone into the metal ahead of a bimaterial interface crack under small scale yielding conditions modeled after the results of Shih and Asaro [23].

CHAPTER 3
EXPERIMENTAL PROCEDURES

3.1. Materials and Sample Fabrication

3.1.1. Alumina/aluminum joints

Liquid state bonding was used to make sandwich specimens with 5, 35, and 100 μm thick layers of 99.999% pure aluminum bonded between 99.5% pure polycrystalline alumina (Coors AD995). The bonding surfaces of the Coors AD995 alumina blocks (21.3 mm square by 10.2 mm thick) were lapped to a 1 μm finish using successively finer diamond compounds before rinsing in acetone and ethanol and baking at 1000°C in air for one hour to remove any organic contaminants. The alumina microstructure is shown in Fig. 3.1, with a mean linear intercept of 11.7 μm, corresponding to a nominal grain size, d_g, of 18 μm using ASTM standard E112.

High purity (99.999%), 250 μm thick aluminum foil was rolled to thicknesses of 35 μm and 100 μm. Foils were cut to size, degreased in acetone and ethanol, and etched to remove the oxide scale resulting from the rolling operations. Etching was conducted by immersing the foils in Tucker's reagent (25% H_2O, 45% HCl, 15% HNO_3, 15% HF) and agitating for 1 – 2 minutes before rinsing in distilled water and ethanol. The foil was placed between two polished alumina pieces and cold pressed to ~ 40 MPa. After cold pressing, the assembly was placed in a closed, high purity (99.8%) alumina crucible between two high purity alumina flat disks for bonding, as seen in Fig. 3.2. Bonding was carried out in a purified, gettered argon environment with titanium chips added to the crucible to provide additional gettering near the sample. The crucible was heated to 980°C at a rate of 30°C/minute and held for 5 minutes before cooling at 20°C/minute.

For the fabrication of samples with 5 μm thick aluminum layers the use of foils proved impractical since rolling and handling of such thin foils is prohibitively difficult. Instead, thin coatings of 99.999% pure aluminum were evaporated on the surface of each block in the place of the foil, and the same bonding procedure was followed. Due to crowning of the polished alumina surface from the lapping procedure, adequate bonding was not achieved at the edges of the blocks for bonds with 5 μm thick aluminum layers and thus only the well bonded center portion was used for testing, resulting in slightly smaller samples and fewer samples per bond. Bonded blocks using AD995 alumina were machined into 3 mm thick compact tension, C(T), specimens for fracture and fatigue testing as shown in Fig. 3.3. Sample widths, *W*, were 17 mm for the 100 and 35 μm thick layer samples, and 14 mm for the 5 μm thick layer samples due to the removal of the unbonded edges; five and three C(T) samples were machined from the bonded blocks, respectively. Additionally, 3 mm thick C(T) samples (W = 17 mm) were machined to measure the fracture and fatigue properties of the bulk AD995 alumina.

Additional samples were made for determining interface strength as a function of layer thickness using 99.999% aluminum foils sandwiched between 99.8% pure alumina (Coors AD998), using the same bonding procedures outlined above. The microstructure of Coors AD998 alumina was much finer than that of AD995 (Fig. 3.1), with a mean liner intercept of 2.7 μm, corresponding to a nominal grain size of 4 μm using ASTM standard E112. Switching to a finer grained, higher strength alumina was necessary to measure joint strength since all bend beams made from AD995 alumina joined with aluminum failed in the ceramic, away from the bonded layer. Bonded rods of AD998 alumina were machined into nominally 3 mm square, 50 mm long bend beams for 3-point

bend testing. Some mechanical and physical properties for materials used can be seen in Table 3.1, while the mismatch parameters α and β for the alumina/aluminum system are given in Table 3.2.

Table 3.1. Mechanical† and physical properties

	AD995	AD998	Aluminum	Niobium	Copper
Elastic Modulus (E)	372 GPa	350 GPa	72 GPa	103 GPa	125 GPa
Shear Modulus (μ)	152 GPa	143 GPa	27 GPa	37.5 GPa	46.4
Poissons Ratio (ν)	0.22	0.22	0.333	0.37	0.34
Mean grain size (d_g)	18 μm	4 μm	-	-	-

†Elastic properties for the aluminas were given by Coors while elastic properties for pure metals were taken from [73].

Table 3.2. Dundurs' parameters for elastic mismatch*

Material 1/Material 2	α	β
Alumina/Aluminum	0.657	0.271
Alumina /Niobium	0.532	0.153
Alumina /Copper	0.469	0.152
Niobium/Copper	-0.084	-0.001

*Calculations are based on properties for AD995 alumina

3.1.2. PTLP bonded niobium/alumina joints

Partial transient liquid phase bonding was carried out using Coors AD995 alumina bonded with a relatively thick (125 μm) niobium layer utilizing thin (3 μm) copper interlayers layers to facilitate bonding. Specifically, one 19.5 mm by 22.5 mm surface of an ~8.6 cm^3 Coors AD995 alumina block was ground flat and polished on a lapping machine using progressively finer diamond compounds followed by colloidal silica as a final polishing agent. For each joint, two such blocks were ultrasonically cleaned in various solutions (detergent and water, distilled water, acetone, and isopropyl alcohol) followed by a 1 hr anneal in air at 1000°C. Copper wire was cleaned in isopropyl

alcohol, bright dipped (5:1 nitric acid:distilled water), rinsed, dried, and evaporated onto the alumina blocks under high vacuum, yielding an approximately 3 μm thick coating on the polished surfaces. While the coated alumina was kept under vacuum, a 125 μm (99.99% pure) niobium foil was also cleaned using various solutions (detergent and water, isopropyl alcohol, ethanol, and nanopure water). After drying, the cleaned niobium foil (also 19.5 mm by 22.5 mm) was sandwiched between the polished surfaces of two copper coated alumina blocks (Fig. 3.4). The assembly was then loaded into a graphite hot press and processed at 1390 - 1400°C for 6 hr. Heating was performed at 4°C/min while cooling was at 2°C/min. A 2.2 MPa load was maintained for the entire heating, soaking, and cooling cycles of the process. Five 3 mm thick, 17 mm wide compact tension, C(T), fracture and fatigue specimens were machined from each joint (Fig. 3.3). Further details of the materials and PTLP bonding process used to make joints for this study are presented elsewhere [66,67,71].

The bonding process described above resulted in a multi-phase interlayer microstructure with the majority of the bonded interfacial area consisting of alumina bonded directly to niobium, while roughly 11% of the interfacial area contained isolated regions of copper located between the niobium and alumina. Additionally, some residual interfacial porosity was present, on the order of a few percent, which appeared to be present in a greater area fraction near the edges of the bonded blocks. Some mechanical and physical properties for the materials used in this study are listed in Table 3.1, while the calculated values of α and β for this system are tabulated in Table 3.2. The most relevant of these mismatch parameters are expected to be for the mismatch between the

alumina and the niobium layer since these two materials make up the majority of the joint interface.

3.2. Strength Experiments

Interface strength experiments were conducted on nominally 3 mm square, 50 mm long samples using a 3-point bend geometry with a span (distance from the center to outer load point) of 12.7 mm. The unnotched bend samples were polished on the tensile loading face by lapping to a 1 μm finish using successively finer diamond compounds and all edges of the bend beams were beveled using a diamond grinding disk to prevent premature failure due to stress concentrations at the corners. The bending strength of each sample was computed from the peak failure load using conventional beam theory.

3.3. Fracture Toughness Experiments

3.3.1. Alumina/aluminum joints

Interfacial fracture toughness experiments were carried out on fatigue pre-cracked C(T) specimens in room air at 25°C (20 - 40% R.H.), where the fatigue pre-cracks initially were located at the interface. Pre-cracking was performed by cycling samples until stable cracks initiated on the alumina/aluminum interface ahead of machined notches (~ 0.2 mm wide, with length $a_o \approx 5$ mm), at which point cyclic loads were incrementally reduced until the interfacial fatigue crack growth rates were on the order of 10^{-10} m/cycle (i.e., fatigue threshold), thus minimizing the size of the cyclic plastic zone in the aluminum ahead of the crack tip. Samples were then subjected to monotonically increasing loads until failure occurred. Crack driving forces were assessed using the

strain energy release rate, with G_c defined as the critical driving force required for fracture; values were computed from the peak load at failure, P_{max}, and crack length, a, using Eq. 2-1 along with the standard stress intensity solution for C(T) specimens:

$$K_I = \frac{P_{max}}{BW^{\frac{1}{2}}} f_1(\frac{a}{W}), \tag{3-1}$$

where $f_1(\frac{a}{W})$ can be found in [74].

3.3.2. PTLP bonded joints

Interfacial fracture toughness experiments were carried out on fatigue pre-cracked C(T) specimens, tested in room air at 25°C and 20 - 40% relative humidity. Additionally, elevated temperature fracture experiments were conducted at 800°C and 1000°C in an inert, gettered argon environment. For both ambient and elevated temperature tests, pre-cracking was performed by fatigue cycling at room temperature until cracks initiated at a machined notch in the alumina, adjacent to the bonded layer. With continued cycling, cracks were drawn to the interface by modulus mismatch effects, at which point crack propagation occurred along the interface and the cyclic loads were incrementally reduced until the fatigue crack growth rates were on the order of 10^{-10} m/cycle, thus minimizing the size of the cyclic fatigue damage zone. The resulting pre-cracks invariably had a significant portion of the crack front located in the alumina due to crack deviations off the interface during fatigue. Crack driving forces for failure were assessed using the critical strain energy release rate, G_c, as described above.

3.3.3. Bulk alumina

For comparison, fracture properties were also measured for monolithic AD995 alumina. Since AD995 alumina demonstrates rising toughness with crack extension, a crack resistance curve (R-curve) was measured. Specifically, to minimize the initial crack length, fatigue pre-cracks were grown only to Δa_f = 200 - 300 μm prior to measurement of the R-curve, where Δa_f is the length of the fatigue crack extension as measured from the end of the machined notch. Samples were then loaded in displacement control until the onset of cracking, at which point the sample was unloaded to ~ 10 - 20% of the peak load to record the sample compliance at the new crack length. This process was repeated until termination of the test, at which point the compliance and loading data was analyzed to determine fracture energy, G_R, as a function of crack extension, Δa, at which point an R-curve was constructed.

3.4. Cyclic Fatigue Crack Growth Experiments

Long crack (Δa_f > 2 mm) cyclic fatigue crack growth rates were measured in lab air at 25°C (20 - 40% relative humidity) in general accordance with ASTM standard E647 in nominally the same manner for all samples. Some specific modifications for the sandwich test geometry are described below, while other details specific to sandwich samples can be found elsewhere [33,75]. Tests were conducted at a frequency of 25 Hz (sine wave) using servo-hydraulic testing machines at a constant load ratio, $R = P_{min}/P_{max}$, of 0.1, where P_{min} and P_{max} are the minimum and maximum applied loads, respectively. Crack length, a, was continuously monitored on each sample using back-face strain compliance methods with the strain gauge mounted on the alumina adjacent to the metal

layer (Fig. 3.3), or on the center of the back face for bulk alumina samples. For all samples standard compliance calibrations for monolithic C(T) samples were used, which proved to be accurate for the sandwich specimens as verified by direct crack length measurements. Crack driving forces were assessed using the strain energy release rate range, $\Delta G = G_{max} - G_{min}$. Fatigue crack growth rate versus applied driving force (i.e., *da/dN* - ΔG) curves were measured using both increasing and decreasing loading schemes (i.e., under increasing and decreasing ΔG conditions); the later method was used to obtain ΔG_{TH} fatigue thresholds, that were defined as the applied ΔG corresponding to growth rates below ~ 10^{-10} m/cycle. Specifically, cracks were initiated by cycling until stable fatigue cracks formed ahead of the machined notches. Then, the loads were either incrementally reduced to measure the behavior approaching the threshold or increased to obtain the high velocity portion of the crack growth curves. For practical considerations, tests were controlled using the far field applied stress intensity range, ΔK_I^{∞}, with continuous load shedding that limited the ΔK_I^{∞}-gradient ($=1/\Delta K_I^{\infty}[d\Delta K_I^{\infty}/da]$) to ±0.08 mm^{-1}. Ideally, this rate of change in loads would be sufficiently slow to allow the crack blunting or bridging levels to adjust to the current load and level of ΔK_I^{∞} or ΔG.

Short crack (Δa_f < 2 mm) cyclic fatigue crack growth experiments were conducted on bulk alumina samples using the same general procedures outlined above. Cracks were initiated from straight machined notches and data were recorded for the first ~ 2 mm of crack growth, both under increasing and decreasing ΔG conditions. In contrast to long crack testing, short crack fatigue testing specifically does not allow crack bridging levels

to adjust to steady state values prior to data collection; the specific significance of the Δa_f < 2 mm cutoff for short cracks will be discussed along with the results.

3.5. Moisture Assisted Crack Growth Experiments

Moisture assisted crack growth (i.e., stress corrosion cracking) experiments were conducted under static load using fatigue pre-cracked alumina/aluminum sandwich C(T) specimens in a controlled high humidity (> 95% relative humidity) room air environment, where the fatigue pre-cracks initially were located at the interface. Fatigue pre-cracking was performed as described previously and high humidity conditions were maintained by bubbling room air twice through distilled water and into a closed testing chamber. Samples were tested under constant load, i.e., crack driving forces increased with crack extension. To determine crack velocity, *da/dt*, crack lengths were monitored *in situ* using the back face strain signal to estimate the unloading compliance curve. Additionally, crack lengths were periodically verified by the more accurate method of unloading the sample to measure the actual unloading compliance. Samples were initially held at loads where reasonably measurable growth rates ($da/dt > 10^{-9}$ m/sec) could not be achieved. Loads were then step increased and held until measurable growth could be detected at some constant load, at which point all tests were conducted using an increasing loading scheme due to the increasing G field associated with constant loading for the C(T) geometry. When possible, samples were unloaded before critical fracture occurred using computer controlled interlocks. Additional tests were conducted on fatigue pre-cracked ($\Delta a_f > 2$ mm) bulk alumina specimens using the same procedures.

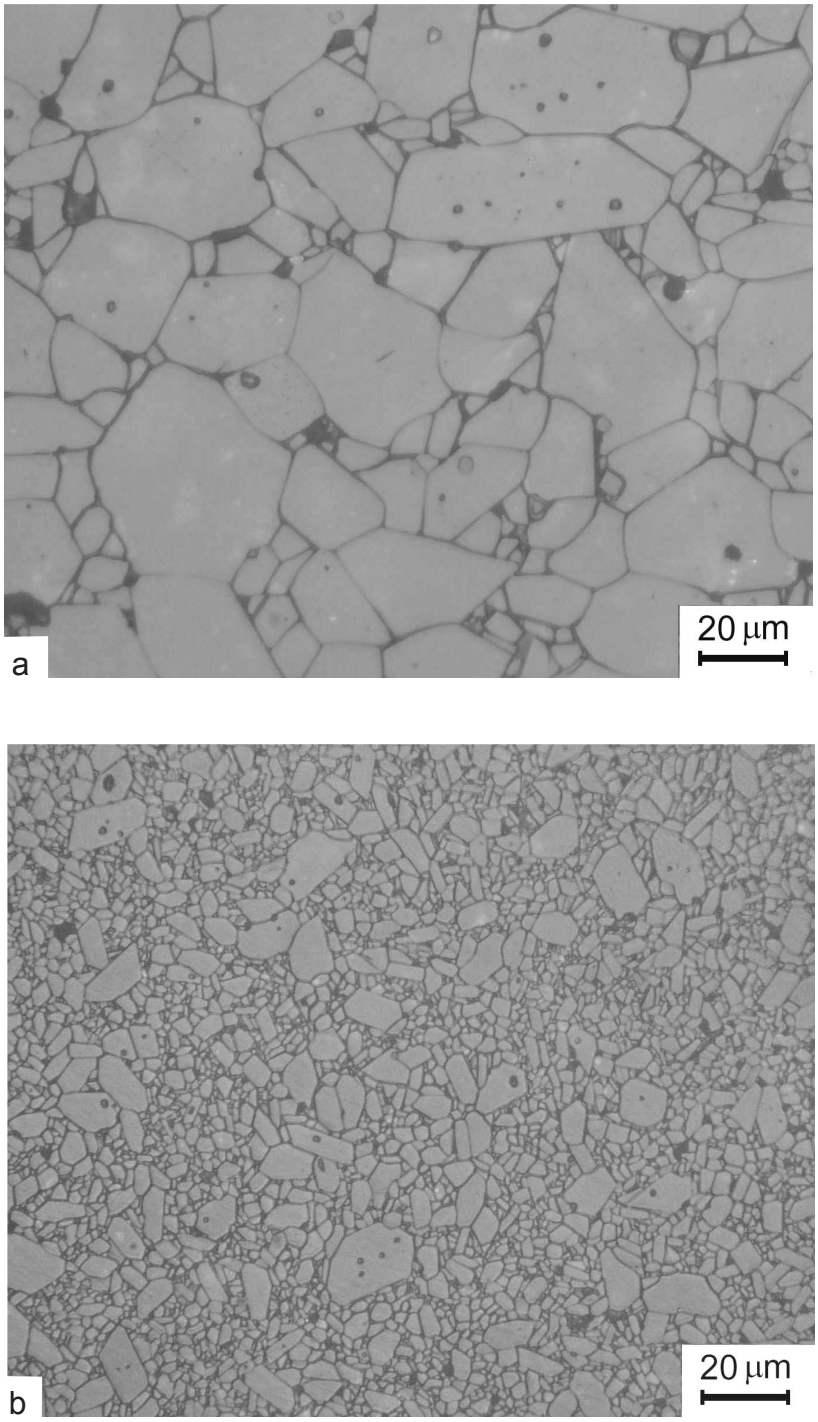

Figure 3.1. Micrographs showing the microstructure of (a) AD995 and (b) AD998 alumina. Samples were thermally etched in air at 1550°C for 30 minutes to reveal grain boundaries.

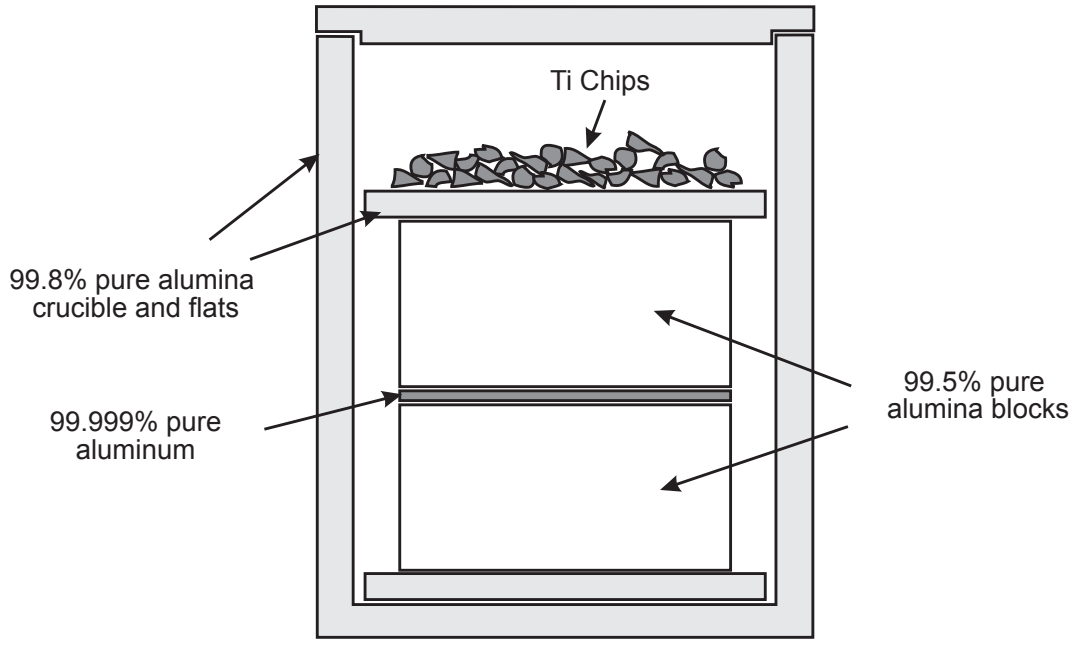

Figure 3.2. Schematic of the alumina/aluminum bonding configuration.

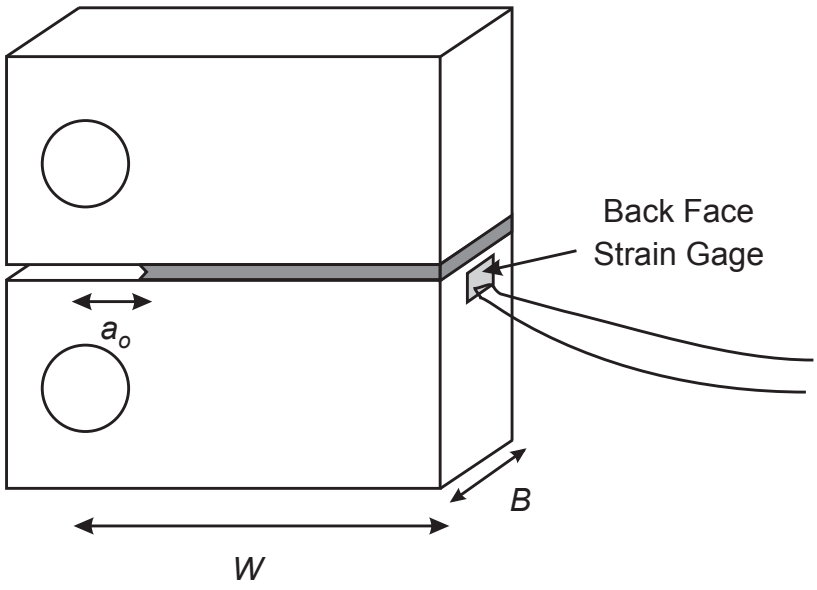

Figure 3.3. Schematic of a compact tension, C(T), sandwich specimen.

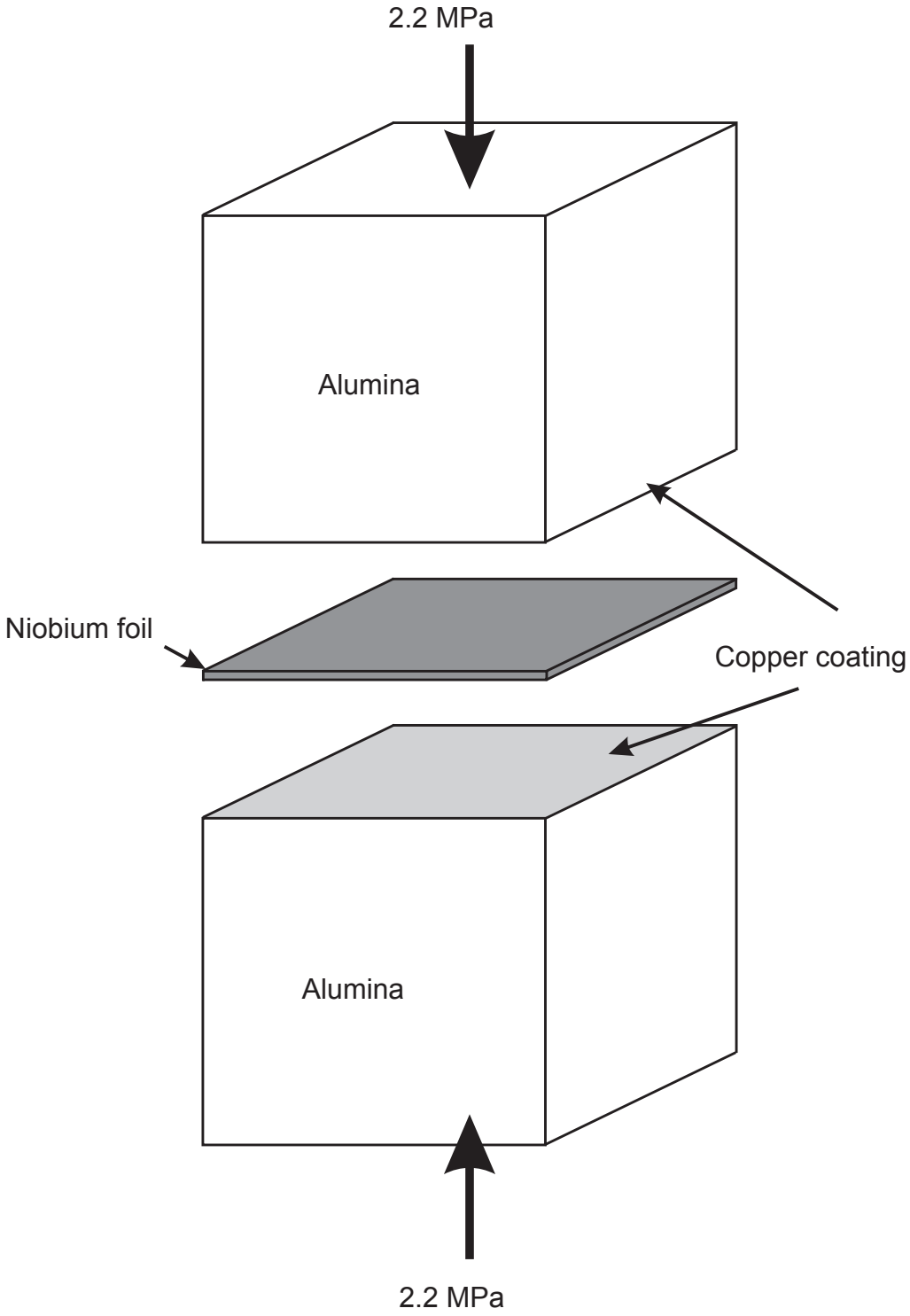

Figure 3.4. Schematic of the PTLP bonding assembly.

CHAPTER 4
STRENGTH AND FRACTURE TOUGHNESS

4.1. Results

4.1.1. Strength of alumina/aluminum/alumina sandwich joints

Results from 3-point bend testing of aluminum joined AD998 alumina beams, shown in Fig. 4.1, demonstrate a trend of increasing strength with decreasing layer thickness over the range of ~ 150 – 20 μm. Observations of the fracture surfaces revealed that in all cases failure initiated by ductile void growth in the metal layer, with this mechanism continuing for the entire failure process in all but the thinnest layer samples. Indeed, micrographs of the fracture surfaces, shown in Fig. 4.2, are characteristic of ductile fracture. For the thinnest layer samples, after initial ductile propagation in the metal, the crack deviated into and propagated in the alumina.

Microvoids appeared to initiate by interfacial debonding at defects at the interface, with direct evidence shown in Fig. 4.3. Fig. 4.3c and 4.3d demonstrate voids where initiation is thought to have occurred at interfacial pores located over alumina grain pullout sites; such grain pullout sites were presumably caused by polishing damage on the alumina surface prior to bonding. Void nucleation initiated by defects at the interface has been observed previously for alumina/alumina interface samples [2,33]. Additionally, for sapphire/aluminum samples, where fewer and smaller defects exist, *in situ* experiments have demonstrated that voids also initiate at the interface [28].

4.1.2. Fracture toughness of alumina/aluminum/alumina sandwich C(T) specimens

A definitive trend of decreasing toughness with decreasing aluminum layer thickness, over the range of 5 – 100 μm, was found for the fatigue pre-cracked alumina/aluminum/alumina sandwich samples (Fig. 4.4). For comparison, the strength results from Fig. 4.1 are also shown on the same plot, demonstrating the opposite trends of toughness and strength with layer thickness. For all samples tested, the fatigue pre-crack, which was located at the interface, was observed to initiate brittle failure in the alumina, with the alumina/aluminum interface remaining intact. Although fracture occurred in the alumina, measured fracture energies for the interface samples were well in excess of the initiation toughness of ~ 20 J/m^2 taken from the measured crack resistance curve (R-curve) for the bulk polycrystalline alumina (Fig. 4.5).

Fig. 4.6 shows *in situ* images, taken in a field emission scanning electron microscope (FESEM), while loading a sandwich C(T) sample up to ultimate failure, which occurred at a fracture energy of 346 J/m^2. The tip of the interface crack in a 100 μm thick layer sample was observed to blunt into the aluminum during loading from 76 to 280 J/m^2. The measured crack tip opening displacement (CTOD) for this sample increased by permanent plastic deformation in the aluminum from sub-micron levels up to ~ 2.6 μm at 280 J/m^2.

4.1.3. Fracture toughness of PTLP bonded joints

At room temperature, the C(T) samples were found to fracture at the alumina/niobium interface at a mean driving force of 39 J/m^2. This value is consistent with the range of fracture energies (9 – 90 J/m^2) that have been reported for diffusion bonded

polycrystalline alumina/niobium samples under mode I loading [4,18,55,56]; however, it is well below the range of 74 - > 2100 J/m^2 that has been exhibited by ultra-high vacuum diffusion bonded alumina/niobium bicrystals processed in various orientations [4,13,57]. Measured room temperature fracture toughness values for the present joints fell roughly in the middle of the range reported for diffusion bonded samples, demonstrating that comparable toughness values can be obtained by utilizing a PTLP bonding process that offers the convenience of potentially lower bonding temperatures and/or pressures.

The interfacial fracture toughness was observed to decrease with increasing temperature up to 1000°C, as shown in Fig. 4.7. The mean fracture energy decreases by almost 50% from 39 J/m^2 at room temperature to 21 J/m^2 at 1000°C. Due to alumina grain pullout during fatigue, pre-cracks typically did not lie entirely at the interface, with a portion of the crack front located in the alumina near the interface. Upon fracture, however, the crack was quickly drawn to the interface and propagated primarily along it with almost no alumina grain pullout. Observations of the fracture surfaces in the FESEM (up to 50,000X) indicate that the niobium debonded from the alumina in an essentially brittle manner with no visible deformation; indeed, imprints of the alumina grain boundaries are visible on the niobium regions of the fracture surface (Fig. 4.8a). Additionally, small regions of Nb_5Si_3, as identified by quantitative energy dispersive spectroscopy (EDS), ranging from ~ 40 to less than 1 micron in size were observed on the alumina sides of the fracture surfaces. These regions also appeared to fracture in a brittle manner with the majority only a few microns in size and located at alumina grain boundaries and triple points (Fig. 4.8); the largest Nb_5Si_3 regions appeared to be located over patches of small alumina grains (Fig. 4.9). In contrast, regions of interfacial copper,

also identified by EDS, deformed plastically and adhered to both sides of the fracture surface (Fig. 4.8).

4.2. Discussion

4.2.1. Trends in strength with layer thickness

The observed trend of increasing strength with decreasing layer thickness is in agreement with that found in previous studies for 100 – 500 μm thick layers, where the increase in strength was attributed to increased constraint of the plasticity in the metal for thinner layers [2,3]; predictions of the observed trends using plasticity theory supported their conclusions [2]. The effects of constraint on a thin ductile layer bonded between liner elastic members can be understood be considering that plastic deformation occurs as an essentially constant volume process. This implies that during tensile plastic deformation, radial contraction of the ductile layer must occur to maintain constant volume. At the interface with an elastic material, in order to maintain geometric compatibility, the contraction of the ductile layer is restricted by the elastic material it is bonded to, raising the stress necessary to cause deformation and failure. This constraint is lost away from the material interface, and thus for thick ductile layers plastic deformation occurs more freely near the center of the layer as compared to thinner layers, lowering the failure stress.

4.2.2. Crack trajectories

During fracture testing for alumina/aluminum specimens, pre-cracks initially located at the interface propagated by crack deviation into the alumina, although the predictions

of Ritchie *et al.* [54] predict the highest local driving force to be in the metal layer for positive β. For PTLP bonded joints, pre-cracks that initially had crack fronts located partially in the alumina were drawn to, and propagated along, the niobium/alumina interface during fracture. Crack deflection towards the interface for PTLP bonded joints is consistent with predictions for positive β values [54]; however, while some highly localized crack deflections into the layer occurred, in general cracks were not observed to deviate off the interface and propagate in the layer as might be expected based on the driving force alone. In order to explain the differences between such predicted and observed behavior, the relative toughnesses of the alumina and layer materials, as well as that of the interface, must be considered in addition to the elastic mismatch effects.

For aluminum joints, crack deviation into the alumina implies that the toughness of the alumina must be significantly lower than that of both the interface and the aluminum layer, and in essence the alumina represents a weakest path that determines the crack trajectory. Conversely, PTLP bonded joints demonstrate slightly more complicated behavior. Crack propagation along the interface suggests that the toughness of the niobium layer is greater than that of the PTLP bonded interface, thus preventing further crack deflection into the metal layer and trapping the crack at the interface. Unlike aluminum joints, however, crack propagation along the interface occurs instead of kinking into the alumina, and thus we can infer that the toughness of the alumina is not significantly lower than that of the PTLP bonded interface.

As mentioned previously, small, local crack deflections into the metal interlayer for PTLP bonded samples occurred, with regions identified as Nb_5Si_3 left on the alumina side of the fracture surface after failure. Crack kinking into the layer appears to occur where

the niobium contacts the alumina grain boundaries and can interact with the intergranular glassy phase, which is assumed to be the source of silicon for the Nb_5Si_3. Local embrittlement of niobium in the presence of silicon has been previously observed to affect crack paths in both PTLP [76] and diffusion [77] bonded alumina/niobium joints; however, previous investigations did not identify such regions as the intermetallic phase Nb_5Si_3. While Sugar *et al.* [76] did not perform quantitative analysis on such regions for their PTLP bonds, Elssner *et al.* [77] identified the particles observed on the fracture surface of their diffusion bonded samples as having composition Nb_4Si by using Auger spectroscopy; however, there is no known stable room temperature niobium silicide with that composition.

4.2.3. Mechanisms of toughening: Role of plastic constraint

For alumina/aluminum joints, samples with 100 μm thick layers demonstrate fracture energies an order of magnitude higher than bulk alumina although final fracture occurs in the alumina for both cases. In order to explain the high measured toughness for these interface samples, it is noted that based on linear elastic fracture mechanics, local stresses near a blunted crack/notch, as in Fig. 4.6, are considerably lower than those ahead of a sharp crack tip at the same applied driving force. For example, using the linear elastic solutions of Creager and Paris [78] to calculate the stresses ahead of a blunt crack/notch with root radius ρ in an isotropic, monolithic material, it can be shown that for any given applied driving force the crack opening stresses, σ_{yy}, are reduced by 42% and 22% relative to the sharp crack case at distances of $\rho/20$ and $\rho/10$ ahead of the crack tip, respectively. Thus, compared to the relatively sharp cracks in the bulk alumina case, a

larger applied driving force is needed for blunted cracks to achieve the stresses necessary to initiate fracture of the alumina, thereby giving a higher measured fracture toughness for the blunt crack sandwich specimens compared to that for bulk alumina.

Additionally, the observed trend of increasing toughness with increasing layer thickness for alumina/aluminum joints (Fig. 4.4) can be explained in terms of the greater crack tip deformation and blunting due to diminished plastic constraint through the thickness of the metal layer for samples with thicker layers. First, to predict if plastic deformation is expected to impinge on the opposite alumina piece and become constrained, plastic zone size estimates[1] can be made for a crack at a bimaterial interface, where plasticity can extend into the aluminum unconstrained (Fig. 2.5). This allows an estimate of the distance, r_{py}, that the plastic zone would like to extend from the lower interface if it did not impinge on the upper metal/ceramic interface. Using the results of Shih and Asaro [23,36], estimates reveal that the plastic zone should extend ~ 100 μm into the aluminum (i.e., comparable to the thickest layers of this study) at a driving force of only ~ 11 J/m^2. This implies that at driving forces necessary for fracture for all alumina/aluminum samples in the present study (> 40 J/m^2), the plastic zone extends across the entire thickness of the aluminum layer and impinges on the ceramic, which limits the amount of plasticity, and in turn the amount of crack tip blunting that can occur. For samples with thin layers, blunting is limited by the thickness of the metal layer at relatively low driving forces, leading to sharper crack tips compared to samples with thicker layers. Direct evidence of increased blunting in 100 μm thick layer samples is seen in Fig. 4.10, which shows a crack in a 100 μm thick layer sample loaded to 488

[1] A flow stress of 50 MPa for the aluminum was used for all plastic zone size calculations in this paper.

J/m^2, where the measured CTOD is comparable to the layer thickness of the 5 μm thick layer samples. Fig. 4.10 demonstrates more highly constrained 5 μm thick layer samples simply cannot blunt enough to reach the high toughness values measured for 100 μm thick layer samples.

To show that increased constraint leads to higher stresses ahead of the crack tip one can look to the results of Varias *et al.* which allow for predictions of the maximum mean hydrostatic stress normalized by yield stress, σ_m/σ_o, ahead of the crack tip [27]. Indeed, the computed maximum value of σ_m/σ_o ahead of the crack tip reaches a level of 6.65 at an applied driving force of ~ 15 J/m^2 and ~ 295 J/m^2 for 5 and 100 μm thick layer samples, respectively. Although these values derive from computations for the centerline crack configuration (Fig. 2.4), it is expected that these predictions are quite reasonable for interface cracks where plasticity extends across the entire layer, and well ahead of the crack tip. Thus, it is implied that at the same applied driving force, samples with thinner, more highly constrained, layers experience higher local stresses ahead of the (sharper) crack tip. Flaws in the alumina ahead of the interfacial crack tip can thus be triggered to failure and cause alumina fracture more easily for samples with thinner aluminum layers due to the more severe stress state.

Additionally, it should be noted that for the samples with 100 μm, and perhaps 35 μm, layer thicknesses, the G_c toughness values calculated from asymptotic stress intensity solutions may underestimate the total fracture energy due to excessive plasticity in the aluminum, i.e., from a violation of small scale yielding assumptions. Using the results from [27], computed plastic zone size estimates in the direction ahead of the crack tip, r_{px}, indicate that at a driving force of 280 J/m^2, the plastic zone already extends > 1

mm ahead of the crack tip for 100 μm thick layer samples, which is not small compared to sample dimensions. Indeed, the work of McNaney *et al.* [33] showed that for layer thicknesses ≥ 100 μm, large scale plasticity with associated load point displacements accounts for a significant fraction of the fracture energy, and accordingly, no trend of decreasing fracture toughness with decreasing layer thickness could be determined when driving forces were calculated using linear elastic solutions. In the present study, however, this expected trend is observed since plasticity is limited in samples with 5 and 35 μm thick layers such that small scale yielding assumptions are reasonable and crack tip plasticity only represents a small perturbation in the asymptotic, linear elastic solutions. Accordingly, it is expected that the trend seen in Fig. 4.4 would be more pronounced if large scale plasticity were taken into account in the calculation of the crack driving forces for the samples with 100 μm, and possibly 35 μm, thick layers.

4.2.4. Mechanisms of toughening: Role of interfacial ductile phase

Based on observations of fracture surfaces, several features have been identified which may have an influence on the fracture properties of the PTLP bonded samples. While interfacial porosity and brittle pullout/fracture of Nb_5Si_3 particles are considered to have minor effects on the measured crack resistance, the observed ductile tearing of copper particles is expected to play a more significant role, and will be the focus of further discussion.

Under monotonic loading at both ambient and elevated temperatures, fracture of PTLP bonded joints occurred by essentially brittle separation of the alumina/niobium interface accompanied by ductile tearing of the copper regions. No deformation or slip steps were

observed on the niobium side of the fracture surface, which is in contrast to observations made on UHV bonded bicrystals, which showed distinct slip steps on the fracture surfaces as a result of plastic deformation [14,58]. While the strain rate sensitivity of niobium is expected to play a role in reducing deformation during fast fracture, no deformation was found at the critical fracture initiation point where the loading rate was moderate and more deformation should be expected. Possible explanations for this difference may be a much higher yield strength for the polycrystalline niobium in the present case due to impurity uptake during bonding and/or a decrease in the work of attraction, W_{at}, due to copper adsorbed on the interface allowing interface failure at lower toughness values.

In order to estimate the niobium yield strength, Vickers microhardness measurements were taken on a fine polished surface on the side of a sample giving HV = 1.7 GPa; this was about 25% less than values found on the fracture surface. Assuming the Vickers hardness to be roughly three times the yield stress, it is implied that the niobium layer may have a yield stress in excess of 550 MPa, or up to an order of magnitude higher than the estimates for the niobium single crystals used in [4,13,14,57,58]. This difference in yield strength may account in part for the lower fracture energies and lack of observed slip steps for the present samples. Additionally, as mentioned previously, adsorbed silver has been found to drastically decrease the toughness of UHV bonded bicrystals by lowering W_{at}, thereby decreasing the ability for cracks to blunt or deform the niobium [14,57]. For the present case, copper may play a similar role in reducing the W_{at}, thereby lowering the measured toughness and reducing the propensity for blunting.

In contrast to the niobium, as the interface crack encountered a copper region during fracture, it was visibly plastically deformed, absorbing energy, which in turn provided toughening by contributing to the measured fracture energy. This toughening mechanism is analogous to that seen in ductile phase reinforced composites, where distributed ductile phases are used to increase the toughness of brittle materials [79-82]. Indeed, deformed copper regions on the fracture surfaces in the present study look identical in morphology to deformed aluminum on the fracture surface of an aluminum reinforced alumina composite [80].

A rough estimate of the toughening contribution from the ductile copper phase can be made by using an expression developed for ductile phase reinforced brittle composites [59,80,83]:

$$\delta G_c = V_f \sigma_o t \chi \tag{4-1}$$

where V_f is the volume fraction, σ_o is the yield strength, and t is the radius of the reinforcing phase, while χ is a work of rupture parameter. In the present case, χ is expected to be approximately 1 for a fully ductile ligament [80]. Estimating the yield strength for fully annealed copper to be approximately 100 MPa and using a measured average copper partical radius of ~ 2 μm, we predict a toughening contribution of 22 J/m^2, or ~ 60% of the room temperature fracture energy. As the temperature is increased towards the melting point of the copper ($T_{mp} \approx 1083°C$), the yield strength of copper is expected to decrease, lowering the toughening contribution. Indeed, the 18 J/m^2 drop in fracture energy that was observed for fracture at 1000°C is consitant with the loss of most of the toughening contribution from the plastic work associated with the deformation of the interfacial copper; however, lacking further evidence it is currently unclear whether

this is indeed the primary factor causing the decrease in toughness with increasing temperature.

The above result implies that the intrisic toughness of the alumina/niobium interface may be only ~ 17 J/m^2, which is not unreasonable considering that an interfacial crack path is observed. If the intrinsic alumina/niobium interface toughness was significantly higher than the initiation toughness of the alumina (~ 20 J/m^2), crack kinking into the alumina would be expected. Since an interfacial crack path is observed, however, it is expected that the intrisic alumina/niobium interface toughness should be comparable or lower than that of the alumina, which is consistant with a fracture energy of ~ 17 J/m^2.

4.2.5. Reliability of joints

Comparisons of the mechanical properties of joints to that of the bulk material, in this case alumina, are essential for reliability predictions in joined components. For aluminum/alumina joints, samples with 100 μm thick layers demonstrate toughness an order of magnitude higher than bulk alumina; however, most of this benefit is lost for 5 μm thick layers. Additionally, it is important to note that while joint strength is known to increase with decreasing layer thickness, the present work clearly demonstrates that this advantage comes at the expense of fracture toughness. As anticipated, this reaffirms that many factors in addition to strength must be considered when engineering metal/ceramic interface systems for optimal mechanical properties. Additionally, this result is not surprising when put in the more general context of fracture of ductile materials, where increased strength has long been known to reduce the toughness of metal alloys via reduced crack tip blunting and plastic work during fracture. This can be understood by

noting that for homogeneous ductile materials the crack tip opening displacement, CTOD, under small scale yielding conditions may be approximated as [84]:

$$\text{CTOD} = G/\sigma_o \qquad (4\text{-}2)$$

where σ_o is the yield strength. Thus, by raising the yield strength, the CTOD is smaller, and the crack tip is sharper, for any given applied strain energy release rate. As a result of such sharper crack tips, the near tip stresses necessary to cause fracture may be reached at a lower applied *G*, and thus decreasing fracture toughness is often observed with increasing strength.

Previous investigations have shown the strength of the PTLP bonded joints to be comparable to that of the alumina used, with the majority of failures occurring in the alumina away from the interface [66,67]. Fracture toughness tests in the present work have demonstrated a mean interfacial fracture toughness of 39 J/m^2 at room temperature, while the bulk alumina exhibited rising R-curve behavior, with an initiation toughness of ~ 20 J/m^2 and toughness values increasing to > 40 J/m^2 (i.e., greater than that of the interface) after ~ 1 mm of crack extension (Fig. 4.5). R-curve behavior for bulk alumina is well understood and is attributed to the frictional tractions that develop along the fractured grain boundaries in the crack wake, creating grain bridges that sustain part of the load and shield the crack tip from a portion of the applied driving force [85-87]. As the crack extends and grain bridges develop, resistance to crack growth increases as seen in Fig. 4.5.

In comparing properties, it must be considered that the several millimeter long fatigue pre-cracks used for the measurement of interfacial fracture toughness were located at least in part in the alumina, and thus alumina grain bridges in the wake of the pre-cracks

may have contributed in part to the measured interfacial fracture toughness. This implies that the measured toughness values may only provide an upper bound to the actual interfacial fracture toughness, i.e., that the interfacial fracture toughness is roughly comparable to that of < 1 mm long cracks in the bulk alumina. While bulk alumina has superior fracture toughness in situations where initial cracks are > 1 mm in length, the presence of such long cracks in a brittle material is often detrimental to the overall mechanical properties and thus, in most practical cases, the benefits of higher toughness would not be realized.

4.3. Conclusions

Based on an experimental study of the strength and interfacial/near interfacial fracture toughness of liquid state bonded alumina/aluminum sandwich joints and partial transient liquid phase bonded joints consisting of alumina bonded with copper/niobium/copper interlayers, the following conclusions may be made:

1. Alumina/aluminum joints were found to fail in 3-point bending by ductile microvoid growth and coalescence, where microvoids appeared to initiate at defects at the interface. A trend of increasing strength with decreasing layer thickness was observed and attributed to increases in the amount of plastic constraint within the aluminum layer as the thickness was decreased.
2. During fracture toughness testing, failure of alumina/aluminum joints occurred by interfacial pre-cracks deviating into and propagating in the alumina. In contrast to strength, the fracture toughness of the alumina/aluminum layered samples was seen to decrease with decreasing aluminum layer thickness; this trend rationalized in terms of

diminished crack tip deformation and blunting in the thinner metal layers (where plastic deformation is more constrained), which raised the local crack tip stresses relative to those needed to trigger cracking at flaws in the alumina.

3. At ambient temperatures, fracture of PTLP bonded joints occurred at the alumina/niobium interface in a brittle manner, with a mean interfacial fracture toughness of 39 J/m^2. This toughness is comparable with the average toughness of standard diffusion bonded niobium/alumina, but the bonds are far more convenient to fabricate.
4. Such failures of PTLP bonded joints at ambient temperatures are associated with niobium/alumina interfacial separation with regions of interfacial copper deforming in a ductile manner and adhering to both sides of the fracture surface. Energy absorbed during the ductile tearing of the copper provides toughening to the PTLP bonded joint by contributing to the total measured fracture energy.
5. Fracture toughness values of PTLP bonded joints were observed to decrease by ~50% as the temperature was raised from 25° to 1000°C; this decrease was attributed at least in part to a reduced toughening contribution from the plastic work associated with the deformation of the copper phase at temperatures near its melting point.
6. By comparing the fracture properties of the alumina/aluminum and PTLP bonded joints to that of bulk alumina, it is concluded for both cases that the presence of the joints does not appear to be detrimental to the overall flaw tolerance of the bonded ceramic structure. Toughness values for joints ranged from an order of magnitude higher than bulk alumina for 100 μm thick alumina/aluminum joints to slightly higher for 5 μm thick alumina/aluminum joints and PTLP bonded joints.

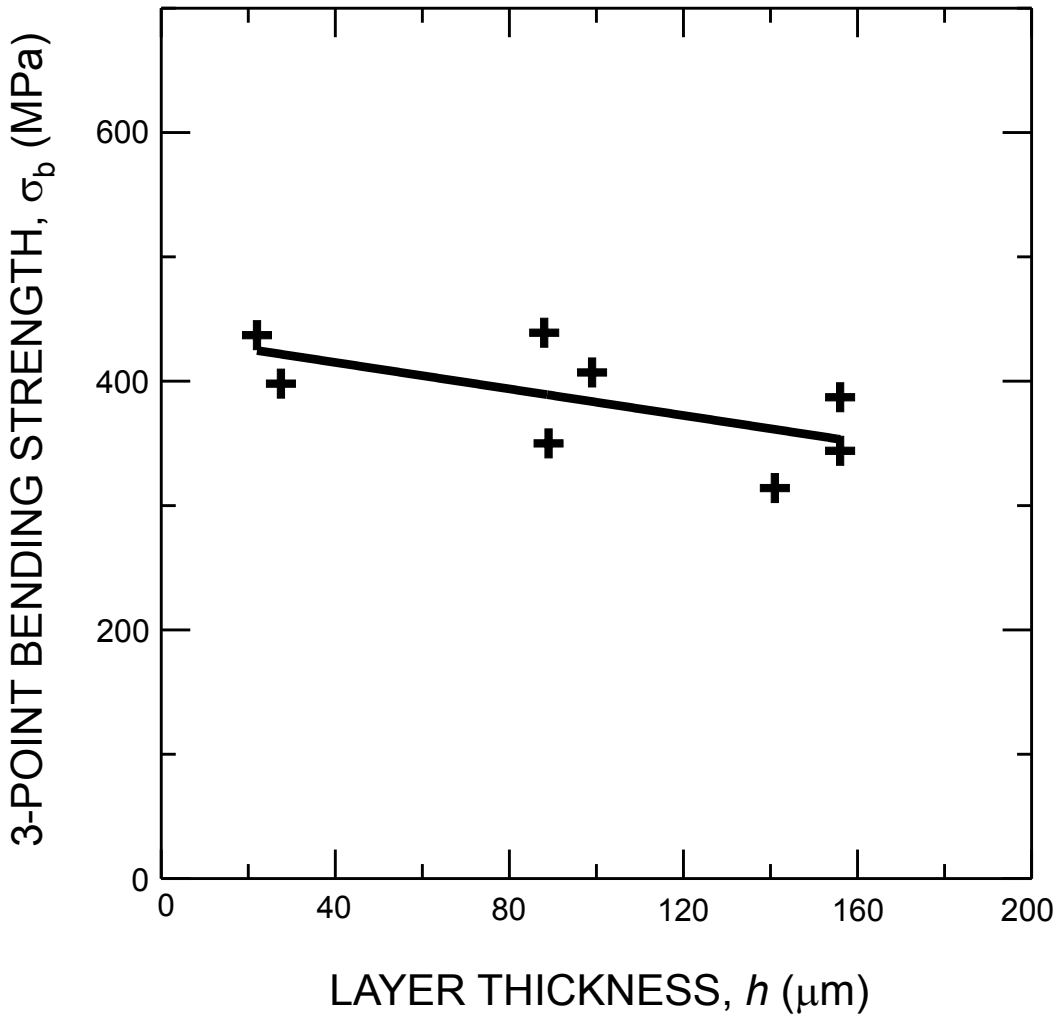

Figure 4.1. Plot of the 3-point bending strength of alumina/aluminum joints demonstrating an increase in strength with decreasing layer thickness. Each data point corresponds to an individual sample that was tested.

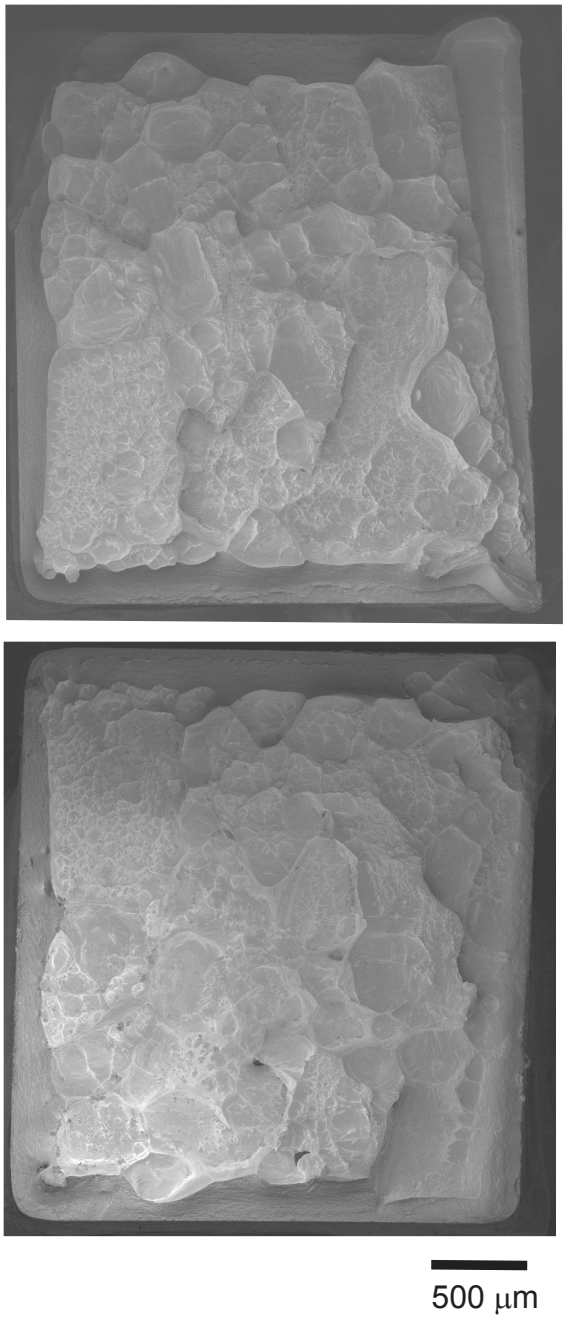

Figure 4.2. Micrographs showing the fracture surface of a 3-point bending specimen.

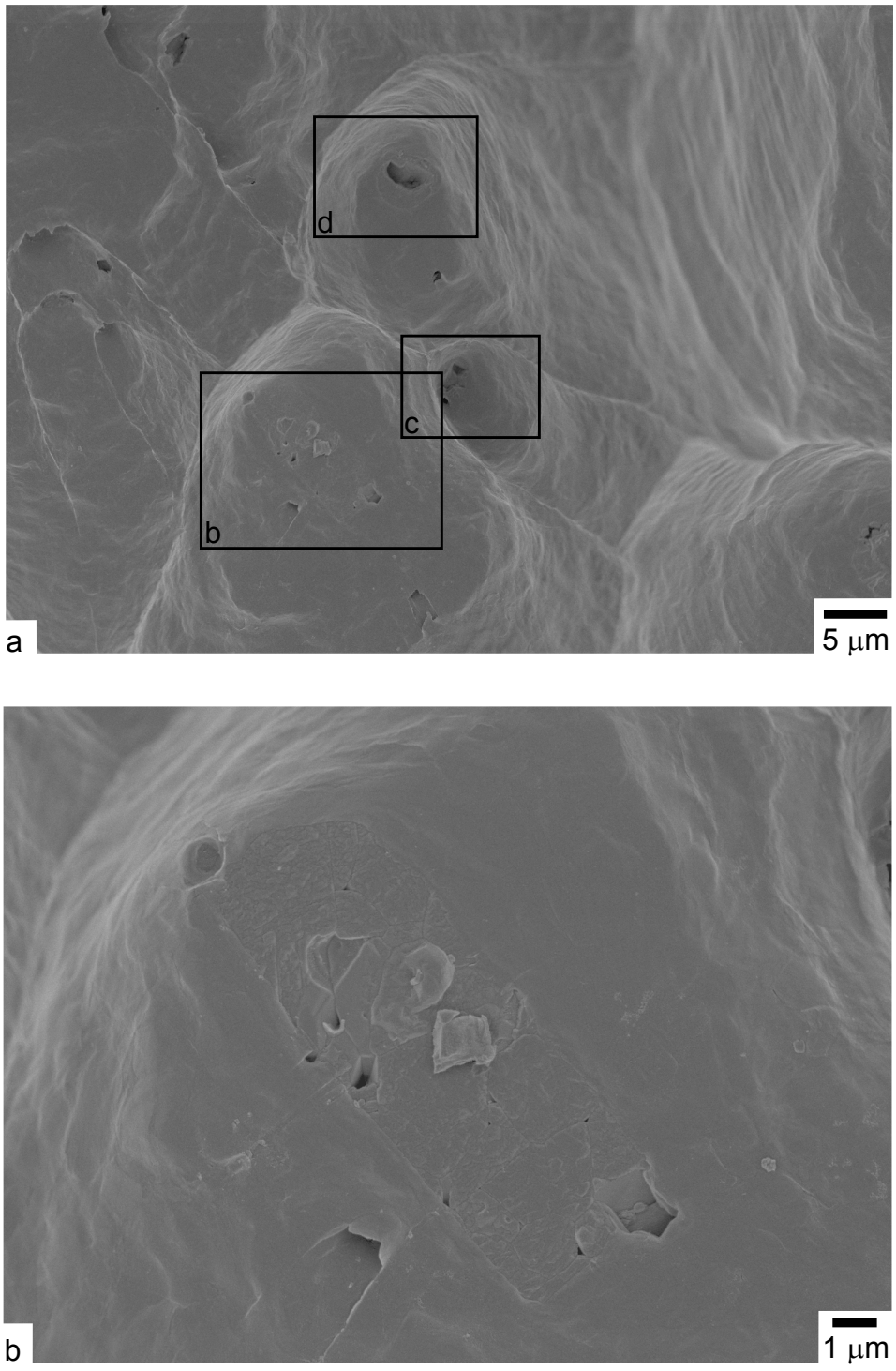

Figure 4.3. (a) Micrograph showing microvoids on the fracture surface of a 3-point bend specimen; (b), (c), and (d) show interfacial defects where microvoids are believed to have initiated from.

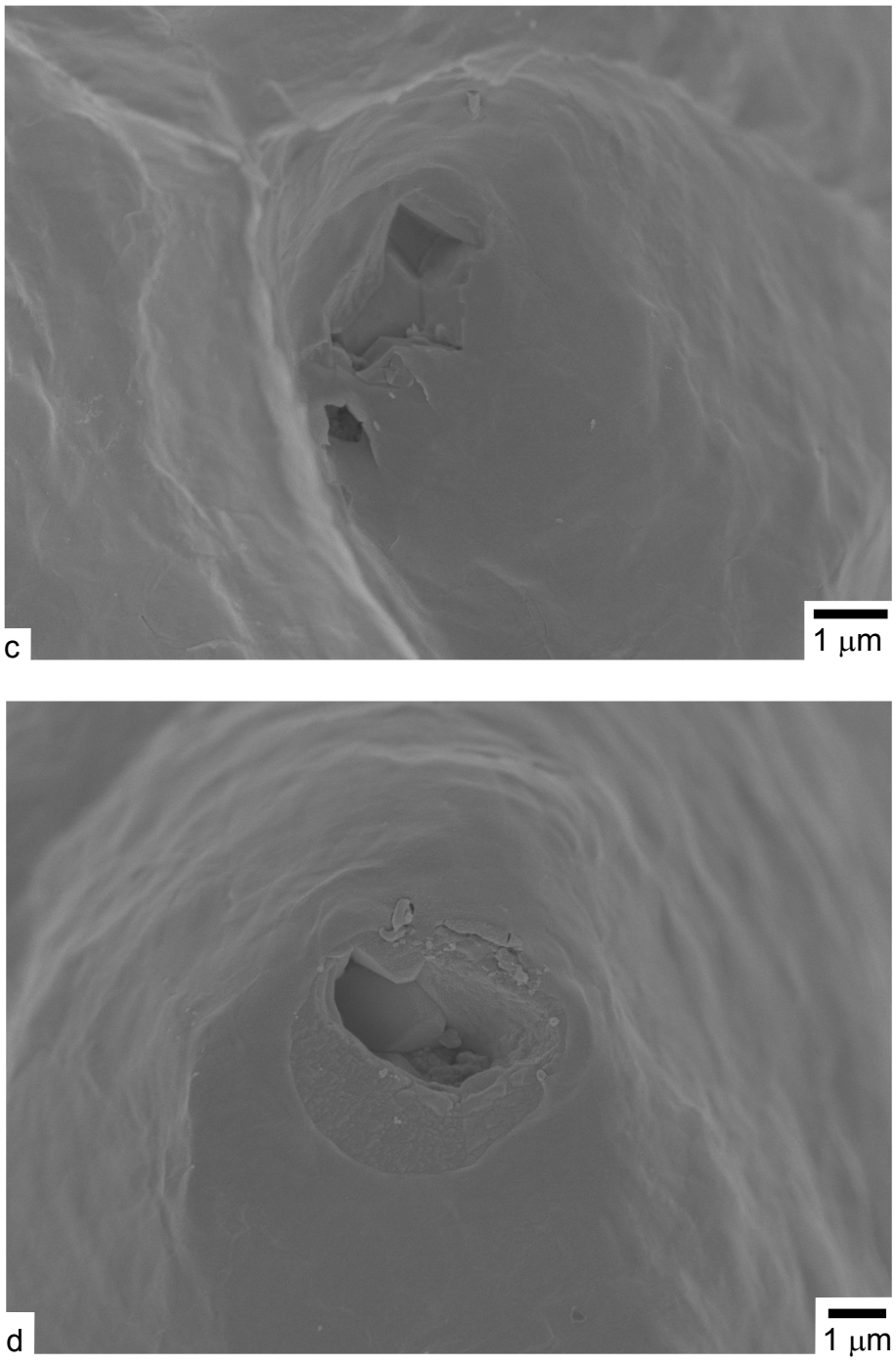

Figure 4.3. continued.

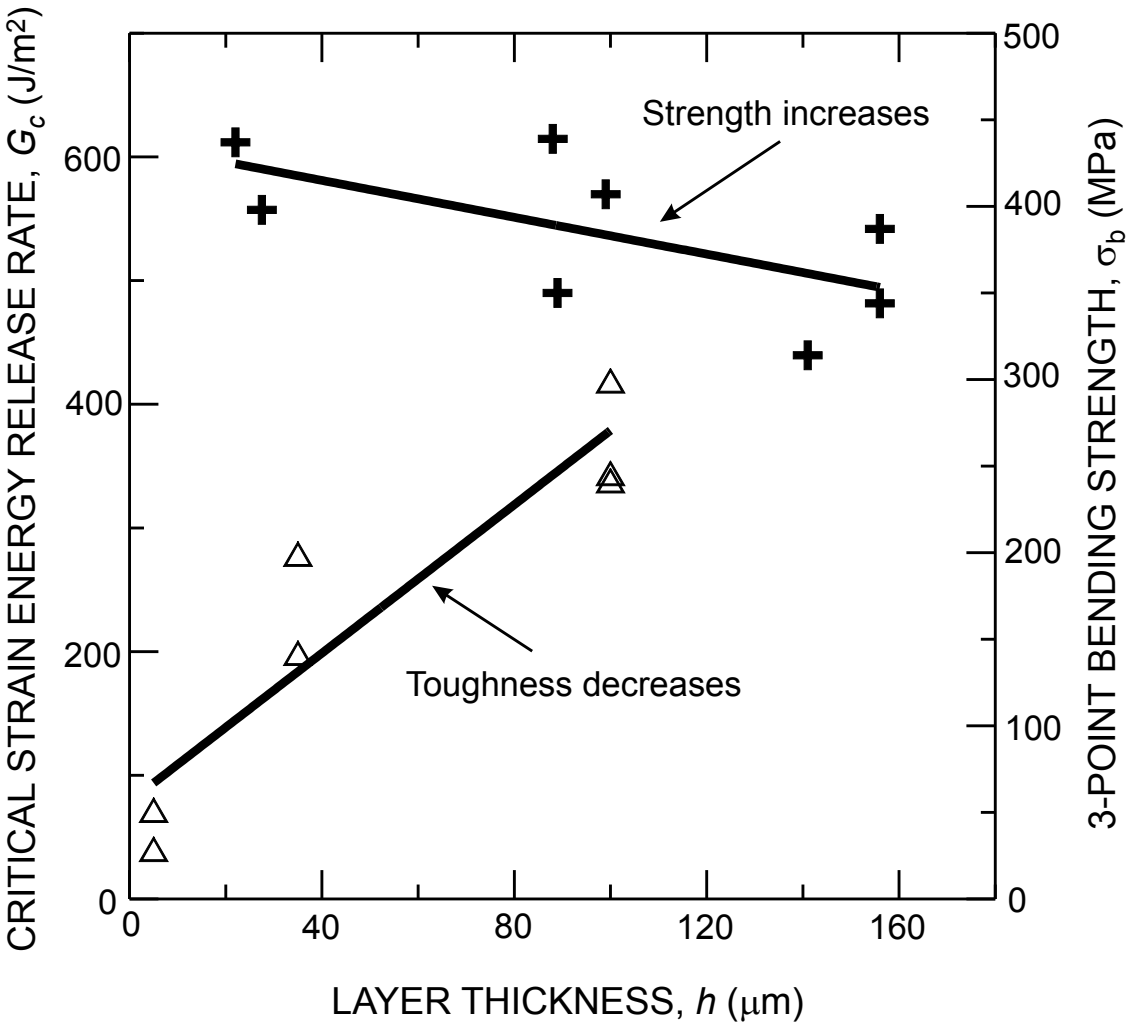

Figure 4.4. Fracture toughness of alumina/aluminum sandwich samples plotted as a function of aluminum layer thickness. Strength data from Fig. 4.1 is plotted as well for comparison. Note the opposite trends of strength and toughness with changing layer thickness. Each data point corresponds to an individual sample that was tested.

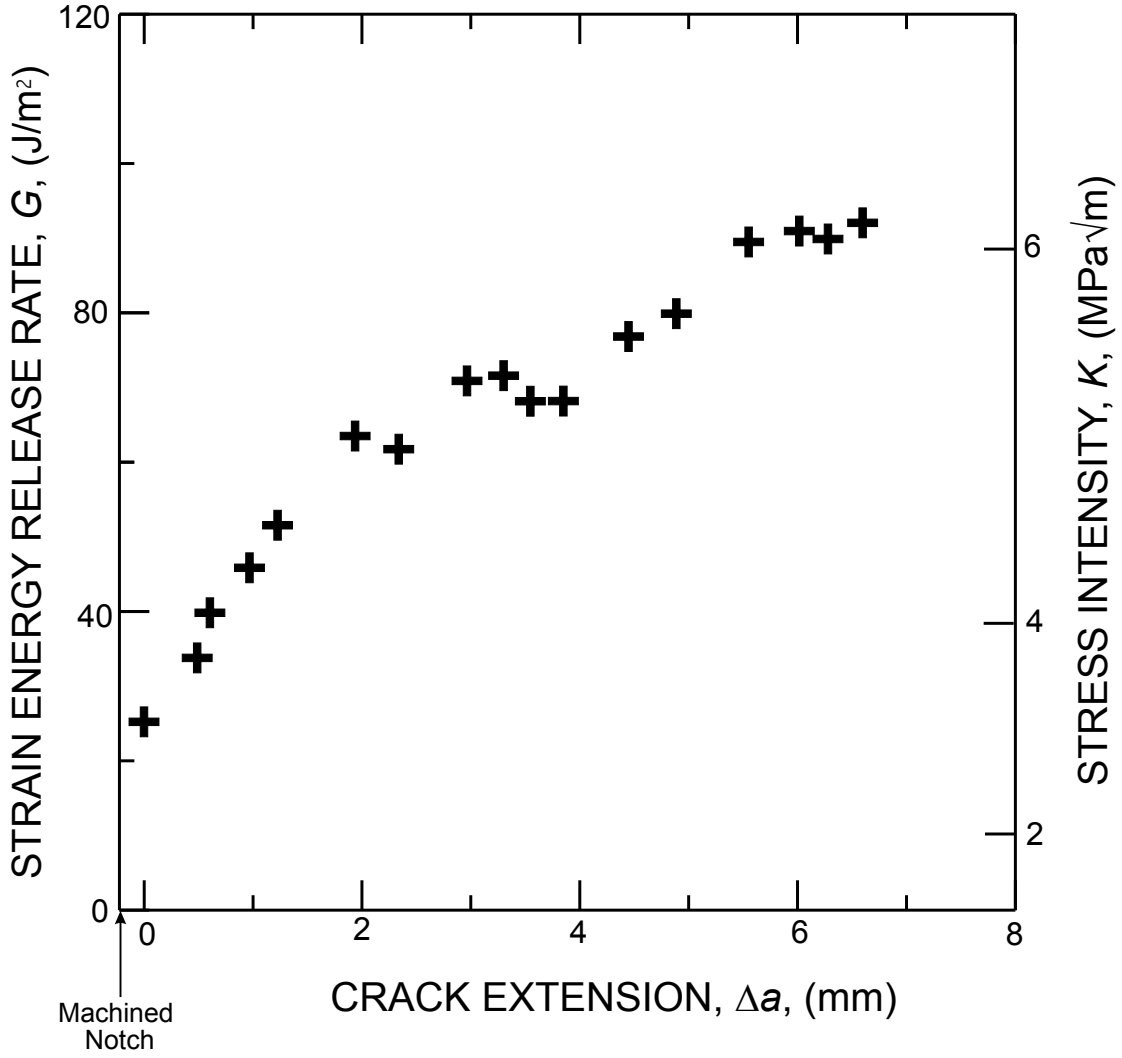

Figure 4.5. R-curve measured for Coors AD995 alumina demonstrating rising crack growth resistance with crack extension. Data shown were collected from a fatigue pre-cracked C(T) sample where the pre-crack was grown only 230 μm from the machined notch to minimize the initial crack length.

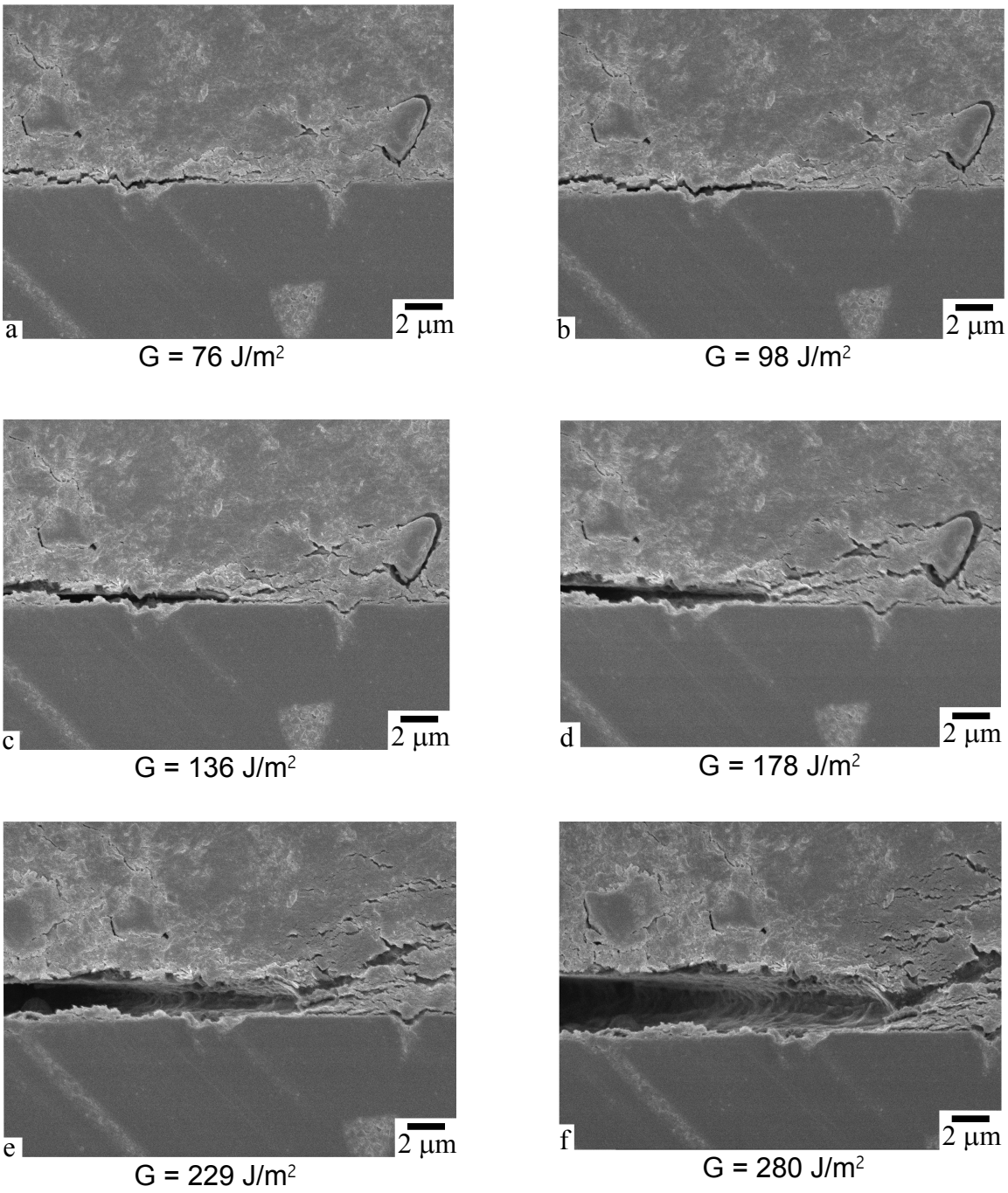

Figure 4.6. Blunting of an interfacial crack into a 100 μm thick aluminum layer during loading *in situ* in the FESEM as the applied driving force was increased from 76 to 280 J/m^2. The sample failed at an applied driving force of 346 J/m^2 in the alumina.

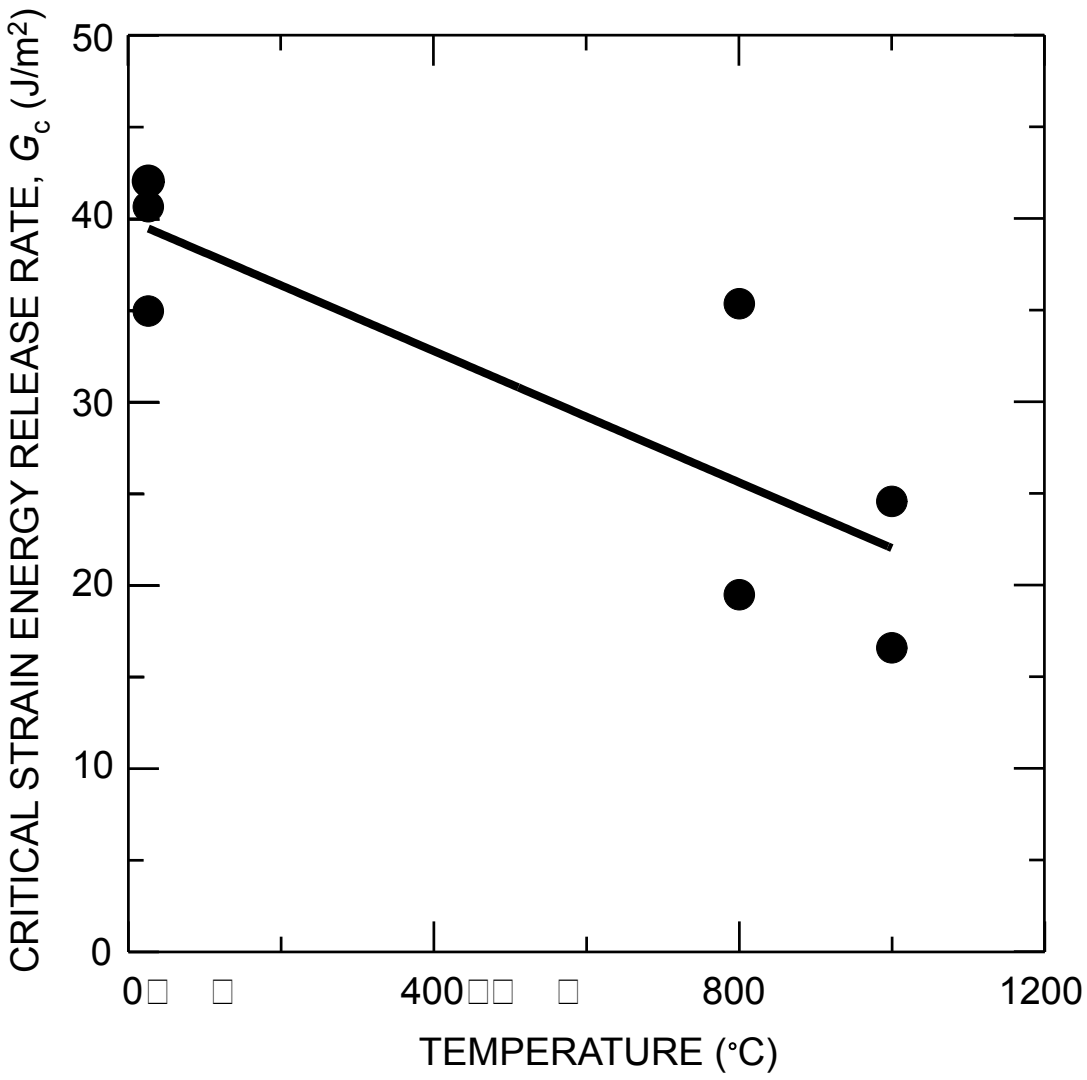

Figure 4.7. Interfacial fracture toughness of PTLP bonded joints as a function of temperature. Elevated temperature tests were performed in gettered argon. Each data point corresponds to an individual sample that was tested.

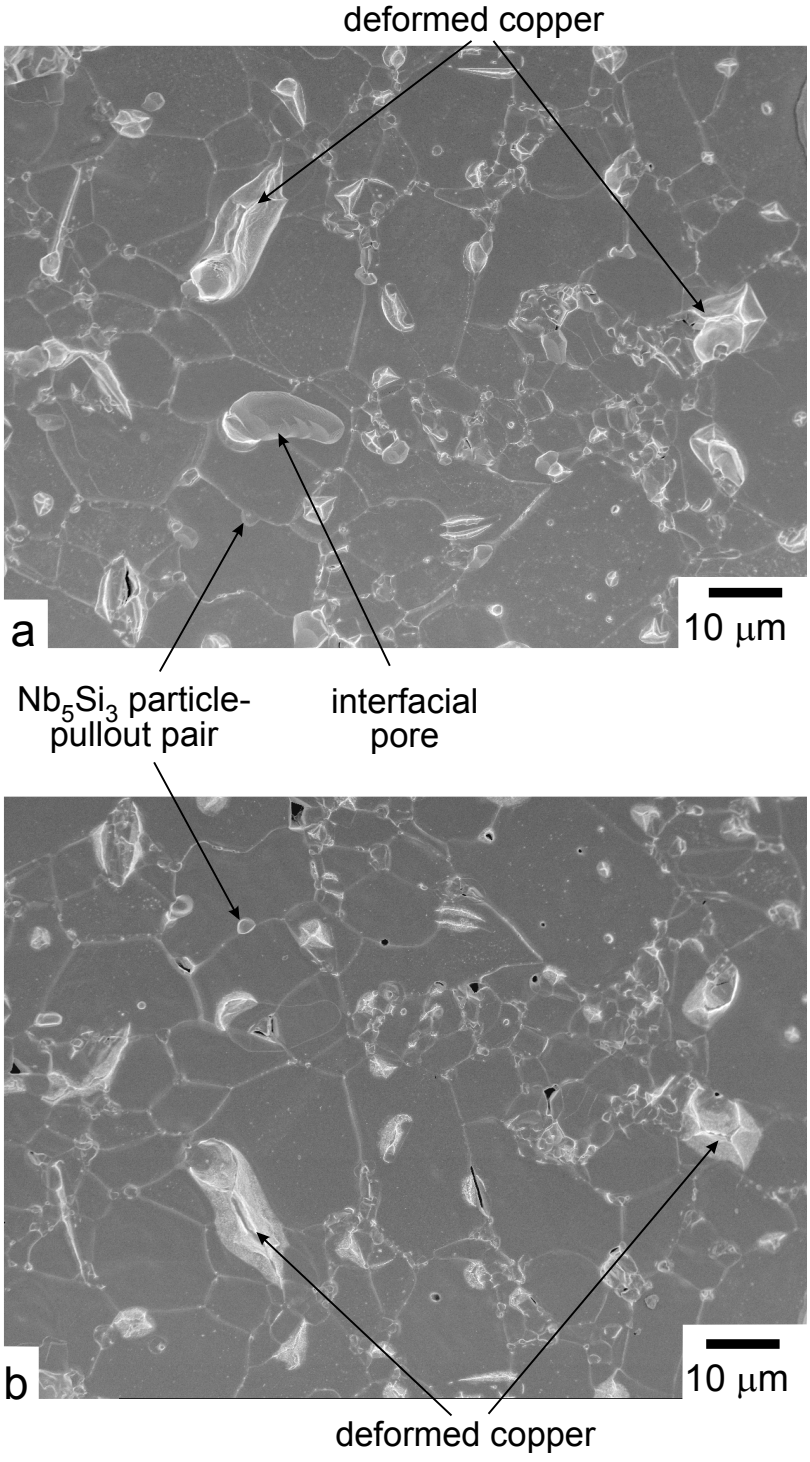

Figure 4.8. Matching micrographs of the (a) niobium and (b) alumina side of the fast fracture surfaces. The deformed copper regions are seen adhered to both sides of the fracture surface while Nb_5Si_3 particles are seen only on alumina side. Grain boundary grooving is evident in the alumina, with matching imprints appearing in the niobium. Direction of crack propagation was left to right with respect to the micrograph.

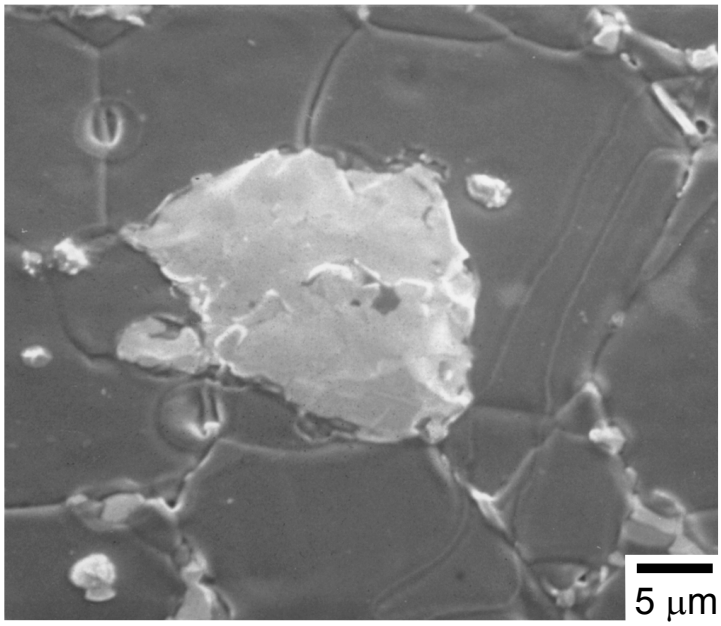

Figure 4.9. Micrograph of a large Nb_5Si_3 particle on the alumina side of the fast fracture surface that was used for quantitative EDS measurements. Direction of crack propagation was left to right with respect to the micrograph.

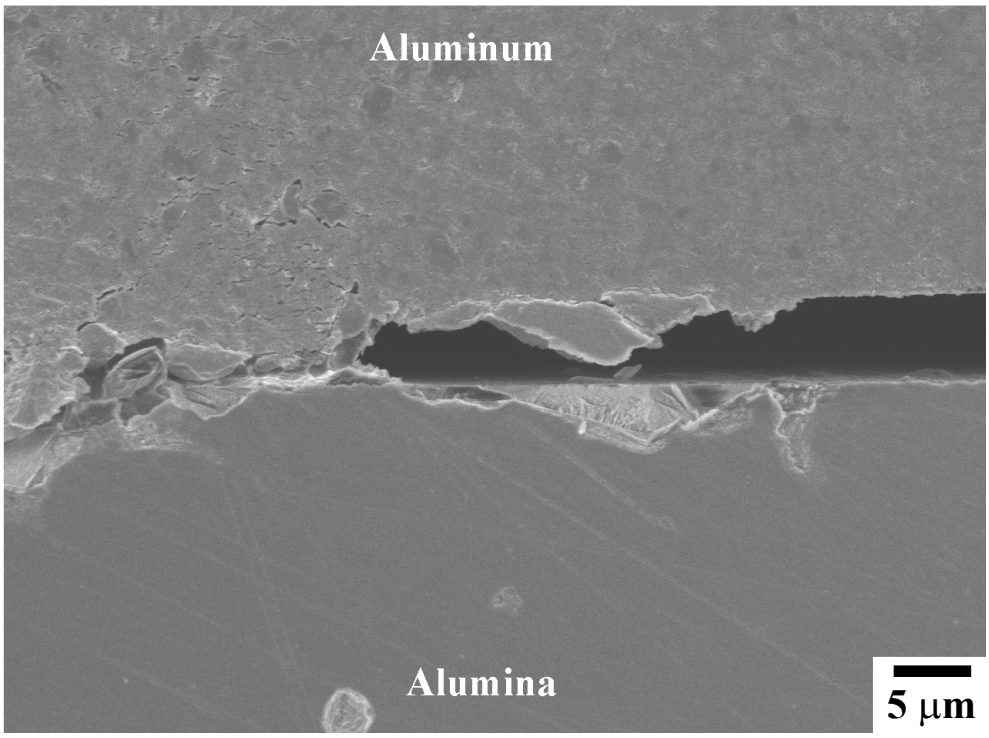

Figure 4.10. Crack tip blunting in a 100 μm thick layer sample loaded *in situ* in the FESEM to 480 J/m^2. Note the opening displacement is on the order of 5 μm.

CHAPTER 5
CYCLIC FATIGUE CRACK GROWTH

5.1. Results

5.1.1. Fatigue crack growth in alumina/aluminum/alumina sandwich C(T) specimens

A trend of increasing fatigue crack growth resistance with decreasing aluminum layer thickness was observed for cyclic fatigue of alumina/aluminum/alumina sandwich samples in the near threshold regime, with crack propagation occurring exactly at the interface for all data shown in Fig. 5.1. Samples with 5 μm thick aluminum layers showed a factor of two higher fatigue threshold compared to 100 μm thick layer samples, as well as an order of magnitude lower growth rates at comparable driving forces in the near threshold regime, while samples with 35 μm thick layers exhibited intermediate behavior in both regards. Data from McNaney *et al.* [33], using samples with 100 to 500 μm thick layers where no such trend was observed, are also shown for comparison.

Evidence for the presence of fatigue striations on the aluminum side of the fatigue fracture surface was seen for all layer thicknesses (Fig. 5.2). Additionally, examination of the fatigue surface of 5 μm thick layer samples after failure revealed a crack path alternating between one interface and the other during fatigue crack growth (Fig. 5.3a). While macroscopic jumps of the entire crack front from one interface to another were not uncommon for all samples, the additional localized jumps seen in Fig. 5.3a, distributed across the fracture surface, were unique to 5 μm thick layer samples. Observations of crack profiles in unbroken samples (Fig. 5.3b) revealed such jumping to be initiated predominantly at flaws in the alumina microstructure. In Fig. 5.3b the crack, originally

propagating on the upper interface, re-initiated on the other side of the layer at a flaw in the alumina; it then grew to, and propagated along, the lower interface.

While samples with ≥ 100 μm thick layers from this study and others [33] demonstrated primarily interfacial fatigue crack growth at all driving forces, for samples with 5 μm thick aluminum layers, fatigue cracks were found to leave the interface and grow into the alumina as driving forces were increased. Data for the stable crack growth in the alumina for the 5 μm thick layer samples are represented by open symbols in Fig. 5.4. Data for large cracks in bulk AD995 alumina, where the amount of fatigue crack extension from the machined notch, Δa_f, was greater than 2 mm, are also shown in Fig. 5.4 for reference. For the 5 μm thick aluminum layers, crack growth in the alumina initially occurred at driving forces lower than necessary for growth of large cracks in bulk AD995 alumina (Fig. 5.4); data for the two cases only merged after > 2 mm of crack growth.

5.1.2. Fatigue of PTLP bonded joints

Under fatigue loading, cracks propagated at or near the niobium/alumina interface with various amounts of alumina grain pullout (i.e., excursions of the crack into the alumina). Resulting fatigue crack growth rates, da/dN, at room temperature are shown in Fig. 5.5 and are compared with corresponding data collected for large (Δa_f > 2 mm) fatigue cracks propagating in bulk alumina samples. The fatigue crack growth rate behavior can be expressed in terms of a standard fatigue (Paris) power law:

$$da / dN \propto \Delta G^m , \qquad (5\text{-}1)$$

with the power-law exponents, *m*, ranging from 10 to 50 for the four samples shown. These exponents are far larger than those commonly measured in metallic alloys but are similar to those found for the cyclic fatigue of brittle materials [88]; for example, the results measured in the present investigation for bulk AD995 alumina display a power-law exponent of ~ 50.

With respect to the crack path, the amount of ceramic grain pullout during fatigue crack growth varied quite widely, with alumina grains covering from ~ 50% to nearly 100% of the niobium side of the fracture surface. Representative micrographs of samples demonstrating each case are shown in Fig. 5.6. For the latter case, cracks propagated mostly in the alumina; however, they were constantly drawn back to the interface, resulting in a near interfacial crack path. Interface samples in which the fatigue crack propagated primarily in the alumina exhibited growth rates and power-law exponents comparable to that of monolithic Coors AD995 alumina (Fig. 5.5).

Samples with less alumina grain pullout had appreciable portions of the crack front propagating at the niobium/alumina interface and demonstrated less fatigue crack growth resistance. Indeed, samples with ~ 100% coverage of alumina grains on the fatigue fracture surface exhibited fatigue crack growth thresholds ~ 50% higher when compared with samples with only ~ 50% coverage. Fatigue fracture surfaces in regions where the fatigue crack grew at the interface (Fig. 5.7) looked similar to that of fast fracture (Fig. 4.8); the only notable difference was in the morphology of the copper regions. Copper regions at the PTLP bonded joint interface adhered to both sides of the fatigue fracture surface and appeared deformed; however, in the case of fatigue, these regions appeared flattened due to the cyclic loading with evidence of partial copper/alumina interface

failure in some places (Fig. 5.7). In contrast to alumina/aluminum joints, scanning electron microscopy revealed no visible deformation or fatigue markings (e.g., fatigue striations or beachmarks) on the niobium portions of the fatigue fracture surface at magnifications up to ~ 50,000X. Indeed, as in fast fracture, imprints of the alumina grain boundaries were still clearly visible in the niobium after fatigue failure, implying a relatively brittle debonding mechanism in these regions (Fig. 5.7). Finally, small, local crack deflections into the metal interlayer occurred under cyclic loading, specifically at particles of Nb_5Si_3 as was described for fast fracture in Chapter 4.

5.1.3. Fatigue of AD995 alumina: Long and short crack results

While long crack (Δa_f > 2 mm) fatigue results have been presented in both Figs. 5.4 and 5.5, short crack (Δa_f < 2 mm) fatigue data for AD995 alumina are additionally presented in Fig. 5.8. Behavior of short fatigue cracks differed greatly from that of long cracks. Specifically, when tested under decreasing ΔG conditions, fatigue crack growth rates decreased with decreasing ΔG similarly to long cracks; however, significantly lower applied driving forces were need for crack growth. Additionally, short fatigue cracks demonstrated a lower fatigue threshold than long cracks. Under increasing ΔG conditions, behavior was very different from that of long cracks, with crack growth rates initially decreasing with increasing driving force before finally increasing and merging with the long crack data. This behavior resulted in a V-shaped *da/dN* - ΔG curve (Fig. 5.8), with short crack data only merging with long crack data after approximately 2 mm of growth.

5.2. Discussion

5.2.1. Crack trajectories

As in fast fracture, in no case did fatigue failure occur in the metal layer, which would be the highest driving force direction based on the modulus mismatch ($\beta > 0$) for the alumina/aluminum and PTLP joints, and accordingly the relative fatigue crack growth resistance of each crack path must be considered when rationalizing crack paths. Extension of the results of Ritchie *et al.* [54] for monotonic fracture to cyclic loading is considered reasonable since stage II ductile fatigue (i.e., ductile fatigue associated with fatigue striations) occurs on a mode I path ($K_{II} = 0$) [89]. Additionally, for grain bridging ceramics such as alumina, fatigue is typically a result of the degradation of toughening (e.g. grain bridging) with the associated crack extension a result the same mechanisms found for monotonic fracture, and accordingly the same $K_{II} = 0$ crack paths are observed [90-94]; further details on brittle fatigue mechanisms will be described below. Accordingly, the results of Ritchie *et al.* [54] will be used to infer information about the relative fatigue crack growth resistance for the various available crack paths.

For alumina/aluminum interfaces, cyclic fatigue cracks propagated exactly at the interface for the majority of cases tested (i.e., for all data in Fig. 5.1), in contrast to the results of fast fracture where all samples failed in the alumina. It can be inferred from the predictions of Ritchie *et al.* [54] that an interfacial crack path suggests that the fatigue crack growth resistance of the alumina/aluminum interface is lower than that of the aluminum layer and represents a weaker path for crack extension.

For 5 μm thick layer alumina/aluminum sandwich samples, however, the crack path switched into the alumina at higher driving forces as illustrated in Fig. 5.4 and did not

return to the interface. It can be concluded based on [54] that at these higher driving forces, the alumina represents the weakest path to allow for deviation off the interface onto a path less favored by modulus mismatch considerations. This conclusion is further supported by the data for bulk AD995 alumina, which crosses over the data for the interface samples and clearly demonstrates inferior fatigue crack growth resistance at higher driving forces (Fig. 5.4). It is surprising, however, that samples with thicker layers do not switch onto the apparently weaker alumina path and instead stay at the interface at high driving forces. This phenomenon can be rationalized, however, when the increased blunting and lower crack tip stresses associated with thicker layers as described in Chapter 4 for monotonic fracture are considered. It can be inferred that for samples with thicker layers, crack tip stresses are decreased due to blunting below the level necessary to initiate fatigue crack growth into the alumina. Conversely, for 5 μm thick layer samples the crack tips are sharper due to the increased plastic constraint, allowing high enough stresses for fatigue failure to deviate onto the weaker alumina crack path at higher driving forces.

Cracks in PTLP bonded samples also behaved differently under cyclic loading as compared to monotonic loading. While monotonic fracture occurred almost entirely at the alumina/niobium interface, cyclic fatigue failure occurred by a combination of interfacial failure and near interfacial failure in the neighboring alumina; in some samples cyclic fatigue failure occurred almost entirely in the alumina. Cracks that grew in the alumina were constantly drawn back to the interface, which was in contrast to the 5 μm thick alumina/aluminum samples described above, and resulted in a near interfacial crack path. For a crack in the alumina, crack deflection toward the interface is consistent with

the predicted high driving force path based on modulus mismatch [54]; however, crack deflection back into the alumina suggests that the interface has a higher intrinsic resistance to fatigue crack propagation compared to that of the alumina in regions where near interfacial (alumina) crack propagation is prevalent. While the effects of modulus mismatch draw the crack to the interface, the lower intrinsic fatigue crack propagation resistance of the alumina allows the crack to deviate again back into the ceramic.

Both the 5 μm thick alumina/aluminum and the PTLP bonded alumina/niobium joints exhibited crack deflection into the alumina under cyclic loading. One notable difference in behavior is that for the alumina/aluminum joints cracks did not return to the interface while for the PTLP bonded joints crack were constantly drawn back to the interface by modulus mismatch effects. Since both material systems have positive β and are expected to demonstrate crack deflection towards the interface, it is suspected that the difference in layer thickness (5 versus 125 μm) accounts for the difference in behavior. Investigations into near interfacial crack paths for sandwich specimens have determined that the modulus mismatch effects of the layer only extend over distances of approximately five times the layer thickness away from the interface [17]. This implies that for samples with 5 μm thick layers, the crack only needs to deviate ~ 25 μm into the alumina, or 1.4 times the average grain size, before the effects of the layer are no longer felt. This scenario is not difficult to achieve since the intergranular crack path in the alumina necessitates that crack deviations span at least one, often several, grain diameters into the alumina. In contrast, for the PTLP bonded samples, a crack would need to deviate ~ 625 μm, or 35 times the average grain size, to no longer be drawn back to the interface. Thus the

shorter range over which the modulus mismatch effects can be felt can account for cracks not returning to the interface for samples with 5 μm thick aluminum layers.

5.2.2. Cyclic fatigue mechanisms: Role of plastic constraint

For alumina/aluminum joints, evidence for the presence of fatigue striations on the aluminum side of the fracture surface was seen, similar to that observed by McNaney *et al.* [33]. Fatigue striation markings suggest a mechanism of fatigue crack propagation similar to that of ductile metals, with crack advance occurring by a process that involves blunting and re-sharpening of the crack tip, with individual striation markings corresponding to each blunting event. The amount of crack advance per cycle is directly related to the amount of blunting at the crack tip, with the cyclic growth increment typically scaling with some fraction of the crack tip opening displacement, i.e., ~ 0.1 to 0.3 for mode I self-similar growth in ductile metals [95]. Thus, if plastic constraint restricts the degree of blunting during each cycle, this should act to reduce the growth rate for thinner layers. While this gives rise to higher fatigue resistance in the more highly constrained samples, it is important to note that for layer thicknesses ≥ 100 μm, the computed plastic zone thickness, r_{py}, at the crack tip is small enough near the fatigue threshold (~ 35 μm at 4 J/m^2 [23,36]) so that it does not extend completely across the metal layer. In this range of layer thicknesses, no effect of layer thickness is to be expected; indeed, experiments by McNaney *et al.* [33] observed no layer thickness effects on cyclic fatigue thresholds in the range of 100 – 500 μm thick aluminum layers.

An additional complication arises for the alumina/aluminum samples with 5 μm aluminum layers, where crack jumping from interface to interface potentially leads to

bridging ligaments of aluminum in the crack wake (Fig. 5.3), which may have sustained some of the applied load, giving rise to an increase in the measured fatigue threshold [35]. However, a recent study of the fatigue behavior of 2 μm thick layers of 99.999% pure aluminum sandwiched between sapphire, wherein smaller flaws exist and no crack jumping was reported, described a fatigue threshold of ~ 10 J/m^2 [34]. This result is similar to results for the 5 μm thick aluminum layer samples and significantly higher than the threshold of 4 J/m^2 found for 100 μm thick layer samples in the present work, suggesting that effects on the fatigue threshold due to crack jumping are secondary to that of plastic constraint.

5.2.3. Cyclic fatigue mechanisms: Alumina fatigue

For the alumina/aluminum samples with 5 μm thick aluminum layers, the crack path deviated off the interface and into the alumina as driving forces were increased. Additionally, for some PTLP bonded samples cracks propagated almost entirely in the alumina for all driving forces. In both cases, the mechanism of fatigue crack advance is identical to that of bulk alumina, which is now described below. Many polycrystalline, grain bridging aluminas, including Coors AD995, have revealed a true cyclic fatigue effect, with degradation of grain bridges attributed as the mechanism for crack advance [90-94]. Under monotonic loading, when intergranular fracture is predominant in alumina, frictional tractions along the fractured grain boundaries in the crack wake sustain load and shield the crack tip from part of the applied driving force, resulting in rising toughness with crack extension as these bridges develop [85-87]. Evidence of this behavior can be seen in the rising R-curve shown in Fig. 4.5. As the crack is cycled open

and closed, however, the grain bridges that provide toughening in the alumina degrade by mechanisms such as abrasive wear, thereby promoting crack advance; individual increments of crack advance are thought to occur by the same mechanisms as in monotonically loaded fracture [90-94].

5.2.4. Cyclic fatigue mechanisms: Short crack effects

For 5 μm thick aluminum layer samples, after the crack leaves the interface and enters the alumina, crack growth occurs at higher growth rates than measured for bulk alumina for the first ~ 2 mm of growth and a V-shaped *da/dN* - ΔG curve (Fig. 5.4) is observed, similar to that found for short cracks in bulk alumina (Fig. 5.8). Since alumina demonstrates rising crack resistance with crack extension under monotonic loading (Fig. 4.5), it is not surprising to observe crack size effects under cyclic loading as well. Crack size effects under cyclic loading are typically referred to as short or small crack[2] effects, with short cracks invariably growing at rates faster than long cracks at the same applied driving force [96-98]. Specifically with grain bridging ceramics such as alumina, cracks may be considered to be short if the crack length is smaller than the distance over which extrinsic toughening (i.e., grain bridging) takes place behind the crack tip .

Short crack effects in AD995 alumina are demonstrated in Fig. 5.8 where faster growth rates are clearly observed for fatigue cracks that have extended less than 2 mm from the machined notch. Specifically, under decreasing ΔG conditions, short cracks (Δa_f < 2 mm) demonstrated a fatigue threshold 50 – 65% of that for corresponding long cracks (Δa_f > 2 mm). For increasing loading, a V-shaped curve is observed, with growth

rates initially decreasing with increasing applied loading before finally merging with the long crack data.

Such behavior can be rationalized when it is considered that the grain bridging zones for short cracks have not yet reached the steady state size found for long cracks. Accordingly, the amount of load that can sustained by the smaller grain bridging zone is necessarily less than that of corresponding long cracks that have full sized, steady state grain bridging zones. This situation leads to a higher effective, near tip driving force for small cracks as compared to long cracks. To calculate the effective near tip stress intensity range[3], ΔK_{eff}, in the presence of bridging, the bridging contribution, K_{br}, is subtracted from K_{max} using the principle of superposition:

$$\Delta K_{eff} = (K_{max} - K_{br}) - K_{min} . \qquad (5\text{-}2)$$

K_{br} is then the amount of stress intensity (driving force) no longer experienced at the crack tip due to load sustained by bridges, while K_{min} and K_{max} are determined by the loading for any given crack length. The result of bridging is then a reduction in maximum stress intensity experienced locally at the crack tip, leading to a reduction in ΔK_{eff} along with a decrease in the effective load ratio, R, shown schematically in Fig. 5.9. The value of K_{br} is less for short cracks than for long cracks, and thus ΔK_{eff} is greater for any given applied loading, resulting in the observed higher growth rates at the same applied driving force.

The bridging stress intensity, K_{br}, can be measured for bulk alumina by comparing the experimentally measured compliance of the bridged crack to the theoretical compliance

[2] Short or small fatigue cracks are defined as cracks small compared to: (i) the scale of microstructure, (ii) the extent of local inelasticity, or (iii) the extent of crack-tip shielding in the crack wake, where short cracks are small in one dimension and small cracks are small in all dimensions [96-98].

for a traction free crack of the same size [99], schematically illustrated in Fig. 5.9b. In the present study, bridging load measurements were made on bulk alumina samples by periodically stopping the long crack fatigue test and measuring the actual sample compliance along with optically measuring the actual crack length. The measured crack length was used to compute the theoretical compliance by using standard C(T) compliance calibrations, which was then compared with the measured compliance to obtain K_{br}. Accordingly, Fig. 5.10 shows long crack results plotted in terms of both the applied and effective driving force, along with short crack results.

We can see from Fig. 5.10 that when the long crack data are plotted in terms of the effective, near tip driving force, that a lower bound curve is obtained, below which short cracks do not propagate in bulk alumina. This reaffirms the assertion that the observed short crack behavior in alumina is due to the lack of an equilibrium grain bridging zone for short cracks; indeed, when the contribution of grain bridging is removed, long cracks no longer demonstrate slower fatigue crack growth rates as compared to short cracks.

For the case of 5 μm thick aluminum layer samples, while the interfacial cracks are physically long, alumina grain bridges can only begin to develop and sustain load after the cracks have entered the alumina. Thus short crack fatigue behavior is observed in these samples; indeed, the V-shaped da/dN - ΔG curve seen in Fig. 5.4 is similar to that observed for short cracks in bulk alumina (Fig. 5.8). As the crack grows into the alumina, although the applied driving force is increasing, crack tip shielding due to the grain bridges initially increases at a faster rate, causing the effective driving force at the crack tip to decrease; this leads to an initial reduction in crack growth rates. After further

[3] Here the stress intensity factor, K, is used because of its superposition properties. Once calculated, ΔK_{eff} can be converted to ΔG_{eff} using Eq. 2-1.

crack growth, however, a steady state is reached where grain bridges are created and degraded at an equal rate, and the growth rates match those of the large cracks in the bulk alumina. Additionally, long crack data for bulk alumina plotted in terms of the effective driving force (i.e., when the contribution of bridging is removed) provide a lower bound for the initial crack growth off the alumina/aluminum interface and into the alumina (Fig. 5.11). The results shown in Fig. 5.11 reaffirm that it is indeed the lack of a steady state grain bridging zone that accounts for the initially faster growth rates as cracks leave the interface and enter the alumina.

5.2.5. Cyclic fatigue mechanisms: Grain bridging zone lengths

Bridging zones associated with cyclic fatigue crack growth in the alumina were observed in the present study to be on the order of 2 mm based on the convergence point of the long and short crack data. Under monotonic loading, rising crack resistance is still observed after > 6 mm of crack growth (Fig. 4.5), which suggests an equilibrium bridging zone greater than 6 mm in length. Clearly this is much greater than the 2 mm zone observed in fatigue, which supports the notion that it is indeed the degradation of the bridging zone under cyclic loading that is responsible for fatigue crack growth in alumina ceramics. Additional experimental evidence of smaller equilibrium bridging zones under cyclic, as compared to monotonic, loading has been reported for alumina by Hu *et al.* [100].

A rough estimate of the bridging zone length under monotonic loading can be made by noting that effective grain bridging occurs only up to the point behind the crack tip where the crack opening displacement is approximately 1/4 to 1/3 of the average grain

size, d_g [101,102]. Using a simple hinge model for crack opening, the extent of the grain bridging zone can thus be estimated by calculating the point where the crack opening is approximately in this range. The opening displacement at the loadline, δ, can be calculated using:

$$\delta = \frac{P}{E'B} V\left(\frac{a}{W}\right) \tag{5-3}$$

where P is the applied load, B and W are the specimen thickness and width, respectively, and the function $V(a/W)$ is given by Saxena *et al*. [103]. While for an unbridged, linear elastic crack the axis of rotation is typically taken to be $0.2(W-a)$ ahead of the crack tip [104], experimental observations of alumina specimens [102] suggest that grain bridging interactions across the crack faces draw the axis of rotation very near the crack tip. Thus, taking the hinge of rotation to be at the crack tip, and assuming a linear crack opening profile from the crack tip to the loadline, the rule of similar triangles can be used to determine the point where the crack opening is approximately $d_g/4$ - $d_g/3$. Using this method a grain bridging zone extending some 8 to 11 mm behind the crack tip under monotonic loading is predicted for the present Coors AD995 alumina. While this value is not inconsistent with the results for monotonic loading shown in Fig. 4.5, it is clearly greater than the 2 mm bridging zone experimentally observed in fatigue. Using this model, the measured bridging zone length of ~ 2 mm for cyclic loading implies that effective grain bridges exist behind the crack tip up to the point where the maximum crack opening is on the order of $d_g/16$, which may be a useful parameter for future predictions of bridging zone lengths under cyclic loading in grain bridging alumina ceramics.

5.2.6. Cyclic fatigue mechanisms: Additional effects of extrinsic toughening

For PTLP bonded samples, interfacial cyclic fatigue crack growth appeared to occur by relatively brittle separation of the niobium/alumina interface with accompanying ductile failure of the copper regions. No fatigue markings or deformation of any kind were observed on the metal side of the fatigue fracture surface, which is in contrast to the results for the alumina/aluminum samples. Possible explanations for this difference may involve such factors as the higher yield strength for the present niobium relative to aluminum and/or lower W_{at} allowing interface separation without observable blunting. As mentioned previously, microhardness measurements indicate that the yield strength of the niobium may be greater than 500 MPa, or an order of magnitude higher than that expected for the aluminum. Additionally, a low W_{at} for the alumina/niobium interface due to the presence of adsorbed copper may cause the driving force necessary for interfacial separation to be low enough such that observable fatigue markings were not created.

Evidence of deformed copper adhering to both sides of the fatigue fracture surface suggests that a ductile fatigue mechanism most likely occurs in these regions. This implies an interfacial fatigue mechanism involving a process of separation of the niobium/alumina interface accompanied by ductile fatigue of the copper regions. Again this appears to be analogous to a ductile phase reinforced brittle matrix composite, where some resistance to fatigue crack propagation derives from the extrinsic toughening created by the ductile reinforcing phase that bridges the crack wake and fails in fatigue [82,105]. Although ductile phase reinforcement has proven to be less effective under cyclic loading as compared to monotonic loading, it has been demonstrated that fatigue

crack growth resistance can be imparted into brittle materials by the addition of a ductile second phase [82,105].

Sample-to-sample variation in the measured fatigue crack growth rates corresponds with the variation in interfacial versus near interfacial (alumina) crack path for each sample (Fig. 5.5). As mentioned previously, based on linear elastic crack path predictions [54], the intrinsic fatigue crack growth resistance at the interface is expected to range locally from comparable to slightly higher than that of the alumina to allow both crack propagation paths to be active. In order to explain the higher global crack growth resistance that is measured for predominantly near interfacial (alumina) fatigue crack growth (Fig. 5.5), extrinsic toughening mechanisms in the alumina (i.e., grain bridging) must be taken into account. Samples with only ~ 50% of the crack wake in the alumina experience less grain bridging and correspondingly higher near tip driving forces compared to samples with closer to 100% alumina crack path. This results in decreased measured fatigue crack growth resistance in the presence of interfacial fatigue failure even though the local intrinsic resistance at the interface is thought to range from comparable to somewhat higher than that of the alumina.

Supporting evidence for this notion can be found if one compares the fatigue data for the PTLP bonded joints to that of the bulk alumina with the contributions of extrinsic toughening (i.e., grain bridging) removed. In Fig. 5.12 it is seen that when the contribution of bridging is removed, the data for the bulk alumina fall very near the lower bound for the PTLP bonded samples. These results demonstrate that the intrinsic fatigue resistance of the alumina (i.e., in the absence of grain bridging) is indeed comparable to that of the PTLP bonded interface, as was expected based on the observations of the

crack path discussed previously. Additionally, it is seen that reduced grain bridging can indeed account for the scatter in the fatigue data for the PTLP bonded joints, as well as the correspondence of crack growth resistance to the percentage of alumina grain pullout on the fatigue fracture surface.

5.2.7. Reliability of joints

In comparing alumina/aluminum joints with different layer thicknesses, sandwich samples with 5 μm thick aluminum layers have demonstrated a higher fatigue threshold as compared to samples with thicker layers tested in both in the present study and in others [33]. It should be noted, however, that samples with thicker layers continue to demonstrate ductile fatigue behavior as driving forces are increased (Fig. 5.1), while in contrast, samples with 5 μm thick layers show a change in mechanism to brittle fatigue in the alumina that is in fact detrimental to the overall fatigue resistance (Fig. 5.4). It can therefore be concluded that alumina/aluminum sandwich joints with 100 μm and thicker aluminum layers demonstrate superior fatigue crack growth resistance properties compared to samples with 5 μm thick aluminum layers.

As for comparing the fatigue resistance of the alumina/aluminum joints to that of bulk alumina, it can be seen that for samples with ≥ 100 μm thick aluminum layers, although the fatigue threshold for interfacial crack growth is lower than bulk alumina, the ductile fatigue behavior at higher driving forces, along with the corresponding lower power law exponents, allow for appreciable fatigue life and reasonable fatigue lifetime prediction (Fig. 5.4). Such ductile fatigue behavior is typically considered superior to brittle fatigue behavior (e.g., alumina) when applying a damage tolerant approach to fatigue lifetime in

design. Samples with 5 μm thick aluminum layers, however, provide the worst of both worlds, demonstrating lower fatigue thresholds than both short and long cracks bulk alumina along with brittle fatigue behavior at high driving forces. Additional short crack effects for crack propagation into the alumina make the fatigue properties for samples with 5 μm thick layers even less desirable.

For PTLP bonded alumina/niobium sandwich samples, fatigue crack growth thresholds for interfacial and near interfacial cracking have been found to range from ~ 20 – 30 J/m^2, with data for bulk alumina at the upper end of that range (~ 30 J/m^2). As discussed above, the threshold of ~ 30 J/m^2 for the bulk alumina can only be achieved after > 2 mm of crack extension, after which a steady state grain bridging zone behind the crack tip is achieved. For cracks shorter than 2 mm in length, bulk alumina exhibits significantly less fatigue crack growth resistance (Figs. 5.8 & 5.12) in the form of lower fatigue thresholds and faster crack growth rates at comparable driving forces. This implies that the bulk alumina only possesses consistently superior fatigue crack growth resistance when cracks are greater than 2 mm in length, and as in fast fracture the presence of such long cracks in many cases would most likely be detrimental to the overall mechanical properties of the structure. Thus, based on the results of the present work, the presence of the PTLP joints does not appear to be detrimental to the overall fatigue crack growth resistance of the joined structure for cases when flaws are of reasonably practical sizes (< 2 mm).

5.3. Conclusions

Based on an experimental study of the interfacial/near interfacial fatigue crack growth resistance of liquid state bonded alumina/aluminum sandwich joints and partial transient liquid phase bonded joints consisting of alumina bonded with copper/niobium/copper interlayers, the following conclusions may be made:

1. For alumina/aluminum joints the interfacial fatigue crack growth resistance was found to decrease with increasing aluminum layer thickness at near threshold driving forces; this was observed in the form of lower fatigue thresholds and higher growth rates in the near threshold regime.
2. Stable cyclic fatigue crack growth occurred predominantly at the alumina/aluminum interface, with the only exception being samples with 5 μm thick layers at high driving forces.
3. Trends of decreasing fatigue threshold with increasing layer thickness were attributed to changes in plastic constraint. For the 100 μm thick layer samples, estimates of the plastic zone size suggest that plasticity does not extend through the thickness of the layer at the fatigue threshold; for the 5 and 35 μm thick layer samples, conversely, the plasticity is constrained by the thickness of the layer, thereby limiting the degree of crack blunting and consequently the crack advance per cycle even at threshold.
4. At higher driving forces, the trajectory of the cyclic fatigue cracks was found to change for 5 μm thick layer samples, specifically from an interfacial path to crack growth in the alumina, resulting in substantially less crack growth resistance. Additionally, short crack effects, attributed to lack of grain bridging for a crack just

entering the alumina, caused the initial cracking to occur at lower driving forces than normally measured for large cracks in bulk alumina.

5. Cyclic bridging zones were measured in the alumina to be ~ 2 mm in length, significantly smaller than expected under monotonic loading due to grain bridge degradation under cyclic loading conditions. Such cyclic bridging zone lengths corresponded to a distance behind the crack tip where the maximum crack opening was ~ $d_g/16$.
6. For PTLP bonded samples, cyclic fatigue crack trajectories were either near interfacial in the alumina, or a combination of interfacial (~ 0 – 50 %) and near interfacial (~ 50 – 100 %). In the predominantly near interfacial (alumina) case, the rates of fatigue crack growth corresponded closely to those for long cracks in bulk alumina at the same driving force, while in the mixed interfacial/near interfacial case, crack growth behavior in the joints showed somewhat lower crack growth resistance in the form of higher fatigue crack growth rates and lower fatigue thresholds.
7. In regions where interfacial fatigue was prominent, crack growth occurred by separation of the niobium/alumina interface along with apparent ductile failure of the copper regions. Conversely, near interfacial (alumina) fatigue occurred by grain bridging degradation in the alumina
8. Scatter in the fatigue behavior are attributed to the role of extrinsic toughening mechanisms (i.e., grain bridging) in the alumina. A higher proportion of the crack path within the alumina results in increased crack tip shielding via grain bridging, resulting in lower near tip driving forces and increased fatigue resistance.

9. By comparing the fatigue properties of the bonded joints to that of bulk alumina, it is concluded that the presence of PTLP bonded joints does not appear to be detrimental to the fatigue resistance of the bonded ceramic structure in the cases where flaws sizes are in a reasonable regime for brittle materials (< 2 mm). In contrast, for alumina/aluminum joints, the presence of 5 μm thick aluminum layers is detrimental to the overall fatigue resistance; however, 100 μm and thicker layers demonstrate more desirable ductile fatigue properties.

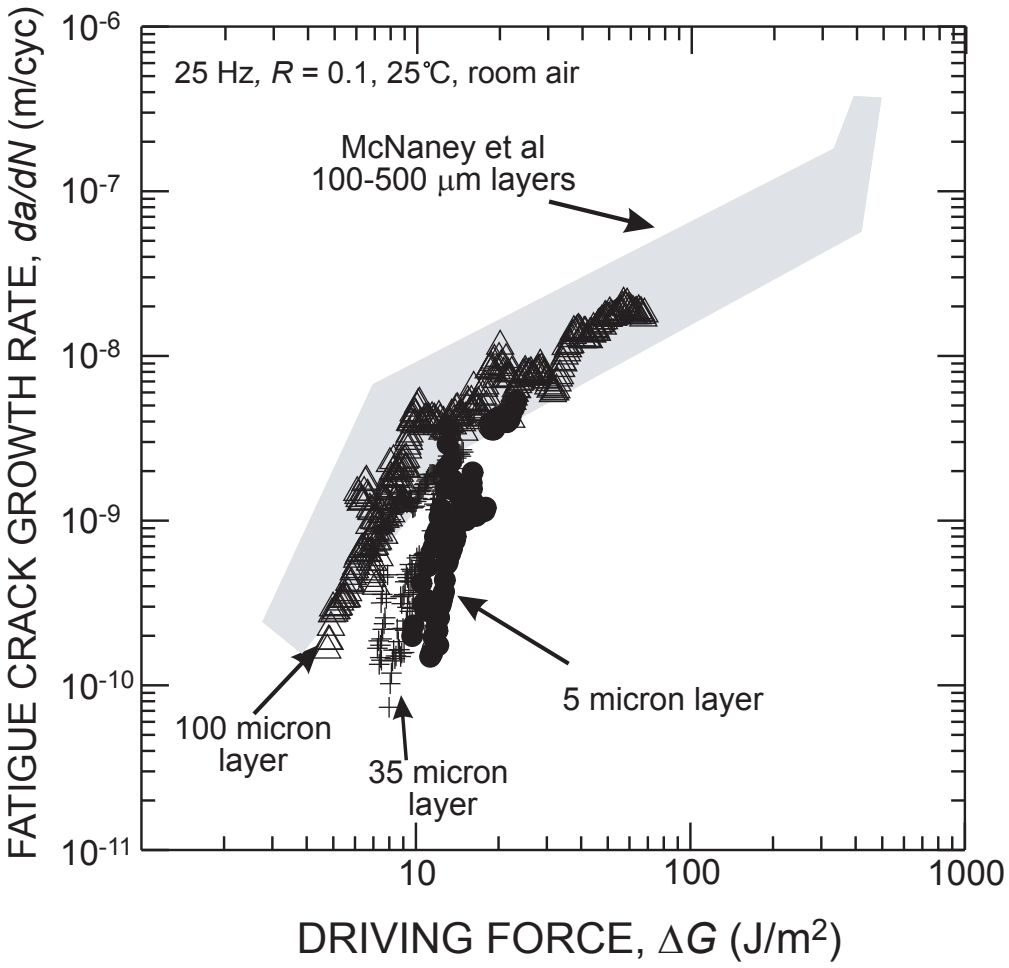

Figure 5.1. Fatigue crack growth results showing a decrease in crack growth rates with decreasing layer thickness in the near threshold regime. Additional data from McNaney *et al.* [33].

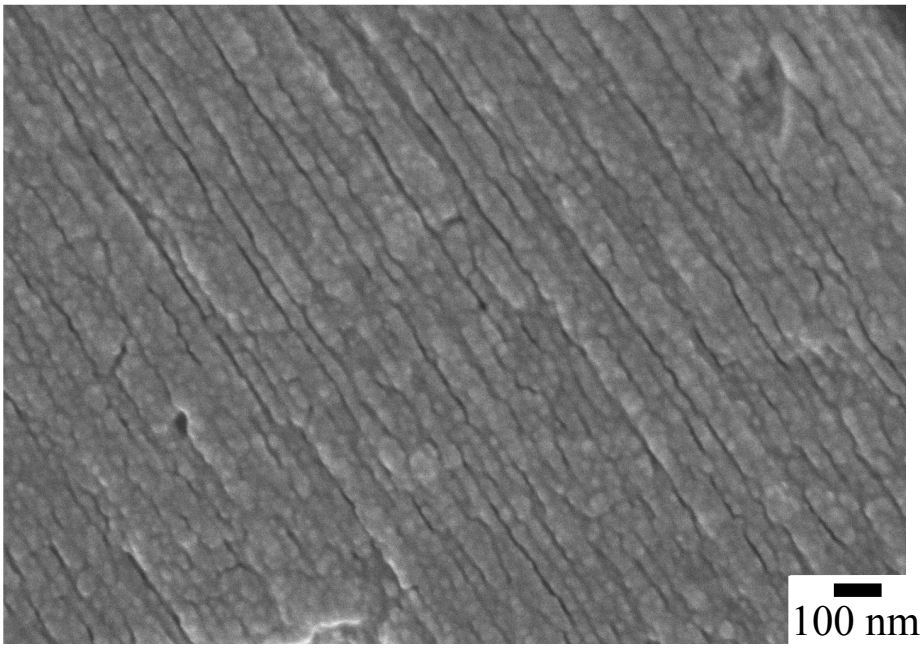

Figure 5.2. Micrograph showing evidence of fatigue striations on the aluminum side of the fatigue fracture surface due to fatigue crack growth at an applied ΔG of ~ 10 J/m^2. Direction of crack growth was left to right with respect to the micrograph.

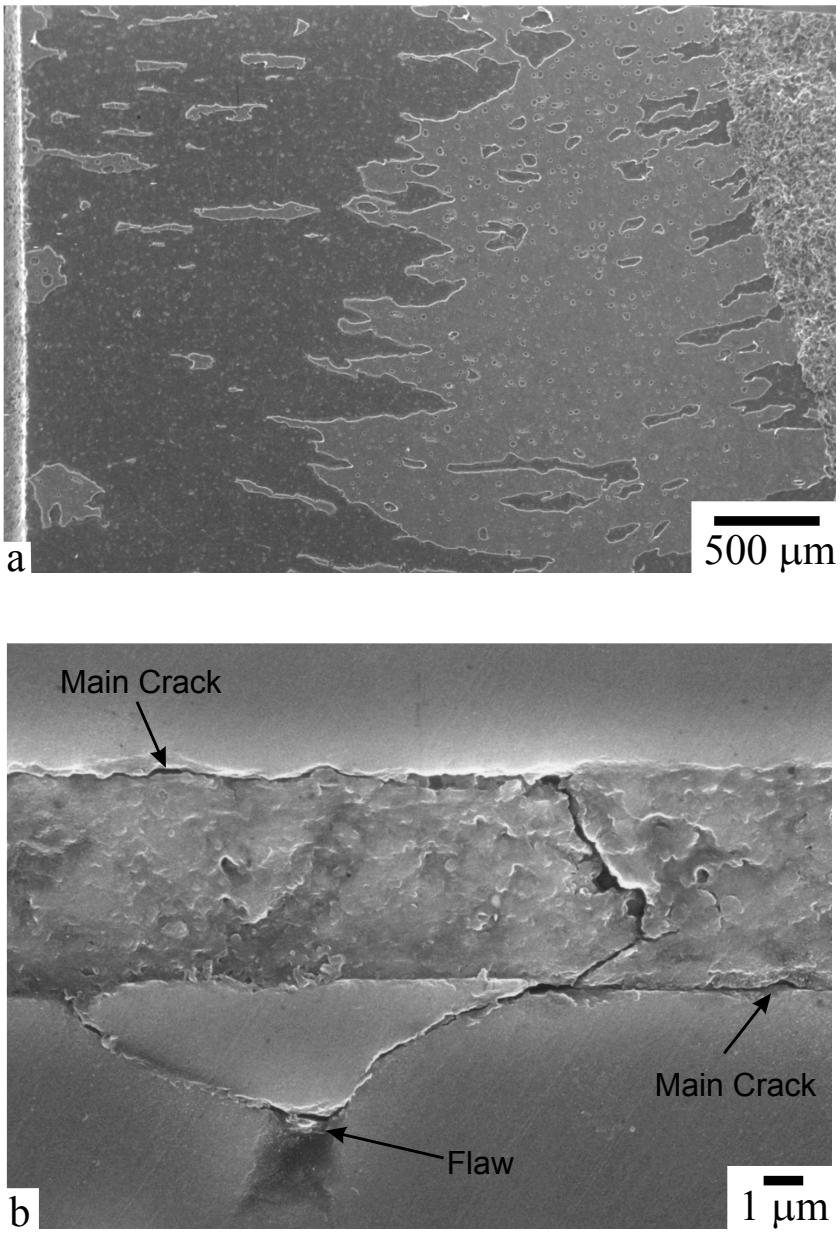

Figure 5.3. Evidence of crack jumping both (a) on the fatigue fracture surface and (b) in profile on a 5 μm thick layer sample. In (a) aluminum is seen in lighter contrast. In (b) crack jumping is observed to initiate at a flaw in the alumina. Fatigue crack growth occurred at applied ΔG values in the range of ~ 10 - 15 J/m^2. Direction of crack growth was left to right with respect to the micrograph.

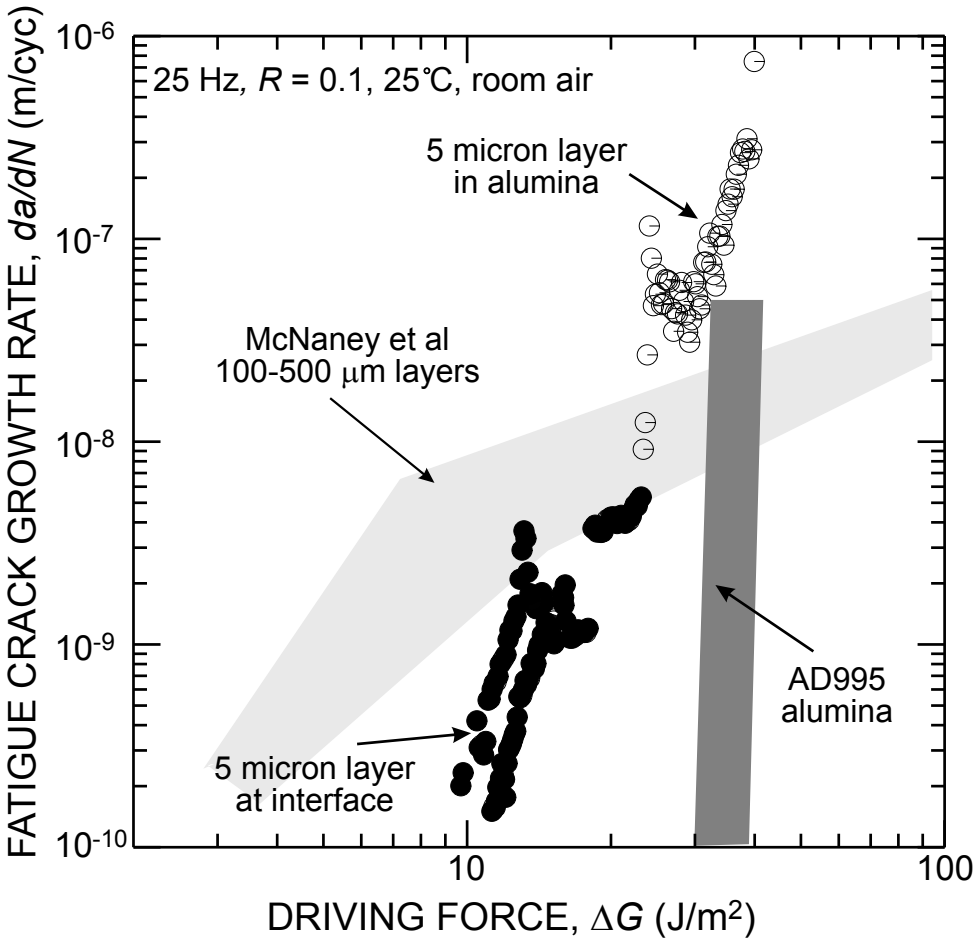

Figure 5.4. Fatigue crack growth results for a fatigue crack leaving the interface of a 5 μm thick aluminum layer sample and growing in the alumina. Growth rates were initially faster than that of bulk alumina, with the data merging only after > 2 mm of crack growth.

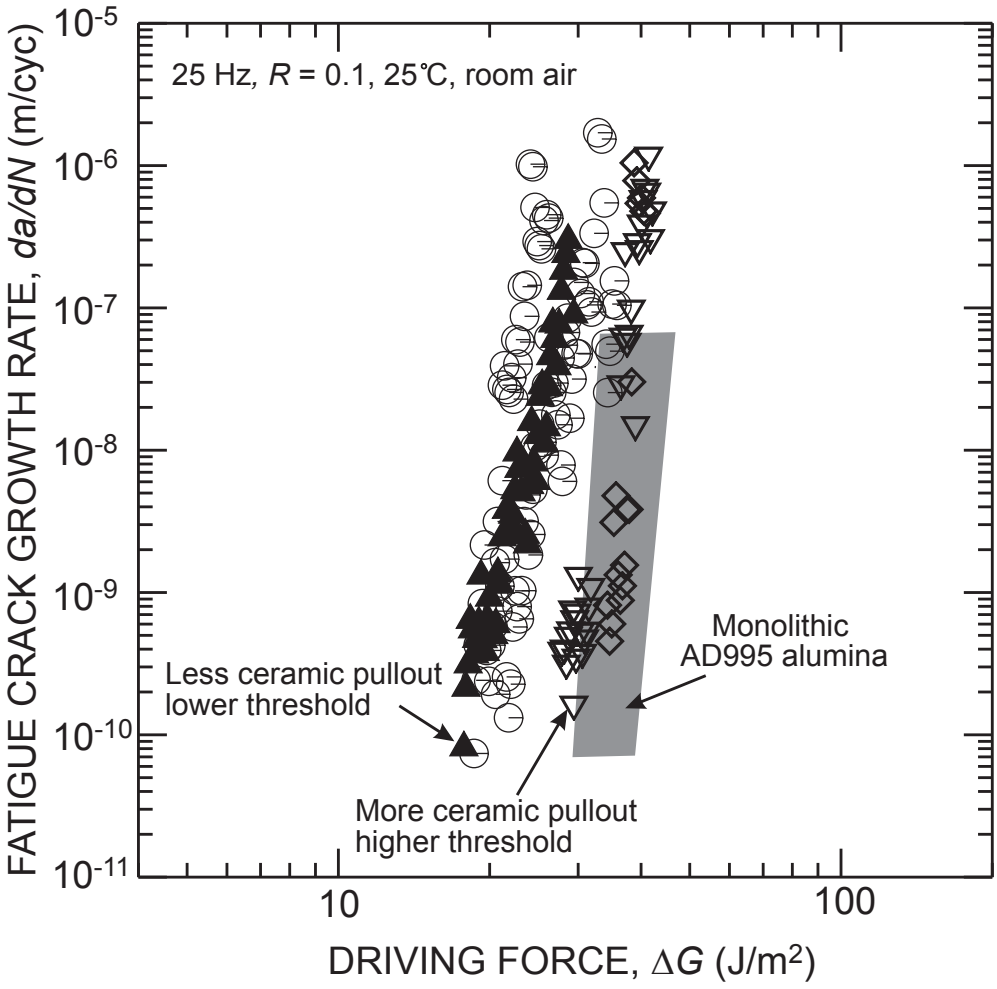

Figure 5.5. Fatigue crack growth rates for PTLP bonded sandwich specimens. Individual symbols correspond to different individual samples. Higher fatigue thresholds were measured for samples with more alumina grain pullout during fatigue crack growth.

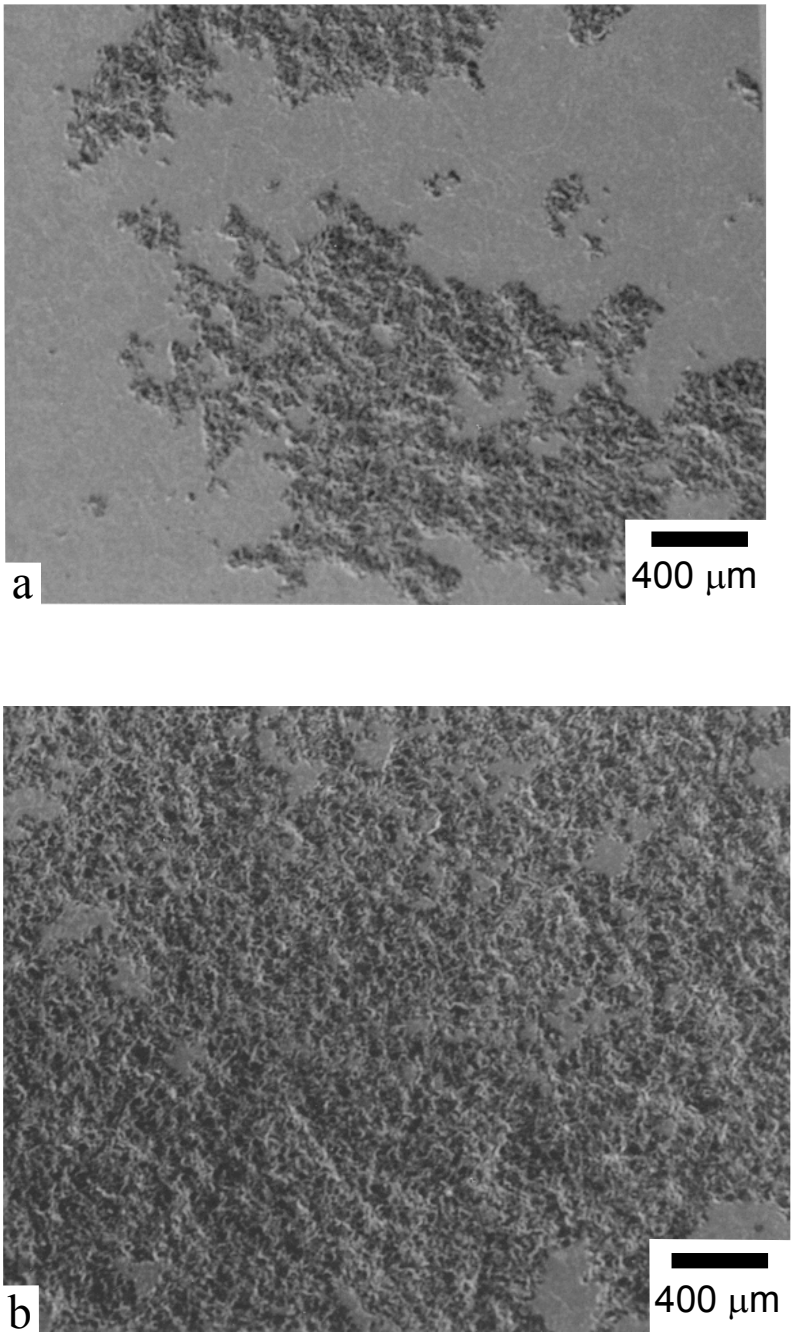

Figure 5.6. Micrographs of fatigue fracture surfaces showing (a) ~ 50% and (b) ~ 100% alumina grain pullout. For the latter case fatigue crack propagation was almost entirely in the alumina. Fatigue crack growth occurred at applied ΔG values ranging from 19 - 36 J/m^2 in (a) and 28 - 42 J/m^2 in (b), reflecting the observed differences in fatigue crack resitance for each case. Direction of crack propagation was left to right with respect to the micrographs.

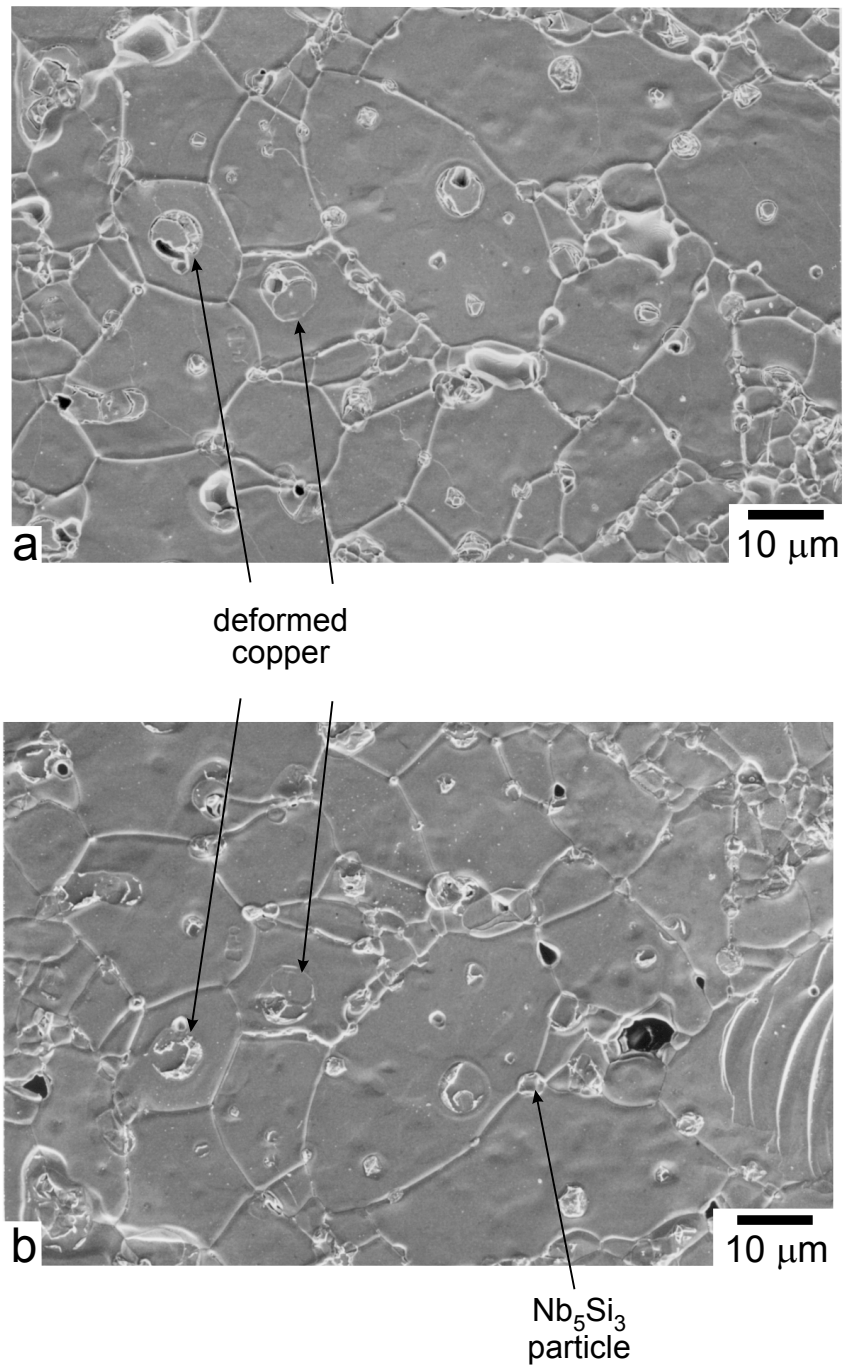

Figure 5.7. Matching micrographs of the same region of the (a) niobium and (b) alumina side of the fatigue fracture surfaces for the sample shown in Fig. 5.6a. Deformed copper regions appear flattened with some separation of the alumina/copper interface visible. Matching imprints of the alumina grain boundaries can be seen in the niobium. Direction of crack propagation was left to right with respect to the micrograph.

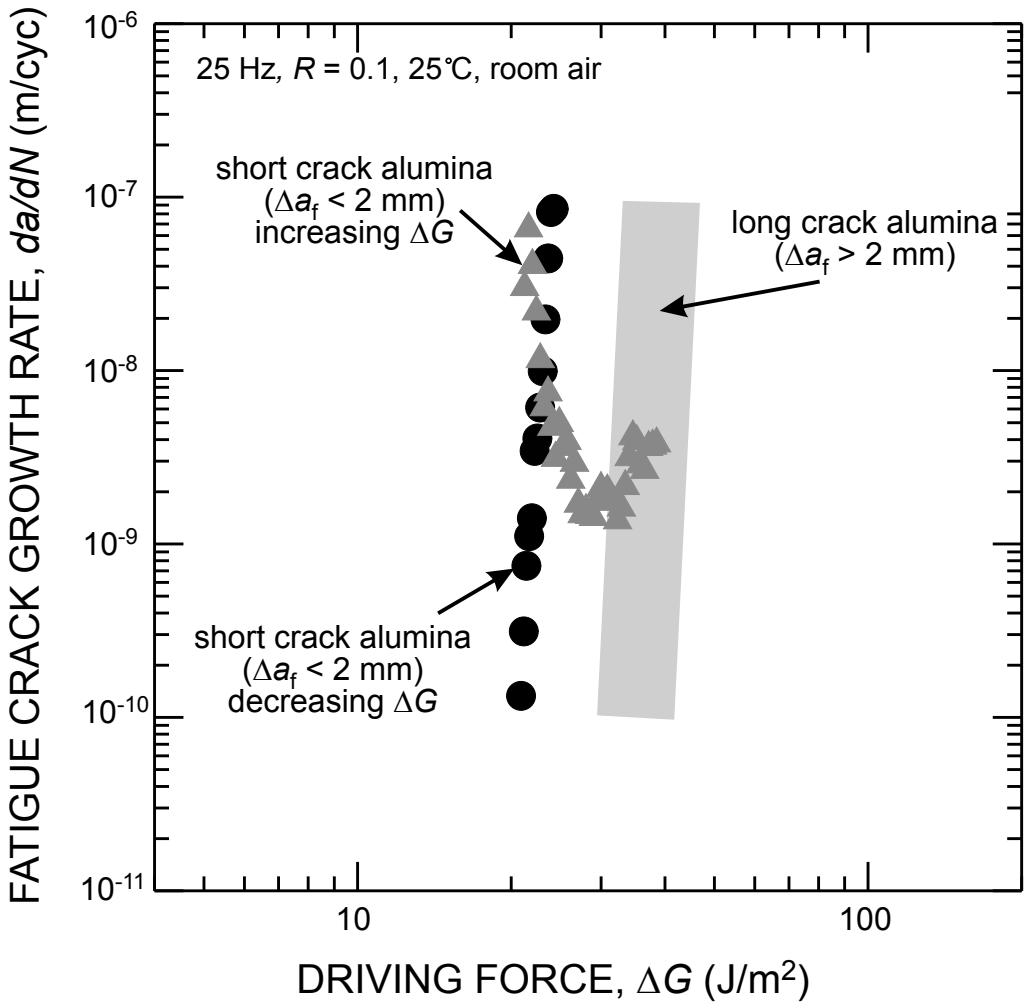

Figure 5.8. Short crack fatigue results for Coors AD995 alumina. Under decreasing ΔG conditions a lower fatigue threshold is measured compared to long cracks, while for increasing ΔG conditions a V-shaped curve is observed with data merging after ~ 2 mm of crack growth..

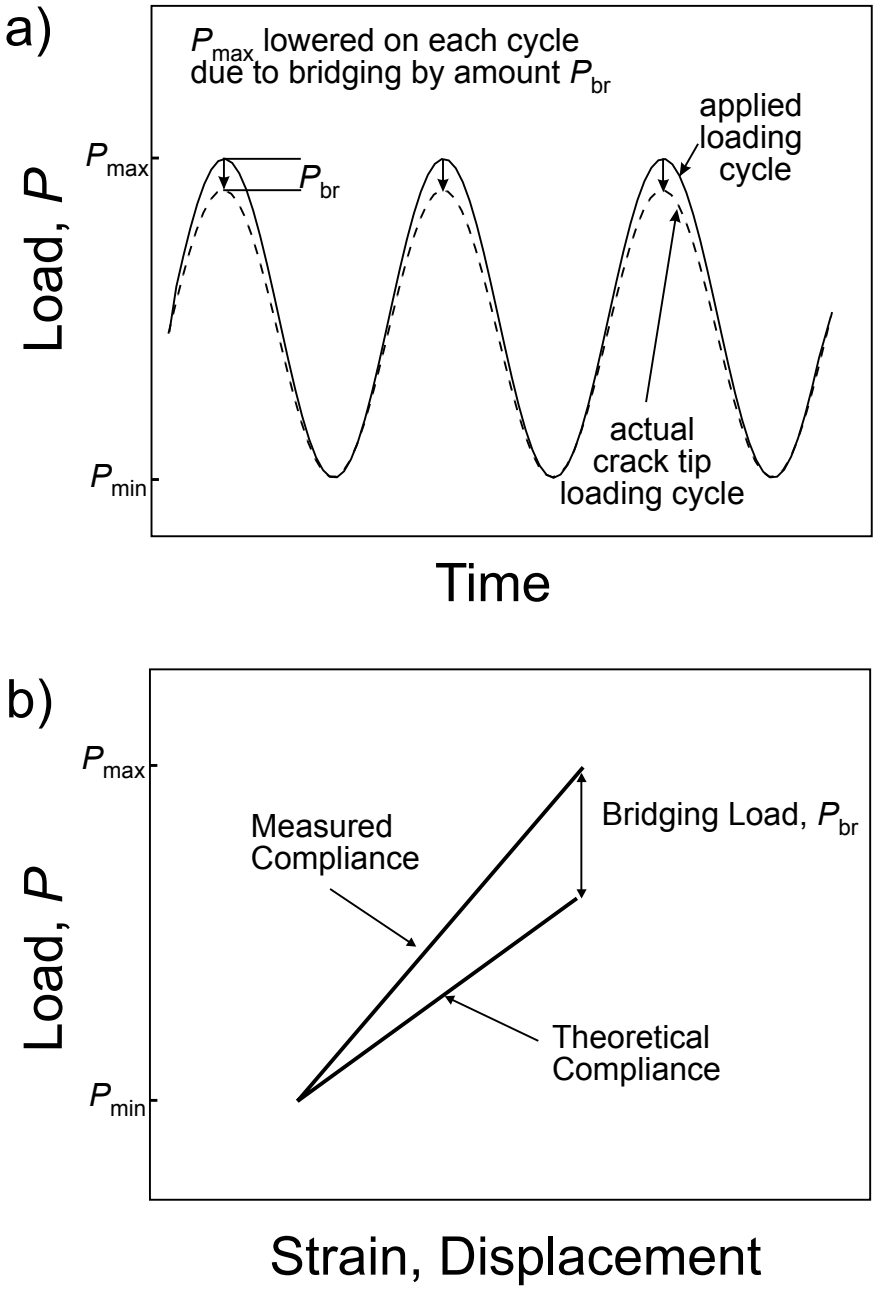

Figure 5.9. Schematics showing a) how the near tip loading cycle is affected by bridging and b) how measurements are made for the bridging load, P_{br}, using the measured and calculated compliance curves. P_{br} is used to calculate the corresponding bridging stress intensity, K_{br}.

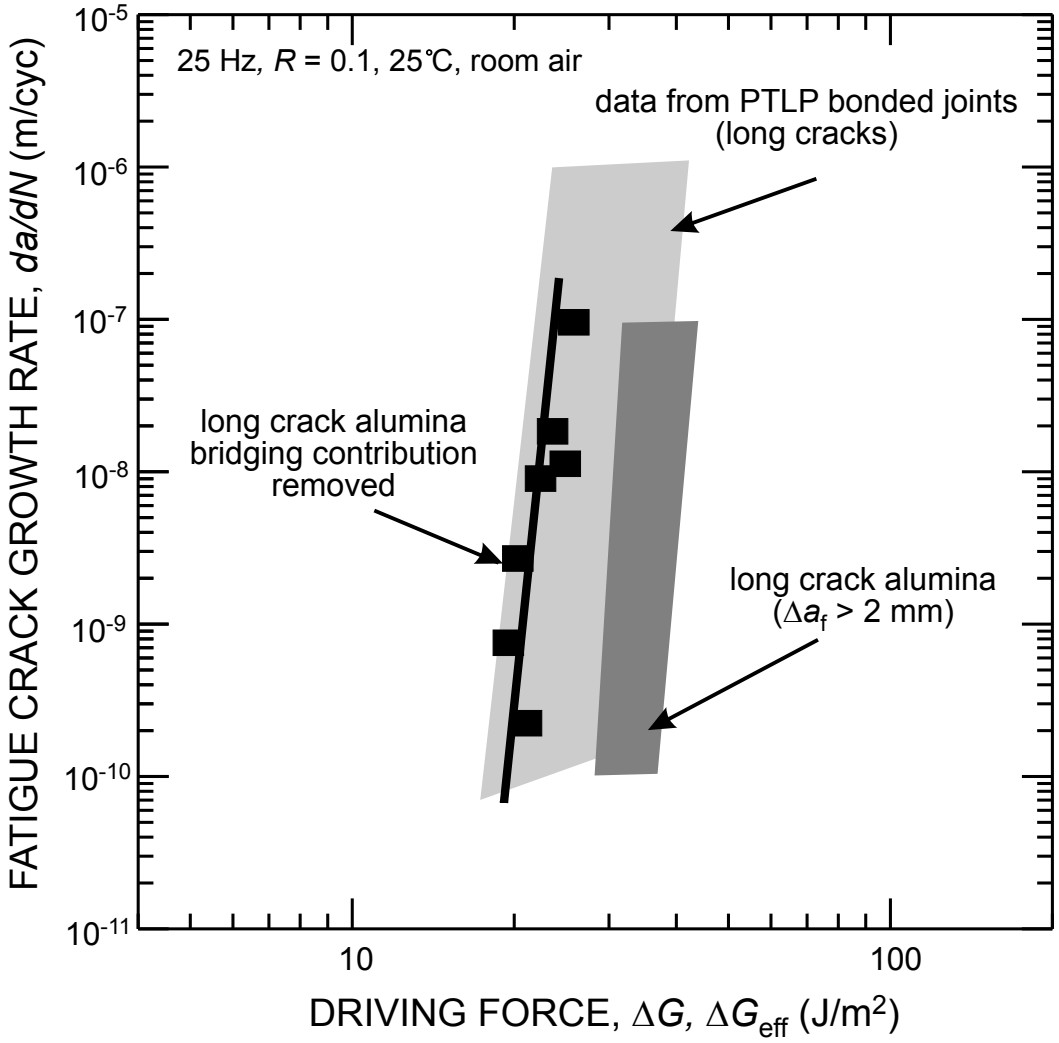

Figure 5.12. Bridging adjusted long crack alumina fatigue data plotted along with data for PTLP bonded samples. Note that differing amounts of grain bridging can account for much of the scatter in the PTLP bonded sample data. Indeed, when the contribution of bridging is removed the alumina data falls near the lower bound of the PTLP bonded data.

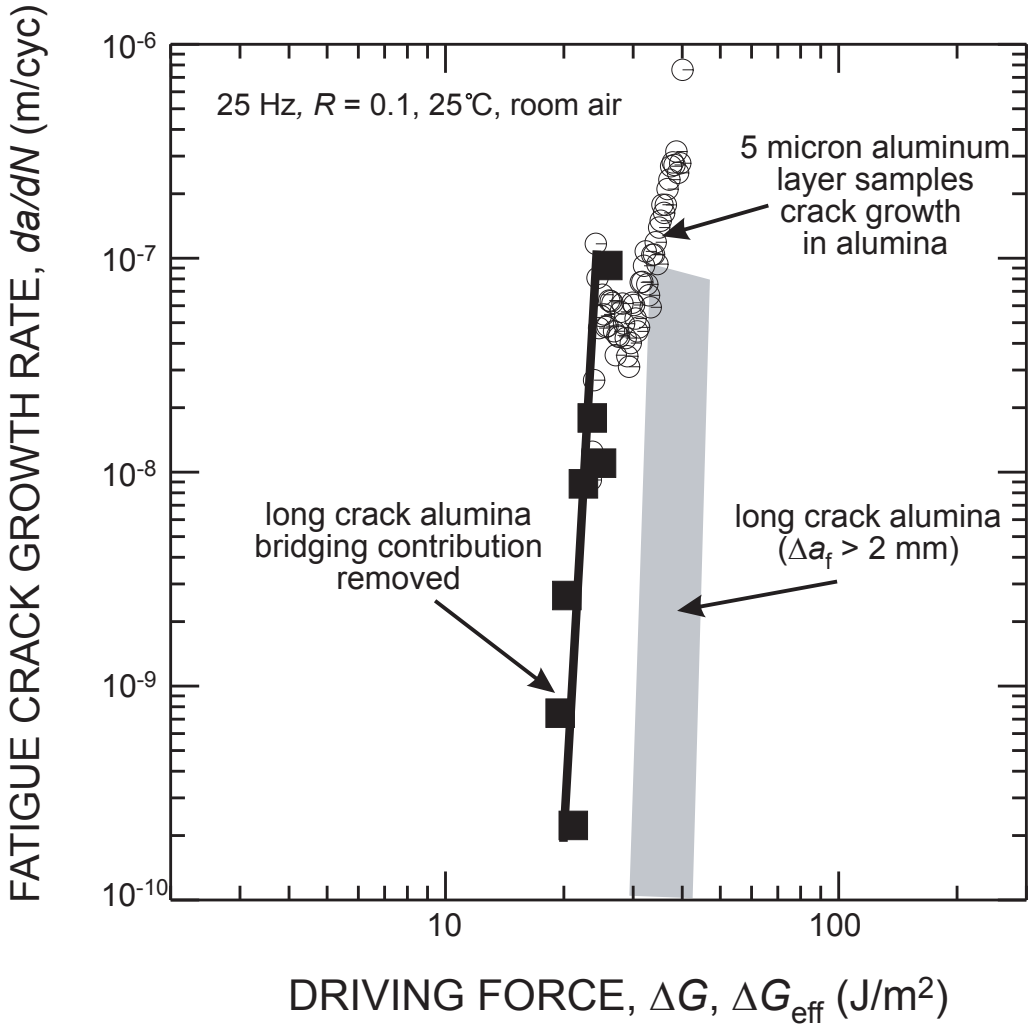

Figure 5.11. Data for near interfacial fatigue crack propagation in the alumina for samples with 5 μm thick aluminum layers plotted along with the bridging adjusted long crack alumina data. Note that when the effects of bridging are removed, the adjusted long crack alumina data provide a lower bound for the initial crack growth off the interface.

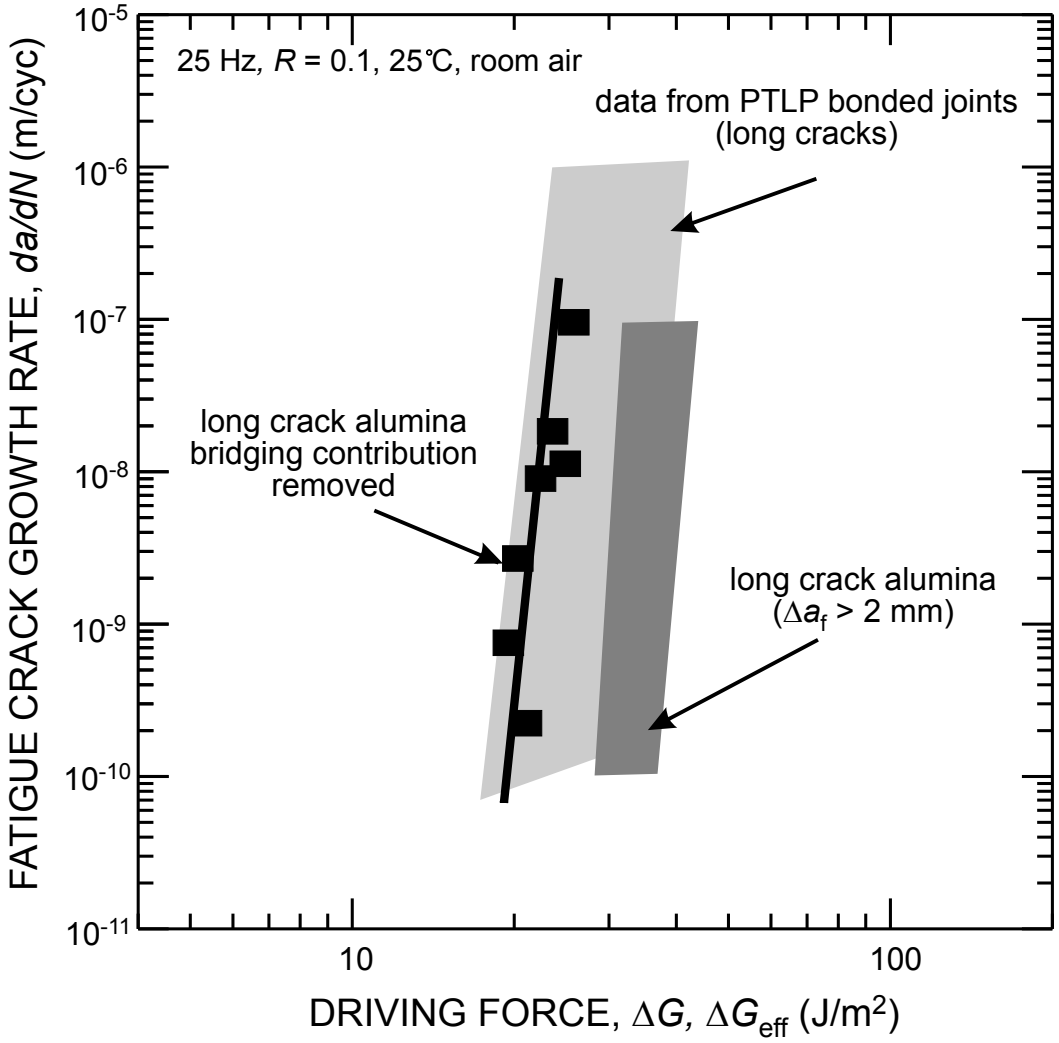

Figure 5.12. Bridging adjusted long crack alumina fatigue data plotted along with data for PTLP bonded samples. Note that differing amounts of grain bridging can account for much of the scatter in the PTLP bonded sample data. Indeed, when the contribution of bridging is removed the alumina data falls near the lower bound of the PTLP bonded data.

CHAPTER 6
MOISTURE ASSISTED SLOW CRACK GROWTH

6.1. Results

For interfacial cracks in alumina/aluminum/alumina sandwich samples under static loading in a moist environment (> 95 % relative humidity), separation along the alumina/aluminum interface was not observed in any of the samples tested. Crack growth did occur, however, in samples with thinner aluminum layers when interfacial fatigue pre-cracks left the interface and propagated into the alumina. As shown in Fig. 6.1, initial crack growth in the alumina for the 5 μm thick layer samples occurred at driving forces lower than necessary for equivalent growth in pre-cracked bulk alumina samples. For samples with 35 μm thick aluminum layers, analogous crack growth occurred in two of three samples, but only at driving forces higher than necessary for crack growth in bulk alumina. Due to the high driving forces necessary to initiate growth into the alumina in these samples, once the crack had grown a short distance from the plastically deforming aluminum layer, catastrophic fracture occurred, limiting the amount of subcritical crack growth data that could be obtained. It should be noted that this was a true time dependent effect, with failure occurring only after several hours at constant load. Indeed, limited stable crack growth was actually measured before final failure, as shown in Fig. 6.1. In the case of samples with 100 μm thick layers (and one sample with a 35 μm thick layer), no subcritical crack growth was observed at measurable rates ($\geq 10^{-9}$ m/sec) up to driving forces of ~ 200 J/m^2.

Fig. 6.2 shows direct evidence that moisture assisted crack growth did not occur at the interface, with fatigue markings evident up to the point where the crack deviated into the alumina. Based on observations of the fracture surface, moisture assisted crack growth appeared to occur along an intergranular crack path in the alumina.

6.2. Discussion

Under moisture assisted crack growth conditions, crack propagation only occurred by crack deviation off of the alumina/aluminum interface and into the alumina. Similar to fast fracture, this observed crack path implies that the alumina represents the weakest path for crack advance based on the results of Ritchie *et al.* [54]. While samples with 5 μm thick aluminum layers exhibited stable moisture assisted crack growth in the alumina, samples with 100 μm thick layers demonstrated high resistance to such growth, with no crack growth observed up to driving forces of 200 J/m^2, or well above the fracture toughness of the alumina. Samples with 35 μm thick layers exhibited a range of behavior and generally intermediate resistance to moisture assisted crack growth. As reasoned for the toughness results, the higher resistance to moisture assisted crack propagation for samples with thicker aluminum layers is attributed to increased crack tip plasticity and blunting that lowers the local crack tip stresses relative to values necessary for the crack to leave the interface and enter the alumina. At 22 J/m^2, where growth was first measured for 5 μm thick layer samples, the normalized mean hydrostatic stress, σ_m/σ_o, is greater than 7, while a sample with a 100 μm thick layer would need to be loaded to > 300 J/m^2 to experience similar stress levels ahead of the crack [27]. At such high load levels, only catastrophic fast fracture of the alumina is possible, and stable moisture

assisted crack growth may not occur except possibly to aid in the initiation of cracking for fast fracture.

In some cases samples with 35 μm thick aluminum layers exhibited limited measurable stable crack growth even at loadings that exceeded the fracture toughness of alumina. Such behavior may be rationalized by considering the toughening effects of the ductile aluminum layer for near interfacial cracks. Although near interfacial cracks may not blunt into the aluminum layer like interfacial cracks, plastic deformation of the layer may still occur when cracks are very near the interface. Plastic energy dissipation in the aluminum layer can accordingly raise the apparent toughness by shielding the crack from some of the applied driving force. Similar behavior has been observed for fracture in multi-layered interconnect structures from the semiconductor industry [106]. As the crack propagates away from the plastically deforming layer; however, the toughening benefits of the layer decay until critical fracture occurs, as was observed.

Additionally, for one 35 μm thick layer samples cracking did not occur off the interface into the alumina at driving forces up to 200 J/m^2. One possible cause for this scatter in the observed behavior may be due to differences in the local flaw populations in the alumina near the crack tip. Since crack propagation into the alumina from a plastically blunted interfacial crack tip is dependent upon activating near tip flaws in the alumina, random variations in flaw populations can accounts for scatter in the observed behavior. Specifically, it is likely that there were no near tip flaws large enough to initiate failure into the alumina for the 35 μm thick layer sample where moisture assisted time dependant failure did not occur.

The observed crack growth for the alumina/aluminum interface specimens was primarily intergranular in the alumina, and appeared to be identical to that observed in previous studies on moisture assisted crack growth in bulk alumina [60,107]. Initial moisture assisted crack growth in the 5 μm thick layer samples occurred at driving forces lower than for crack growth in fatigue pre-cracked bulk alumina samples. It should be noted, however, that the curve shown for the bulk alumina is not unique, and only represents data from the initial growth from large (Δa_f > 2 mm) fatigue pre-cracks. Subsequent measurements of crack velocity (*v*-*G*) curves result in a shift of the data to higher driving forces, as illustrated in Fig. 6.3. Two *v*-*G* curves, measured in succession on the same sample at ~ 40% relative humidity, are shown in Fig. 6.3, where each measured curve is successively shifted to higher driving forces. This effect has been observed previously in alumina by Steinbrech *et al*. [108], with the shifting of the *v*-*G* data attributed to the systematic progression up the R-curve. Indeed, if the contribution of crack shielding (i.e., grain bridging) could be accounted for, a *v*-*G* curve for the traction free crack could be considered unique or intrinsic to the material [109].

The marked shift of the *v*-*G* data to lower driving forces for the 5 μm thick layer samples indicates that there was a lower initial starting point on the alumina R-curve than for the fatigue pre-cracked bulk alumina samples, where initial pre-crack lengths were several millimeters in length. Indeed, initial crack growth for the 5 μm layer samples occurred at a driving force of 22 J/m^2, which is very near the extrapolated initiation toughness of ~ 20 J/m^2 taken from the R-curve shown in Fig. 4.5, where the fatigue pre-crack was only 230 μm in length. The low driving force necessary for initial growth into the alumina for the 5 μm thick layer samples implies an initial position near the

beginning, or lowest point, of the alumina R-curve. As was found in cyclic fatigue, the results indicate a crack size effect for globally large interface cracks that only begin to develop grain bridging, and subsequent R-curve toughening, after they deviate off the interface and into the alumina.

6.3. Conclusions

1. Under static loads in a moist environment, cracks in samples with 5 μm thick aluminum layers left the interface and propagated subcritically in the alumina; this did not occur in samples with 100 μm thick metal layers due to enhanced crack tip blunting in the aluminum.
2. Samples with 35 μm thick layers exhibited generally intermediate resistance to moisture assisted crack growth with some scatter in the observed behavior. Plastic deformation in the nearby aluminum layer allowed limited stable moisture assisted crack growth in the alumina prior to catastrophic failure at driving forces greater than the toughness of the alumina.
3. Initial crack growth into the alumina for 5 μm thick layer samples occurred at driving forces lower than that measured for crack growth from large fatigue pre-cracks in bulk alumina. Such behavior was rationalized in terms of the decreased contribution from grain bridging for interfacial cracks just entering the alumina.

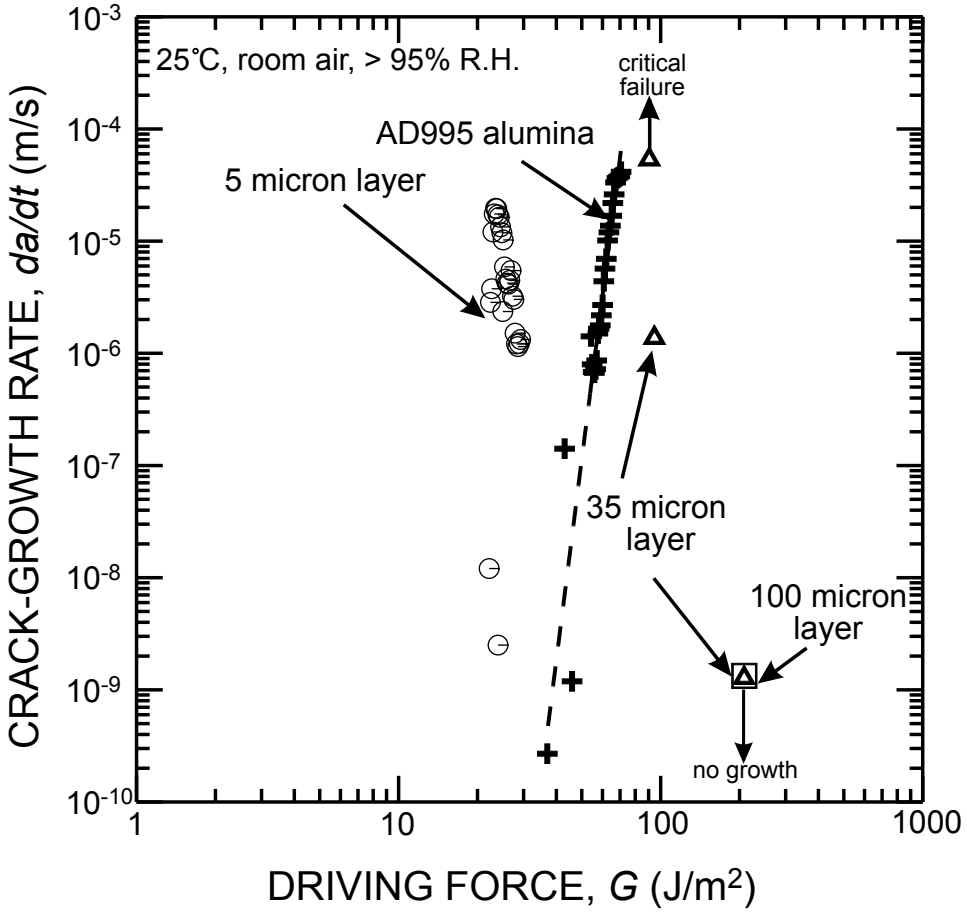

Figure 6.1. Moisture-assisted crack growth results for alumina/aluminum sandwich and bulk alumina specimens in > 95% relative humidity room air. Crack growth was in the alumina for all cases where growth occurred.

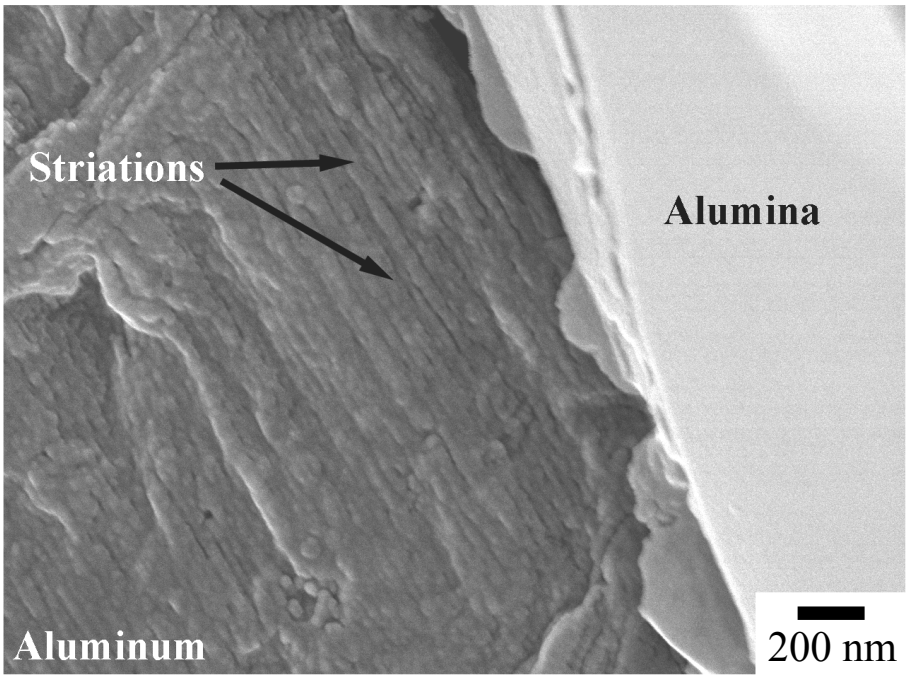

Figure 6.2. Evidence of fatigue striations up to the point where the crack left the interface during moisture-assisted crack growth. Direction of crack propagation was left to right.

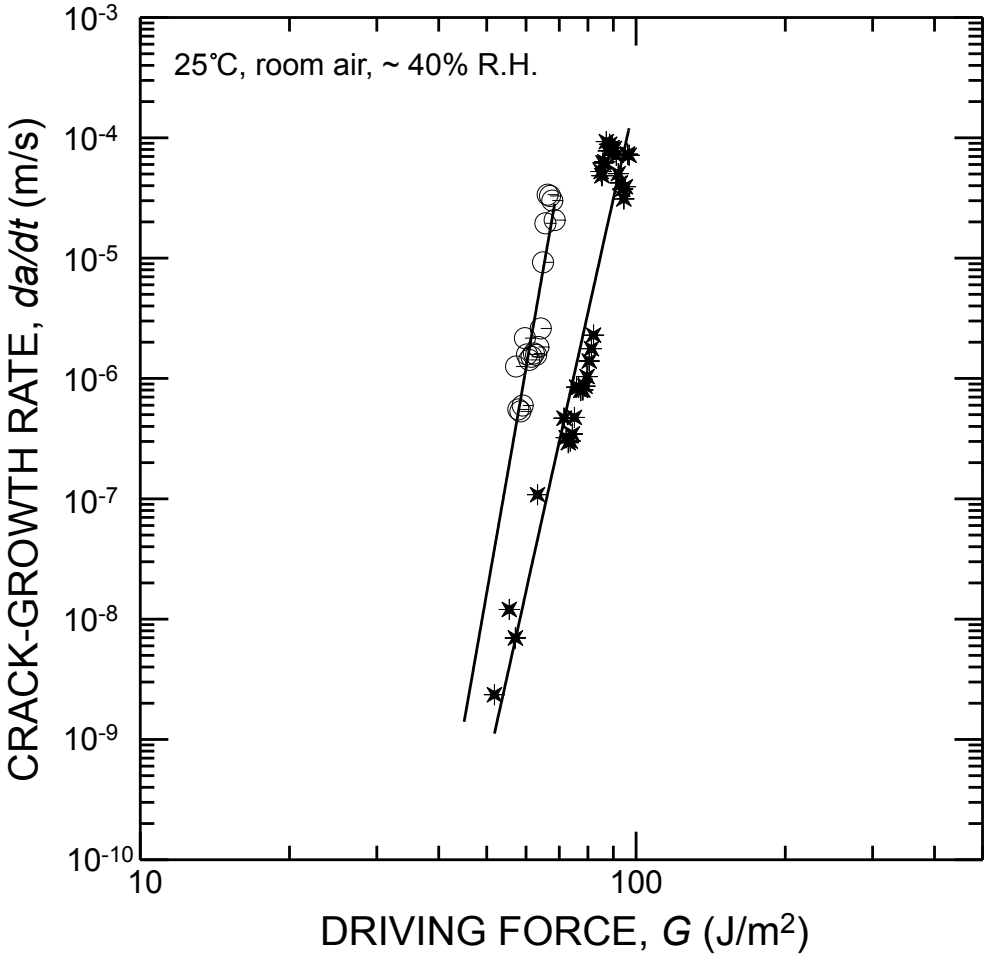

Figure 6.3. Two sequentially measured *v*-*G* curves for a fatigue pre-cracked bulk alumina sample measured in 40% relative humidity room air. The curve measured second is shifted to higher driving forces, corresponding to a higher starting point on the alumina R-curve.

CHAPTER 7
FINAL REMARKS AND FUTURE WORK

7.1. Alumina/aluminum system

Experiments conducted using sandwich specimens consisting of 99.999% pure aluminum layers bonded between 99.5% pure polycrystalline alumina substrates while varying the aluminum layer thickness from 5 to 100 μm focused on investigating the role of changing metal layer thickness, and the resultant changing plastic constraint, during failure. Although it was found that the unnotched 3-point bending strength of the aluminum bonded joints increased with decreasing layer thickness, in general the fracture toughness, cyclic fatigue resistance, and moisture assisted crack growth resistance were all found to be degraded at thinner layer thicknesses due to the higher degree of plastic constraint. Specifically:

- Mean fracture energies decreased from 367 to 55 J/m^2 as the aluminum layer thickness was reduced from 100 to 5 μm.
- Although cyclic fatigue thresholds were somewhat higher for thinner layers, the transition to brittle fatigue in the alumina at higher driving forces resulted in lower overall fatigue resistance.
- A mechanism for moisture assisted crack growth was activated for thinner layers whereby interfacial cracks deviated into and propagated in the alumina.

Thus it has been determined that increasing the plastic constraint in the aluminum layer by decreasing layer thickness results in an overall reduction in the flaw tolerance of the alumina/aluminum sandwich joint.

Crack deviation off the alumina/aluminum interface and into the alumina was observed for each of these cases, however, leaving outstanding questions regarding the interfacial failure properties for this system. Future investigations into the role of plastic constraint on alumina/aluminum interfacial failure may consider the use of single crystal alumina (sapphire), where fewer flaws exist to allow crack deviation into the ceramic, thus possibly suppressing crack kinking behavior and promoting interfacial failure. Specific issues that may be addressed include:

- *Fracture toughness*: Since fracture occurred in the ceramic, the measured fracture toughness values were only lower bounds for the actual interface toughnesses. While the presently observed trends provide useful insight, the use of sapphire instead of polycrystalline alumina may prevent ceramic failure, allowing toughness measurements to be made for the actual alumina/aluminum interface as a function of layer thickness. Additionally, fracture experiments where the aluminum yield strength is increased via alloying additions for a constant layer thickness may also be considered. In this case, reduced crack tip blunting, and correspondingly reduced fracture toughness, would be expected, resulting in a similar effect to that achieved by increasing the degree of plastic constraint via thinner layers in the present study.
- *Cyclic loading:* As mentioned previously, crack jumping from interface to interface was prevalent for samples with 5 μm thick aluminum layers and was observed to initiate at flaws in the alumina. The significantly lower flaw population of sapphire may limit such jumping behavior as seen in [34], allowing for the effects of changing plastic constraint to be isolated from the issues of crack bridging/shielding that were discussed above. Additionally, in order to investigate the degree to which fatigue

crack growth rates may be retarded in the near threshold regime by increasing the level of constraint via thinner (h < 5 μm) layers, crack deviation into the alumina must be prevented. In the limit of very thin aluminum layers (i.e., as $h \rightarrow 0$), it is conceivable that interfacial fatigue crack growth may be suppressed almost completely due a lack of plasticity and blunting in the layer due to high constraint; sapphire would be ideal for such experiments since it has high resistance to mechanical fatigue effects which would make fatigue crack deviation into the ceramic unlikely.

- *Moisture assisted crack growth:* Although no *interfacial* moisture assisted crack growth was observed in the present study, the question remains whether the alumina/aluminum interface is nonetheless susceptible to moisture assisted crack growth under conditions of further reduced crack blunting and reduced propensity for cracking into the alumina. While the first condition may be met by further decreasing the aluminum layer thickness and/or increasing the aluminum yield strength, the latter condition may be achieved by decreasing the flaw population at the interface by using sapphire instead of polycrystalline alumina.

7.2. The PTLP bonded system

Fracture experiments conducted on samples of alumina PTLP bonded with copper/niobium/copper interlayers revealed that room temperature interfacial fracture toughness values (~ 39 J/m^2) comparable to those for conventional diffusion bonded alumina/niobium samples (9-90 J/m^2) could be achieved via this novel processing route which offers the advantages of lower processing temperatures and/or pressures.

Additionally, the interfacial fracture and fatigue resistance was found to be comparable to that of the bulk alumina, and thus the presence of such joints is not considered to be detrimental to the overall flaw tolerance of the bonded ceramic structure. While these results are encouraging, roughly half of the apparent toughness appears to come from crack bridging by the ductile interfacial copper and the actual intrinsic alumina/niobium interface toughness is estimated only to be $\leq$ 20 J/m^2. It is speculated that this low interfacial toughness may be attributed to the high yield strength of the niobium for the present PTLP bonded joints which is caused by impurity pickup during processing and/or a low work of attraction, W_{at}, due to copper adsorption at the interface. Accordingly, future work may focus on using more simple, conventionally diffusion bonded alumina/niobium samples where the bonding conditions are carefully controlled to 1) further explore the interrelation of bulk niobium impurity concentration, yield strength, and interfacial toughness, and 2) investigate the role of interfacial copper adsorption by carefully controlling the amount of copper at bonded interfaces and determining the corresponding changes in interfacial fracture toughness and work of attraction.

REFERENCES

1. B.J. Dalgleish, M.C. Lu, and A.G. Evans, *Acta Metall.*, 1988, **36**(8), p. 2029-2035.
2. B.J. Dalgleish, K.P. Trumble, and A.G. Evans, *Acta Metall.*, 1989, **37**(7), p. 1923-1931.
3. B.J. Dalgleish, E. Saiz, A.P. Tomsia, R.M. Cannon, and R.O. Ritchie, *Scripta Metall. Mater.*, 1994, **31**(8), p. 1109-1114.
4. G. Elssner, T. Suga, and M. Turwitt, *J. De Physique*, 1985, **46**, p. C4-597 - C4-612.
5. A.G. Evans, M. Rühle, and M. Turwitt, *J. De Physique*, 1985, **46**, p. C4-613 - C4-626.
6. A.G. Evans and M.C. Lu, *Acta Metall.*, 1986, **34**(8), p. 1643-1655.
7. A.G. Evans, B.J. Dalgleish, M. He, and J.W. Hutchinson, *Acta Metall.*, 1989, **37**(12), p. 3249-3254.
8. A.G. Evans and B.J. Dalgleish, *Acta Metall. Mater.*, 1992, **40**, p. S295-S306.
9. F. Gaudette, S. Suresh, A.G. Evans, G. Dehm, and M. Rühle, *Acta Mater.*, 1997, **45**(9), p. 3505-3513.
10. M. De Graef, B.J. Dalgleish, M.R. Turner, and A.G. Evans, *Acta Metall. Mater.*, 1992, **40**(Suppl.), p. S333-S344.
11. M.Y. He, A.G. Evans, and J.W. Hutchinson, *Acta Mater.*, 1996, **44**(7), p. 2963-2971.
12. J.W. Hutchinson and Z. Suo, *Adv. App. Mech.*, 1992, **29**, p. 63-191.
13. D. Korn, G. Elssner, H.F. Fischmeister, and M. Rühle, *Acta Metall. Mater.*, 1992, **40**, p. S355-S360.
14. D. Korn, G. Elssner, R. Cannon, and M. Rühle, 2001, unpublished work.
15. S.X. Mao and M.Z. Li, *J. Mech. Phys. Solids*, 1999, **47**, p. 2351-2379.
16. S.X. Mao and A.G. Evans, *Acta Mater.*, 1997, **45**(10), p. 4263-4270.
17. J.M. McNaney, R.M. Cannon, and R.O. Ritchie, *Int. J. Fract.*, 1994, **66**, p. 227-240.
18. N.P. O'Dowd, M.G. Stout, and C.F. Shih, *Phil. Mag. A*, 1992, **66**(6), p. 1037-1064.
19. I.E. Reimanis, B.J. Dalgleish, M. Brahy, M. Rühle, and A.G. Evans, *Acta Metall. Mater.*, 1990, **38**(12), p. 2645-2652.
20. I.E. Reimanis, B.J. Dalgleish, and A.G. Evans, *Acta Metall. Mater.*, 1991, **39**(12), p. 3133-3141.
21. I.E. Reimanis, *Scripta Metall. Mater.*, 1992, **27**, p. 1729-1734.
22. J.R. Rice, *J. App. Mech.*, 1988, **55**, p. 98-103.
23. C.F. Shih and R.J. Asaro, *J. App. Mech.*, 1988, **55**, p. 299-316.
24. J.S. Stölken, Ph.D. thesis, University of California, Santa Barbara, 1997.
25. Z. Suo and J.W. Hutchinson, *Mater. Sci. Eng.*, 1989, **A107**, p. 135-143.
26. M.R. Turner and A.G. Evans, *Acta Mater.*, 1996, **44**(3), p. 863-871.
27. A.G. Varias, Z. Suo, and C.F. Shih, *J. Mech. Phys. Solids*, 1991, **39**(7), p. 963-986.
28. W.E. King, G.H. Campbell, D.L. Haupt, J.H. Kinney, R.A. Riddle, and W.L. Wien, *Scripta Metall. Mater.*, 1995, **33**(12), p. 1941-1946.

29. D.M. Lipkin, D.R. Clarke, and A.G. Evans, *Acta Mater.*, 1998, **46**(13), p. 4835-4850.
30. F.G. Gaudette, S. Suresh, and A.G. Evans, *Metall. Mater. Trans.*, 2000, **31A**, p. 1977-1983.
31. I.E. Reimanis, B.J. Dalgleish, and K.P. Trumble. in *Structural Ceramics Joning II*, eds. A.J. Moorhead, R.E. Loehman, and S.M. Johnson. American Ceramic Society, Weservile, Ohio, 1993, p. 219-228.
32. M.C. Shaw, D.B. Marshall, B.J. Dalgleish, M.S. Dadkhah, M.Y. He, and A.G. Evans, *Acta Metall. Mater.*, 1994, **42**(12), p. 4091-4099.
33. J.M. McNaney, R.M. Cannon, and R.O. Ritchie, *Acta Mater.*, 1996, **44**(12), p. 4713-4728.
34. F. Gaudette, S. Suresh, and A.G. Evans, *Metall. Mater. Trans.*, 1999, **30A**, p. 763-769.
35. R.M. Cannon, B.J. Dalgleish, R.H. Dauskardt, T.S. Oh, and R.O. Ritchie, *Acta Metall. Mater.*, 1991, **39**(9), p. 2145-2156.
36. C.F. Shih and R.J. Asaro, *J. App. Mech.*, 1989, **56**, p. 763-779.
37. T.S. Oh, R.M. Cannon, and R.O. Ritchie, *J. Am. Ceram. Soc.*, 1987, **70**(12), p. C-352 - C-355.
38. J.C. Card, R.M. Cannon, R.H. Dauskardt, and R.O. Ritchie. in *Joining and Adhesion of Advanced Inorganic Materials*, eds. A.H. Carim, D.S. Schartz, R.S. Silberglitt, and R.E. Loehman. Materials Research Society, 1993, p. 109-116.
39. T.S. Oh, R.M. Cannon, J. Rödel, A.M. Glaeser, and R.O. Ritchie. in *Interfaces in Polymer, Ceramic, and Metal Matrix Composites*, ed. H. Ishida. Elsevier, Amsterdam, 1988, p. 567-581.
40. M.L. Williams, *Bull. Seis. Soc. Amer.*, 1959, **49**(2), p. 199-204.
41. F. Erdogan, *J. App. Mech.*, 1965, **32**, p. 403-410.
42. A.H. England, *J. App. Mech.*, 1965, **32**, p. 400-402.
43. J.R. Rice and G.C. Sih, *J. App. Mech.*, 1965, **32**, p. 418-423.
44. G.C. Sih and J.R. Rice, *J. App. Mech.*, 1964, **31**, p. 477-482.
45. J. Dunders, *J. App. Mech.*, 1969, **36**, p. 650-652.
46. T.L. Becker, J.M. McNaney, R.M. Cannon, and R.O. Ritchie, *Mech. Mater.*, 1997, **25**, p. 291-308.
47. J.W. Hutchinson, M.E. Mear, and J.R. Rice, *J. App. Mech.*, 1987, **54**, p. 828-832.
48. R.V. Gol'dstein and R.L. Salganik, *Int. J. Fract.*, 1974, **10**(4), p. 507-523.
49. F. Erdogan and G.C. Sih, *J. Basic Eng.*, 1963, **85**(4), p. 519-527.
50. B. Cotterell, *Int. J. Fract. Mech.*, 1965, **1**(2), p. 96-103.
51. B.A. Bilby and G.E. Cardew, *Int. J. Fract.*, 1975, **11**(4), p. 708-712.
52. B. Cotterell and J.R. Rice, *Int. J. Fract.*, 1980, **16**(2), p. 155-169.
53. M.Y. He and J.W. Hutchinson, *J. App. Mech.*, 1989, **56**(2), p. 270-278.
54. R.O. Ritchie, R.M. Cannon, B.J. Dalgleish, R.H. Dauskardt, and J.M. McNaney, *Mater. Sci. Eng.*, 1993, **A166**, p. 221-235.
55. L. Shaw, D. Miracle, and R. Abbaschian, *Acta Metall. Mater.*, 1995, **43**(12), p. 4267-4279.
56. M. Turwitt, G. Elssner, and G. Petzow, *J. De Physique*, 1985, **46**, p. C4-123 - C4-127.

57. G. Elssner, D. Korn, and M. Rühle, *Scripta Metall. Mater.*, 1994, **31**(8), p. 1037-1042.
58. G. Kiessler, D. Korn, and G. Elssner, *Pract. Metall.*, 1992, **29**(12), p. 597-610.
59. M.F. Ashby, F.J. Blunt, and M. Bannister, *Acta Metall.*, 1989, **37**(7), p. 1847-1857.
60. A.G. Evans, *J. Mater. Sci.*, 1972, **7**, p. 1137-1146.
61. S.M. Wiederhorn, *Int. J. Fract. Mech.*, 1968, **4**(2), p. 171-177.
62. B.J. Dalgleish, A.P. Tomsia, K. Nakashima, M.R. Locatelli, and A.M. Glaeser, *Scripta Metall. Mater.*, 1994, **31**(8), p. 1043-1048.
63. B.J. Dalgleish, K. Nakashima, M.R. Locatelli, A.P. Tomsia, and A.M. Glaeser, *Ceram. Inter.*, 1997, **23**(4), p. 313-322.
64. Y. Iino, *J. Mater. Sci. Lett.*, 1991, **10**(2), p. 104-106.
65. M.R. Locatelli, A.P. Tomsia, K. Nakashima, B.J. Dalgleish, and A.M. Glaeser, *Key Eng. Mater.*, 1995, **111-112**, p. 157-190.
66. R.A. Marks, D.R. Chapman, D.T. Danielson, and A.M. Glaeser, *Acta Mater.*, 2000, **48**(18-19), p. 4425-4438.
67. R.A. Marks, J.D. Sugar, and A.M. Glaeser, *J. Mater. Sci.*, 2001, in press.
68. M. Paulasto, G. Ceccone, and S.D. Peteves, *Scripta Mater.*, 1997, **36**(10), p. 1167-1173.
69. S.D. Peteves, M. Paulasto, G. Ceccone, and V. Stamos, *Acta Mater.*, 1998, **46**(7), p. 2407-2414.
70. M.L. Shalz, B.J. Dalgleish, A.P. Tomsia, and A.M. Glaeser, *J. Mater. Sci.*, 1993, **28**(6), p. 1673-1684.
71. M.L. Shalz, B.J. Dalgleish, A.P. Tomsia, R.M. Cannon, and A.M. Glaeser, *J. Mater. Sci.*, 1994, **29**, p. 3678-3690.
72. M.L. Shalz, B.J. Dalgleish, A.P. Tomsia, and A.M. Glaeser, *J. Mater. Sci.*, 1994, **29**(12), p. 3200-3208.
73. A. Buch, *Pure metals properties: a scientific - technical handbook*. 1999, Materials Park, OH: ASM International. 306 pp.
74. Y. Murakami, ed. *Stress Intensity Factors Handbook*. 1st ed. . Vol. 1. 1987, Pergamon Press: Elmsford, New York. 640 pp.
75. J.M. McNaney, R. Havens, and R.O. Ritchie, *J. Test. Eval.*, 1997, **25**(1), p. 28-35.
76. J.D. Sugar, J.T. McKeown, R.M. Marks, and A.M. Glaeser, *J. Am. Ceram. Soc.*, 2001, in review.
77. G. Elssner, S. Riedel, and R. Pabst, *Pract. Metall.*, 1975, **12**, p. 234-243.
78. M. Creager and P.C. Paris, *Int. J. Fract. Mech.*, 1967, **3**, p. 247-252.
79. C.D. Bencher, A. Sakaida, K.T. Venkateswara Rao, and R.O. Ritchie, *Metall. Mater. Trans.*, 1995, **26A**, p. 2027-2033.
80. B.D. Flinn, M. Rühle, and A.G. Evans, *Acta Metall.*, 1989, **37**(11), p. 3001-3006.
81. V.V. Krstic, P.S. Nicholson, and R.G. Hoagland, *J. Am. Ceram. Soc.*, 1981, **64**(9), p. 499-504.
82. L. Murugesh, K.T. Venkateswara Rao, and R.O. Ritchie, *Scripta Metall. Mater.*, 1993, **29**, p. 1107-1112.
83. L.S. Sigl, P.A. Mataga, B.J. Dalgleish, R.M. McMeeking, and A.G. Evans, *Acta Metall.*, 1988, **36**(4), p. 945-953.

84. T.L. Anderson, *Fracture Mechanics Fundamentals and Applications*. 2nd ed. 1995, Boca Raton, Florida: CRC Press. 688 pp.
85. P.L. Swanson, C.J. Fairbanks, B.R. Lawn, Y.W. Mai, and B.J. Hockey, *J. Am. Ceram. Soc.*, 1987, **70**(4), p. 279-289.
86. Y.W. Mai and B.R. Lawn, *J. Am. Ceram. Soc.*, 1987, **70**(4), p. 289-294.
87. S.J. Bennison and B.R. Lawn, *Acta Metall.*, 1989, **37**(10), p. 2659-2671.
88. R.O. Ritchie, *Int. J. Fract.*, 1999, **100**(1), p. 55-83.
89. S. Suresh, *Fatigue of Materials*. 1st ed. Cambridge Solid State Science Series, eds. E.A. Davis and I.M. Ward. 1991, Cambridge: Cambridge University Press. 617 pp.
90. F. Guiu, M. Li, and M.J. Reece, *J. Am. Ceram. Soc.*, 1992, **75**(11), p. 2976-2984.
91. S. Lathabai, J. Rödel, and B. Lawn, *J. Am. Ceram. Soc.*, 1991, **74**, p. 1348-1360.
92. C.J. Gilbert, R.N. Petrany, R.O. Ritchie, R.H. Dauskardt, and R.W. Steinbrech, *J. Mater. Sci.*, 1995, **30**, p. 643-654.
93. R.H. Dauskardt, *Acta Metall. Mater.*, 1993, **41**(9), p. 2765-2781.
94. R.D. Geraghty, J.C. Hay, and K.W. White, *Acta Mater.*, 1999, **47**(4), p. 1345-1353.
95. I. Gu and R.O. Ritchie, in *Fatigue and Fracture Mechanics*, eds. T.L. Panontin and S.D. Sheppard, ASTM STP 1332: West Conshohocken, PA, 1999, p. 552-564.
96. R.O. Ritchie and W. Yu. in *Small Fatigue Cracks*, eds. R.O. Ritchie and J. Lankford. TMS-AIME, Warrendale, PA, 1986, p. 167-189.
97. R.O. Ritchie and J. Lankford, *Mater. Sci. Eng.*, 1986, **A84**, p. 11-16.
98. S. Suresh and R.O. Ritchie, *Int. Metals Rev.*, 1984, **29**, p. 445-476.
99. R.O. Ritchie, W. Yu, and R.J. Bucci, *Eng. Fract. Mech.*, 1989, **32**, p. 361-377.
100. X. Hu and Y.-W. Mai, *J. Am. Ceram. Soc.*, 1992, **75**(4), p. 848-853.
101. J.C. Hay and K.W. White, *J. Am. Ceram. Soc.*, 1993, **76**(7), p. 1849-1854.
102. R.W. Steinbrech, F. Deuerler, A. Reichl, and W. Schaarwächter. in *Science of Ceramics*, ed. D. Taylor, R.W. Davidge, R. Freer, and D.T. Livey. The Institute of Ceramics, Shelton, Stoke-on Trent, Staffs., UK, 1987, p. 659-664.
103. A. Saxena and S.J. Hudak, *Int. J. Fract.*, 1978, **14**(5), p. 453-467.
104. C.C. Veerman and T. Muller, *Eng. Fract. Mech.*, 1972, **4**, p. 25-32.
105. K.T. Venkateswara Rao, G.R. Odette, and R.O. Ritchie, *Acta Metall. Mater.*, 1992, **40**(2), p. 353-361.
106. M. Lane, R.H. Dauskardt, A. Vainchtein, and H. Gao, *J. Mater. Res.*, 2000, **15**(12), p. 2758-2769.
107. S.W. Freiman, K.R. McKinney, and H.L. Smith. in *Symposium of Fracture Mechanics of Ceramics*, eds. R.C. Bradt, D.P.H. Hasselmann, and F.F. Lange. Plenum New York, New York, 1974, p. 659-676.
108. R. Steinbrech, H. Blanke, R. Knehans, and W. Schaarwächter. in *Science of Ceramics*, ed. P. Vincenzini. National Research Council Research Institute for Ceramics Technology, Faenza, 1983, p. 655-660.
109. B. Lawn, *Fracture of Brittle Solids*. 2nd ed. Cambridge Solid State Science Series, eds. E.A. Davis and I.M. Ward. 1993, Cambridge, UK: Cambridge University Press. 378 pp.